NEW PROPOSALS FOR MODELING THE THERMO-MECHANICAL RESPONSE OF STEEL STRUCTURES UNDER FIRE USING BEAM-TYPE FINITE ELEMENTS

by

Myriam Rocío Pallares Muñoz

Thesis proposed as partial fulfillment of the requirements for the Ph.D. in

Construction Engineering

Universitat Politècnica de València

València, Spain

February, 2022

Supervisor: Ph.D. Ignacio Payá Zaforteza

Advisors: Ph.D. Ignacio Payá Zaforteza
Ph.D. Antonio Hospitaler Pérez

UNIVERSITAT POLITÈCNICA DE VALÈNCIA

ABSTRACT

NEW PROPOSALS FOR MODELING THE THERMO-MECHANICAL RESPONSE OF STEEL STRUCTURES UNDER FIRE USING BEAM-TYPE FINITE ELEMENTS

by Myriam Rocío Pallares Muñoz

Fire is one of the main hazards that can affect steel structures. The impact of fire on these structures is highly adverse and complex to simulate, mainly in realistic fire scenarios, where heating in steel members is non-uniform and in slender steel members because they fail prematurely by local buckling. In order to accurately predict the response of steel structures to fire, advanced and complex FE models with shell and solid elements have been developed. However, these shell models are computationally expensive, complicating the carrying out of more complex analyses that require many simulations in a short time and at low computational costs. Therefore, there is a need to develop simple, accurate, and low-cost computational models as reliable as shell-type models that open the path more easily towards modeling more complex steel structural problems in fire conditions. This thesis presents simple and low-cost proposals to simulate the mechanical response of steel structures under fire using Timoshenko's beam-type finite element available in Ansys. One of the proposals consists of a new methodology for the 3D-analysis of steel frames subjected to non-uniform temperatures by fire. The others consist of two modeling strategies for analyzing the lateral-torsional buckling in class-4 steel structural members at elevated temperatures. The proposals significantly simplify the structural modeling and satisfactorily validate numerical and experimental results. That means that complex fire engineering problems, such as probabilistic and optimization analyses, can be handled much more easily, representing a significant step toward the generalized application of performance-based approaches to deal with fire effects on steel structures.

UNIVERSIDAD POLITÉCNICA DE VALENCIA

RESUMEN

NUEVAS PROPUESTAS PARA MODELIZAR LA RESPUESTA TERMOMECÁNICA DE ESTRUCTURAS DE ACERO BAJO FUEGO UTILIZANDO ELEMENTOS FINITOS TIPO VIGA

por Myriam Rocío Pallares Muñoz

El fuego es uno de los principales riesgos que pueden afectar a las estructuras de acero. El impacto del fuego en estas estructuras es muy adverso y complejo de simular, principalmente en escenarios de fuego realistas, donde el calentamiento en los miembros de acero no es uniforme y en miembros de acero esbeltos porque fallan prematuramente por la aparición de abolladuras locales. Para predecir con exactitud la respuesta de las estructuras de acero al fuego, se han desarrollado modelos avanzados y complejos de EF con elementos de cáscara y sólidos. Sin embargo, estos modelos son costosos desde el punto de vista computacional, lo que complica la realización de análisis más complejos que requieren muchas simulaciones en poco tiempo y con bajos costes computacionales. Por lo tanto, es necesario desarrollar modelos computacionales sencillos, precisos y de bajo coste, tan fiables como los modelos de cáscara, que abran el camino más fácilmente hacia la modelización de problemas estructurales de acero más complejos en situación de incendio. En esta tesis se presentan propuestas sencillas y de bajo coste computacional para simular la respuesta mecánica de estructuras de acero en condición de incendio utilizando un elemento finito de viga de Timoshenko de Ansys. Una de las propuestas consiste en una nueva metodología para el análisis en 3D de estructuras de acero sometidas a temperaturas no uniformes por el fuego. Las otras consisten en dos estrategias de modelización para analizar el pandeo lateral torsional en miembros de acero de clase 4 a temperaturas elevadas. Las propuestas simplifican significativamente la modelización estructural y se validan satisfactoriamente con resultados numéricos y experimentales. Esto significa que problemas complejos de ingeniería de incendio, como los análisis probabilísticos y de optimización, pueden tratarse con mucha más facilidad, lo que representa un paso importante hacia la aplicación generalizada de enfoques basados en el desempeño para tratar los efectos del fuego en las estructuras de acero.

UNIVERSITAT POLITÈCNICA DE VALÈNCIA

RESUM

NOVES PROPOSTES PER A MODELIZAR LA RESPOSTA TERMOMECÀNICA D'ESTRUCTURES D'ACER BAIX FOC UTILITZANT ELEMENTS FINITS TIPUS BIGA

per Myriam Rocío Pallares Muñoz

El foc és un dels principals riscos que poden afectar les estructures d'acer. L'impacte del foc en estes estructures és molt advers i complex de simular, principalment en escenaris de foc realistes, on el calfament en els membres d'acer no és uniforme i en membres d'acer esvelts perquè fallen prematurament per l'aparició d'abonyegadures locals. Per a predir amb exactitud la resposta de les estructures d'acer al foc, s'han desenvolupat models avançats i complexos d'elements finits de corfa i sòlids. No obstant això, estos models són computacionalment costosos, la qual cosa complica la realització d'anàlisi més complexos que requerixen moltes simulacions en poc de temps i amb baixos costos computacionals. Per tant, és necessari desenvolupar models computacionals senzills, precisos i de baix cost, tan fiables com els models de corfa, que òbriguen el camí més fàcilment cap a la modelització de problemes estructurals d'acer més complexos en situació d'incendi. En esta tesi es presenten propostes senzilles i de baix cost per a simular la resposta mecànica d'estructures d'acer en condició d'incendi utilitzant un element finit de biga de Timoshenko d'Ansys. Una de les propostes consistix en una nova metodologia per a l'anàlisi en 3D d'estructures d'acer sotmeses a temperatures no uniformes pel foc. Les altres consistixen en dos estratègies de modelització per a analitzar el bombament lateral torsional en membres d'acer de classe 4 a temperatures elevades. Les propostes simplifiquen significativament la modelització estructural i es validen satisfactòriament amb resultats numèrics i experimentals. Açò significa que problemes complexos d'enginyeria d'incendi, com les anàlisis probabilístiques i d'optimització, poden tractar-se amb molta més facilitat, la qual cosa representa un pas important cap a l'aplicació generalitzada d'enfocaments basats en l'exercici per a tractar els efectes del foc en les estructures d'acer.

TABLE OF CONTENTS

LIST OF FIGURES

LIST OF TABLES

ACKNOWLEDGMENTS

I extend sincere thanks to Fundación Carolina, Universitat Politècnica de València and Universidad Surcolombiana for the doctoral fellowship. I also thank my directors for their advice, especially Dr. Ignacio Payá, for his support and rigor, which were extremely useful for the successful conclusion of this research. Thanks also to my dear husband and family, who have always believed in me. Beyond everything, I thank God for being my permanent source of inspiration.

This thesis is a compilation of two previously published works by the author and her directors. Therefore, all its chapters include the contents from the following open access publications adapted to the format of this thesis:

1) A new methodology using beam elements for the analysis of steel frames subjected to non-uniform temperatures due to fires, published in the June 2021 issue of the Journal Structures, vol. 31; p 462–483. https://doi.org/10.1016/j.istruc.2021.02.008.

2) New modeling strategies for analyzing lateral-torsional buckling in class-4 steel structural members at elevated temperatures using beam-type elements, published in the December 2021 issue of the Journal Structures, vol. 34; p 3508–3532. https://doi.org/10.1016/j.istruc.2021.09.087.

Chapter 1

INTRODUCTION

Steel frames define the skeleton of many residential, commercial, industrial, and office buildings. In fact, according to data from the Council on Tall Buildings and Urban Habitat (CTBUH), in early 2020, 67% of the world's 100 tallest buildings used steel or steel-concrete composite structural systems [1]. The list includes, e.g., Dubai's Burj Khalifa and Princess Tower skyscrapers, Mecca's Royal Clock Tower, and 30 Hudson Yards in New York. Steel members are also used to construct large projects such as long-span bridges. The main reasons are steel structures have a greater strength with less weight, can be built in most climatic conditions, and are versatile. However, in large-scale constructions, the open cross-sections of steel frame members need to be significant to carry the high load solicitations, resulting in heavier and more expensive structures. This situation makes optimizing costs at acceptable performance levels necessary, which implies using lighter high-strength sections. Recent cases demonstrated it. For example, in the Wirkowice bridge in Poland (2020), hot-rolled high-strength lightweight steel sections were used to reduce the weight and increase the bridge span [2]. Another illustrative case is Chicago's Union Station Tower (2020). In this 51-floor office steel building, designers reduced the total structural steel in the upper perimeter columns by almost 20% using stronger but lighter steel elements (552 MPa), creating more open space in upper floors [3]. However, the decrease in the amount of material in fabricating steel members to become lighter also makes them slenderer. That condition may compromise the structure's stability because of the possible activation of global or local buckling failure phenomena that, in practice, are more critical when the steel structure is in a fire situation [4]. Examples of such fire failures have been observed in buildings (e.g., the 2001 fire in New York City's World Trade Center 7 [5–7] or the 2017 fire in Tehran's Plasco building [8,9]) and bridges (e.g., the I-65 overpass fire in Birmingham, Alabama, USA [10] and similar cases reported in [11–14]).

The risk of fire is one of the main hazards affecting all types of constructions, and steel constructions are especially vulnerable to fire because structural steel can compromise its integrity at high temperatures. For example, at 300ºC and above, structural steel begins to lose its strength gradually. It can withstand approximately 425ºC before it starts to soften, and between 600ºC and 650ºC, it will lose half of its resistance and be at risk of failure depending on the load it is supporting. This vulnerability vis-à-vis fire hazards has motivated the development of methodologies to predict the steel structures' response to fire. These methodologies typically have three components: a fire model representing the effects of fire on the structure's environment, a thermal model that predicts the temperatures in the structural members, and a mechanical model that provides the structure's response caused by mechanical and thermal stresses.

For the fire model, there are two design strategies. The most common fire design strategy is the prescriptive approach, where a nominal fire curve represents the fire (e.g., the ISO 834 fire curve), and the structure is requested to resist the effects of this fire curve for a code-specified time. More advanced is the performance-based approach, where an effort is made to represent the physical fire features. For this purpose, fire models of different complexity are available (e.g., parametric fires, zone models, localized fires, or computational fluid dynamics -CFD- models).

More realistic models, such as localized fires or CFD [15,16], do not uniformly heat the structure and, therefore, impose non-uniform temperature fields.

When a performance-based approach is used, advanced finite element calculation models are required to conduct realistic analyses of fire-exposed structures. The thermal model involves a heat transfer analysis, including the effects of the non-uniform thermal exposure, the main thermal actions, and the variation of the material's thermal properties with the temperature. The structural model includes the material's temperature-dependent mechanical properties, the combined effects of mechanical and thermal actions, and the effects of geometric and material nonlinearity.

Advanced models to obtain reliable approximations of the structural response in steel structures must also consider the following aspects:

1. Residual stresses created in the fabrication of steel members remain in the whole section of the unloaded member, even after cooling, so they are present before member loading as an initial condition at room temperature.
2. The geometries resulting from the fabrication process of steel members are not perfect, and therefore, initial imperfections are present.
3. The steel members of slender cross-sections solicited in bending fail prematurely by local buckling.

Typically, advanced calculation models for predicting the realistic response of steel structures under fire are built with shell elements [17–29]. That is because shell models naturally discretize the temperature variation in cross-section and can reproduce the buckling response of slender cross-section steel members; however, they are complex to build, and their computational times are high.

Some assumptions are frequently adopted to reduce the high computational cost and complexity of shell models. These assumptions are: a) temperatures in the cross-section of steel members are uniform [17,18,22]; b) thermal expansion is negligible [21,23,30]; c) residual stresses are not relevant because they dissipate during the fire [21,23,24,31–33]. However, these assumptions might lead to results far from the real ones. For example, in realistic fire scenarios, the non-uniform temperature field in the cross-section causes steel being a homogeneous material at room temperature, to behave like a highly heterogeneous material. In other words, the thermal gradients make the sections behave as if they were composed of several materials due to the temperature dependency of steel mechanical properties leading to shear effects in the cross-section becoming relevant. Furthermore, the heterogeneity caused by the asymmetrical temperature field in the cross-section originates a coupling between the axial and bending [34]. As a result, an axial force produces a curvature and a bending moment induces elongation, making the non-uniform temperature field in the cross-section affects the displacements field of the structure. On the other hand, in localized fire scenarios, the steel structures do not heat uniformly so that adverse effects of the residual stresses can remain in zones less heated.

The other aspect to consider is thermal strains. As the thermal expansion of steel is temperature-dependent, the non-uniform temperature field in the cross-section (time-varying) makes thermal strains in isostatic steel members vary in space and time. Furthermore, bending produced by the non-uniform temperature field in the cross-section creates thermal stresses

that add to the residual and the other stresses (self-weight and mechanical). In statically indeterminate steel members, the induced thermal stresses by the non-uniform temperature field of the cross-section produce bending in addition to that of the acting loads. These spatially and time-varying induced thermal stresses are combined with the residual and all other stresses (self-weight and mechanical). All of these interactions affect the strain-stress state and, therefore, the response of the structure.

Regarding the geometric imperfections, these are residual thermal strains coming from the plate fabrication and cutting process. Since thermal strains occur in all three directions in realistic fire scenarios, transverse thermal strains and those induced by the Poisson effect intensify the geometrical imperfections of the steel structure members. The Poisson effect also induces thermal stresses at the points with restrained degrees of freedom; therefore, thermal strains must be considered to account for all temperature effects during the fire exposure time.

Unlike high-cost shell elements, the finite beam elements are especially appealing because of their much easier modeling and lower computational cost, resulting in savings in modeling times, CPU times, memory, and storage demands. However, the use of beam-type elements to model the response of steel structures to realistic fires is very challenging due to the following reasons:

a) The difficulty to properly discretize the cross-section temperature (varying in space and time) when transverse thermal gradients are present.

b) The difficulty to adequately include both the residual stresses into the cross-section and the initial imperfections on the geometry.

c) The problems reproducing the local buckling in the cross-section parts subjected to high compressions in thin-walled members.

One of the main focuses of research to date has been on studying instability, its occurrence, and its effect on fire-affected steel members, and most simulations in such studies have been carried out with shell elements [18–20,22–28]. Although the instability of steel members has been extensively investigated for room temperature conditions, instability in steel members heated to elevated temperatures is, in fact, a topic still under study and of great interest. Hence, experiments and simulations have been conducted to obtain more information and, e.g., to propose new design formulations in the Eurocode to ensure the safety and serviceability of steel structures in modern constructions [23,29].

Researchers have also recently been interested in building models with finite beam elements to analyze the thermo-structural response of steel structures to reduce shell elements' complexity and high cost [35–43]. These simulations have focused on studying instability in fire-affected class-4 steel members involving beam-type finite elements [31,44–51]. The studies have concentrated mainly on analyzing flexural torsional buckling failures in slender section columns, with less frequent analysis of lateral-torsional buckling failures in beams.

However, simulating steel structures under realistic fire scenarios using finite beam elements implies a good approximation of the temperature variation in the cross-section during the fire. That is because the accurate calculation of material properties, nonlinear stress-strain relationships, and thermal strains depend on it. Therefore, the structure's response is more realistic, as long as the spatially and temporally varying temperature field is as well modeled as possible. In simulations of class-4 steel members, this is crucial because, under the same load

level, at the most heated points of the cross-section, the occurrence of local buckling failure due to material softening with increasing temperature will be more likely. In addition, the inclusion of the adverse effects of residual stresses and imperfections in the models is essential in studying the instability of thin-walled steel members heated at elevated fire temperatures. The reason is they act as initial conditions that modify the initial strain-stress state of the steel structure.

To approximate the non-uniform temperature distribution of a finite beam element cross-section, the temperatures over time of three cross-section points (the centroid of the top flange, the web, and the bottom flange) are typically used [35,36]. To do so, the temperature-time at one of these points (e.g., the temperature-time evolution of the web centroid) is taken as the amplitude curve[1]. Then, the temperature-time curves at the other two cross-section points are calculated as factors of that amplitude curve, constants over time. As a result, the amplitude curve is the parent curve, and the temperature-time curves at the other two cross-section points are its children. The problems of this non-uniform temperature approximation are that: 1) it depends on an exact definition of the factors that remain constant during the whole fire; 2) it assumes only a linear variation of the temperature in the web direction; 3) it cannot represent the changes produced in the heating/cooling rate of the cross-section points when insulation elements or radiative shadows are present. Furthermore, this approach involving heat transfer analysis of the cross-section by finite elements only uses the temperature results, ignoring the importance of thermal gradient results responsible for temperature changes in both cross-section directions. It also ignores that the nature of fire is three-dimensional, and the effects of fire on structures are three-dimensional so that the non-uniform temperature fields in realistic steel structures are 3D.

Moreover, Euler-Bernoulli beam elements are the most commonly used in simulations of steel structures exposed to fires with finite beam elements, including simulations of class-4 steel members [23,35,36,47–50,52]. However, Timoshenko beam elements are the most appropriate for analyzing the response of steel structures exposed to non-uniform temperature fields. That is because they assume a cross-section shear state (not present in Euler-Bernoulli's theory) that better approximates cross-section deformation in deep members. This characteristic is advantageous since the material becomes heterogeneous under non-uniform temperature and shear effects are relevant in heterogeneous beams, so they behave like deep beams.

Before this research, there was no simple, general, systematic, and low-cost methodology to represent the non-uniform temperature in the cross-section of finite beam elements to allow more realistic 3D structural analyses adapted to the three-dimensional nature of fire and the existence of 3D non-uniform temperature fields in real steel structures. Furthermore, there were also no proposals for modeling the lateral-torsional buckling phenomenon in slender section members with finite beam elements that could reproduce the behavior of the beam load capacity, the buckling limit state, and the local and global failure modes, involving all the phenomena that are present, such as: geometric and material nonlinearity, thermal strains, the Poisson effect, initial imperfections, initial residual stresses, and non-uniform temperature distribution in the cross-section.

Due to this need for simple, accurate, and low-cost computational models as reliable as shell models, new proposals for modeling the thermo-mechanical response of the steel structures

[1] An amplitude curve is used (e.g., by Abaqus) to specify the time variations of a transient load. The amplitudes of the curve are defined as model data and do not depend on the integration scheme step used for the solution of the problem.

under fire were developed in this thesis and published in a high-impact journal [43,51]. The new proposals were built with 3D-BEAM189 finite elements included in Ansys. They are seven degrees-of-freedom Timoshenko's beam finite elements (six are for translations and rotations in x, y, z, and the seventh is for the warping magnitude representing the cross-section deformations due to high temperatures). BEAM189 has a computational power that reduces the computational time as well as the model-building effort. These savings in time, memory, and storage demand enable addressing complex analyses more easily and making feasible more complex structural fire engineering studies in which millions of simulations must be run quickly, such as parametric, probabilistic, and optimization analyses. Therefore, this contribution represents a significant step toward applying performance-based approaches to address the fire effects on steel structures.

The first proposal is a new low-cost computational methodology to analyze steel frames subjected to non-uniform temperatures due to fires. This methodology involves the space-time variation of the temperature and displacement fields. The non-uniform temperature space-time field is represented by a temperature mean value and the two mean values of the section thermal gradients, which vary in time during the fire. This methodology that captures 3D phenomena such as buckling, flexural-torsional buckling, and warping was satisfactorily validated with experimental and numerical results of the Cardington frame test. The second proposal includes two new modeling strategies for analyzing the lateral-torsional buckling in slender steel structural members at elevated temperatures, which significantly simplify the structural modeling. These strategies, called Fiber Beam Model (FBM) and Cruciform Frame Model (CFM), include initial geometric and material imperfections and thermal strains. In the FBM, the steel member is represented by a single fiber of I-section beam elements. In the CFM, a cruciform arrangement of rectangular beam finite element fibers idealizes it. Both strategies were satisfactorily validated with experimental and numerical results of Test-1 and Test-3 carried out in the "Fire design of steel members with welded or hot-rolled class-4 cross-section" (FIDESC4) research project on a slender beam of class-4 section. Although both strategies correctly capture the lateral-torsional buckling resistance, CFM can, in addition, adequately reproduce the local buckling failure and significantly reduce the computational time.

OBJECTIVES

General

- Develop simple, accurate, and low-cost computational modeling strategies as reliable as complex shell models to address the effects of fire on steel structures.
- Minimize the computational cost and effort of simulating the thermo-mechanical response of steel structures under realistic fire scenarios.
- Implement the beam-type finite elements to simulate the thermo-mechanical response of steel structures exposed to fire.

Specifics

1. Propose a simple, general, and systematic methodology for representing the non-uniform temperature in the cross-section of beam elements that enables

performing 3D structural analysis adapted to the three-dimensional nature of fire and the existence of 3D non-uniform transient temperature fields in realistic structures.

2. Propose new modeling strategies for considering lateral-torsional buckling in slender steel beams with beam-type finite elements that take into account all the phenomena involved and reproduce the thermo-structural response of the steel beams, including global and local buckling.
3. Validate the proposals with numerical and experimental results.

This document is structured as follows: Chapter 1 introduces the problem statement, the objectives, and the research scope. Chapter 2 describes the Ansys finite beam element used in the new proposals. Chapter 3 presents the proposed methodology to analyze steel frames subjected to non-uniform temperatures by fire. Chapter 4 presents the new modeling strategies to analyze the lateral-torsional buckling in class-4 steel structural members at elevated temperatures. Chapter 5 develops the discussion of results. Finally, in Chapter 6, the main conclusions are drawn, and future works are presented.

Chapter 2

FINITE BEAM ELEMENT USED

Proposed new modeling strategies are made up of appropriate Timoshenkos' BEAM189 finite elements available in Ansys. This finite element is three-node quadratic (see Fig. 1a), with seven degrees of freedom at each node: 3 translations (Ux, Uy, Uz), 3 rotations about the *x*, *y*, *z*-global directions (ROTx, ROTy, ROTz), and the warping magnitude (WARP) to represent the cross-section deformations due to high temperatures. Each section of the BEAM189 finite element is a predetermined set of cells with nine nodes and four integration points per cell (see Fig. 1b). The number of cells influences the accuracy of the geometric and material properties and the ability to model the nonlinear stress-strain relationship in the element cross-section. The calculations of the material inelastic behavior and the section temperature variation are performed at the section integration points. The element supports uniform temperatures and thermal gradients that vary linearly in the two cross-section directions and throughout the element [53]. BEAM189 has an excellent capacity for static and dynamic geometrical and material nonlinear analysis, suitable for solving stability problems (buckling, post-buckling, and collapse). The Timoshenko theory of the BEAM189 element assumes a shear-state in the cross-section (not present in Euler-Bernoulli theory). This assumption better approximates the cross-section deformation in deep beams, which is considered necessary given the great relevance of shear effects in fire-affected members, where the material behaves as heterogeneous due to the effects of high temperatures on the steel mechanical properties [34,43]. Results such as deflections at the pseudo-mesh of the BEAM189 finite element cross-section can be shown in extruded views in the post-processing stage. Results querying in extruded view are based on the post-processing query strings that interact with the database of the calculation results in the pseudo-mesh nodes of the section. This 3D-BEAM189 computing power allows the implementation of the proposed modeling strategies. Fig. 1 shows the geometry, the nodes, the coordinate system (local and global), and the cross-section of the BEAM189-finite element.

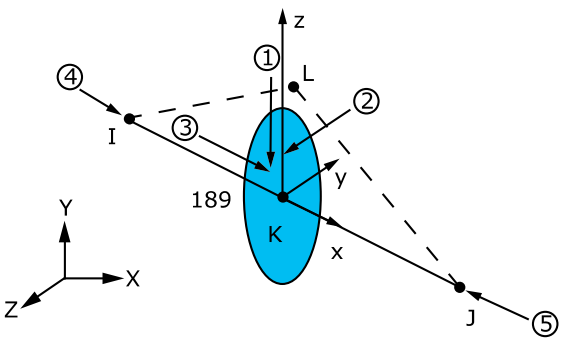

(a) Definition and local axes [53]

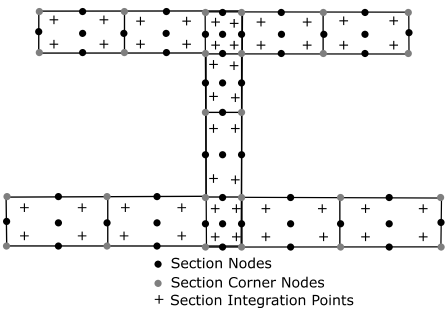

(b) Cells and nodes of the cross-section pseudo-mesh [53]

Fig. 1 BEAM189 finite element

Chapter 3

METHODOLOGY TO ANALYZE STEEL FRAMES SUBJECTED TO NON-UNIFORM TEMPERATURES BY FIRE USING BEAM-TYPE ELEMENTS

This chapter includes the content from sections 1 to 8 from paper "A new methodology using beam elements for the analysis of steel frames subjected to non-uniform temperatures due to fires" published in the June 2021 issue of the Journal Structures, vol. 31; p 462–483. https://doi.org/10.1016/j.istruc.2021.02.008.

3.1 Justification and antecedents

The advanced calculation models for realistic analyses of fire-exposed steel structures can be built using the beam, shell [54], or solid finite elements [55]. Within these finite elements, beam-types are especially appealing because of their much easier modeling and lower computational cost, resulting in savings in modeling times and CPU-times, memory, and storage demands. However, the use of finite beam elements to model the response of structures to realistic fires is very challenging. That is due to, among other reasons, the problems to adequately reproduce phenomena such as web buckling and the difficulty to properly discretize the temperature in the cross-section of the elements when longitudinal and/or transversal thermal gradients are present. These gradients appear, e.g., when the temperature fields around the structure are not uniform, as is the case for bridges [56–58] and perimeter columns [31], and/or when the steel members are joined to or protected by concrete elements [59].

Achieving a good approximation of the non-uniform temperature in the beam element cross-section is justified insofar as the accurate calculation of material properties, nonlinear stress-strain relationships, and thermal strains depend on a good approximation of the temperature in the beam section. Therefore, the structure's response is more realistic, as long as the temperature field in the beam cross-section is as well modeled as possible. A common approach to represent non-uniform temperature fields, i.e., thermal gradients, within the cross-section of a structural element is the use of multiplier values applied to the cross-section parts (e.g., the web and the two flanges). These multipliers are calculated as temperature factors from a pattern-curve, which, in some cases, is the gas compartment temperature [60] and, in others, it is the temperature curve of one of the section parts [35]. As a result, the patterns of the temperature evolution are the same in the entire section. Additionally, it is also common to assume a uniform temperature by parts (i.e., web and two flanges), or, e.g., a linear temperature variation with distance from the top/bottom face of the cross-section (linear interpolation along the vertical axis of the cross-section).

Several authors have taken all or part of these approaches to use beam elements from several software packages such as Ansys, Abaqus, LS-Dyna, Vulcan, and Safir to model structures under fire. For example, Burges and Alexandrou used Vulcan software to apply different factorized temperatures to each part of an I-profile section steel beam in fire based on the gas temperature curve [37–39]. Santiago *et al.* built a structural 2D model of the Cardington framework fire test using Abaqus and Safir beam elements. They applied a linear temperature variation, constant through time, within the vertical direction of the steel member sections [35,36]. To do so, they first calculated the temperature time-history at a representative part of the cross-section with a

2D-heat transfer analysis, which then is scaled to obtain the time history at other representative parts. This section temperature distribution based on multipliers and pattern curves (also called amplitude curves) has several disadvantages, for example, 1) it depends on a very good definition of the multipliers that remain constant throughout the fire, 2) only considers the temperature variations in the web direction, 3) cannot represent the changes produced in the heating/cooling speed of the section points in the presence of isolation elements. In addition, these approaches that have involved previous section heat transfer analysis have only used temperature results and have ignored the importance of thermal gradient results responsible for temperature changes in both directions of the section.

Kumar *et al.* applied a linear temperature variation in the vertical direction of the I-profile section steel members of a framework tested in fire using Ansys beam elements [40]. To do so, they first built a thermal model of the entire framework using shell elements to know the temperatures at specific framework cross-sections. Then, they determined the average temperature in those sections and in the two flanges to calculate, between these three values, a linear vertical variation of the temperature of each section that they later applied to the beam elements of a structural model. The disadvantage of entire member heat transfer analyses using shell (or solid) elements is that they are very robust and involve unnecessary modeling effort compared to the information that can be processed from them when structural models are built with beam elements. In contrast, the heat transfer analyses only of the sections with plane elements allow a good detail of the section thermal phenomenon characteristics if structural models are built with beam elements later. Moreover, this type of heat transfer analysis is easier to model and collect adequate and enough information on the thermal phenomenon of each section.

More advanced is the LS-Dyna software beam element approach, based on the formulation of a degenerated solid element where the temperatures at the integration points of the beam section are calculated by linear interpolation from the previously defined temperature in some points of the section using the normalized coordinates. Rackauskaite *et al.* used LS-Dyna to build a 2D model of the Cardington framework. These authors directly applied the temperature-time curves at the experiment temperature's three points of the section [41]. However, the LS-Dyna beam element has two drawbacks. First of all, it uses a particular formulation that cannot be used in other software. Secondly, LS-Dyna is an explicit analysis software, i.e., it uses explicit dynamics algorithms in which very small-time steps are required to maintain the calculations numerical stability. By contrast, fire phenomena in structures before collapsing do not take place in microseconds or seconds (as it happens, e.g., in impacts, explosions, collisions, and even earthquakes) but last minutes and, in some cases, even hours. Therefore, fire modeling in structures with explicit techniques requires many time steps that must be calculated one by one sequentially in time, i.e., the parallelism of computing can only be used for the subdivision of spatial domains.

Within this context, a simple new general systematic methodology is proposed to model steel structures' behavior under fire in non-uniform temperature conditions (i.e., under longitudinal and/or transversal thermal gradients). This methodology uses beam elements that incorporate the two spatially and temporally variable thermal gradients of the section from the thermal model and, therefore, reproduce the time-dependent thermal and mechanical structural response. Triangle-shape plane elements with quadratic approximation in the 2D-thermal model and seven-degree Timoshenko's beam elements in the 2D/3D mechanical models are used. This methodology was validated with the full-scale experimental measurements carried out in

Cardington published in [61,62], and the 2D-numerical simulations carried out by Franssen *et al.* and Santiago *et al.* [30,35,36].

This chapter is organized as follow: Section 3.2 presents a description of the Cardington test used to validate the proposed methodology; Section 3.3 describe the numerical model of the Cardington framework; Section 3.4 explains the details of the proposed methodology; Section 3.5 presents the heat transfer analysis of the framework cross-sections; Section 3.6 presents the structural analysis of the Cardington framework; Sections 3.7 presents an in-depth analysis of the temperature and thermal gradient results of the heat transfer models of the steel member cross-sections, and finally, Section 3.8 presents an analysis of the framework's mechanical results.

3.2 Cardington fire test

The experiment to validate the methodology to approximate the effects of non-uniform heating in the section and evaluate the influence of thermal expansion, lateral restraint, and the effects of 3D modeling was conducted by Latham *et al.* [61] on a loaded steel 2D-framework located inside a compartment built in Cardington for fire testing (Fig. 2). The beam of the framework is a 4.550 m length UB 406x178x54 profile. This profile was bolted to two columns materialized with a UC 203x203x52-profile of 3.530 m in height. The columns were filled with autoclaved aerated concrete blocks between the flanges to protect the web from fire, and a concrete slab was used on the beam to provide thermal insulation. A specially designed subsidiary framework avoided lateral and swaying instabilities. Loads were applied to columns and at four points along the beam through hydraulic jacks and remained constant in the fire test. The test lasted 30 minutes, and maximum temperatures above 750 °C on the beam and above 606 °C were observed on the column.

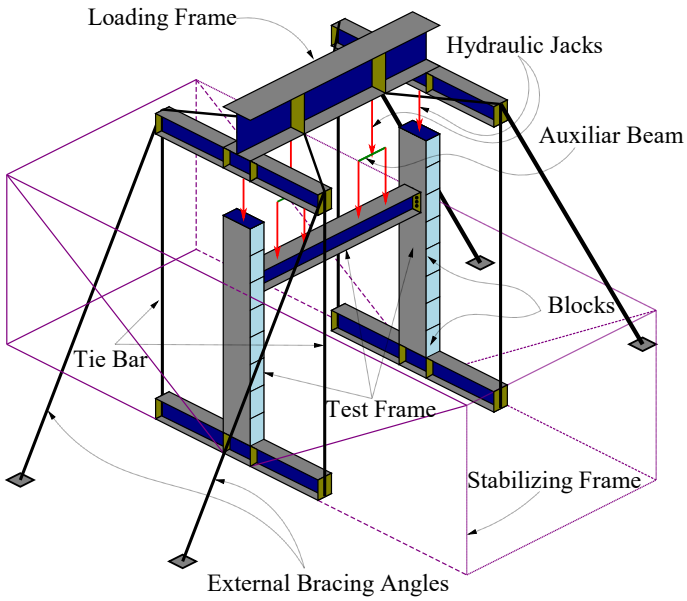

Fig. 2 Cardington framework

3.3 Numerical modeling

Due to the symmetry, the only half framework was modeled, and one spring was placed at the height of 3210.1 mm to represent the secondary framework support. Cardington framework was modeled in 2D and 3D; however, because the beam-finite element used for the modeling is 3D, out-of-plane translation constraints were added to the framework nodes to simplify that dimension in the 2D model. Furthermore, concrete elements in the framework only fill an insulating role, so they only participate in the thermal resistance but not in the structural response. 2D simulations of the Cardington experiment have been carried out by Franssen *et al.* and Santiago *et al.* using the Ceficoss, Safir, and Abaqus software [30,35,36]. However, the work presented in this paper introduces the following contributions:

- The development of a simple methodology with beam elements to determine adequately and rigorously, the response to fire of steel frames subjected to non-uniform temperatures, spending less modeling effort, and calculation time against more complex models built with finite elements of a higher level of discretization such as shells or solids.
- The use of the complete thermal response of the analyzed cross-sections to formulate the new methodology representing the non-uniform temperature field in the sections (variable in space and time), based on the average values of the temperature and the elementary thermal gradients.
- The inclusion of thermal deformations and self-weight loads in the mechanical analysis to consider additional bending deformations into the framework response.
- The inclusion of a Timoshenko's 3D-beam element with the ability to: i) including cross-section warping, ii) adequately reproduce the 3D-field of displacements when the element is subjected to non-uniform temperatures, iii) the deformability of the cross-section (Poisson effect), and iv) correctly model the mechanical 3D-response of the steel framework.

3.4 Methodology description

The Cardington steel framework was modeled in Ansys using 3D-BEAM189 structural elements (see Fig. 1). These finite elements only have displacement degrees of freedom and do not allow discretizing the temperature in the cross-section. Consequently, the non-uniform and time-varying temperature cannot be directly introduced into the beam structural finite element cross-section. However, it allows specifying an elemental uniform temperature and temperature gradients that vary linearly both in the cross-section and in the element length. For that reason, a methodology that approximates the non-uniform temperature distribution in the section of a 3D-beam structural finite element (Fig. 3a) through the following three time-varying components has been proposed:

a) A uniform temperature component equal to the average section temperature, variable in time (Fig. 3b).

b) A temperature gradient component that varies linearly about the Y-axis: this component is equal to the section average horizontal gradient, variable in time (Fig. 3c).

c) A temperature gradient component that varies linearly about the Z-axis: this component is equal to the section average vertical gradient, variable in time (Fig. 3d).

The Y and Z-axes used to describe the direction of the gradients match the 3D-beam structural finite element local directions (see Fig. 1a).

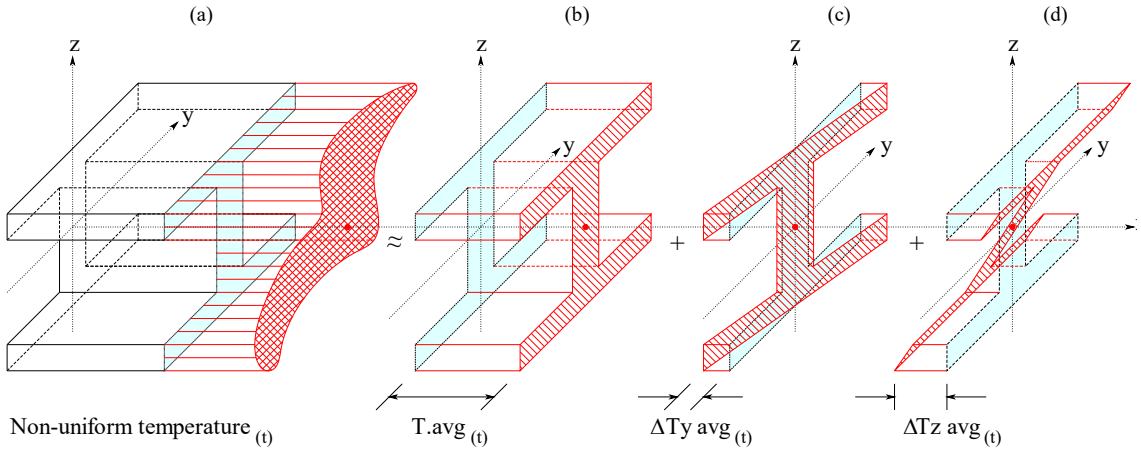

Fig. 3 Representation of the temperature profile components
(Referred to the local axes of a 3D beam finite element)

In Fig. 3a, the time-varying non-uniform temperature in the 3D-beam finite element section is represented by three time-varying average components (Fig. 3b to Fig. 3d). Thus, the temperature applied at a point of the 3D-beam finite element section (for each time) can be determined through the three time-varying components of the non-uniform temperature described. Since 3D-beam-type finite elements are used, the average temperature component is applied at the centroid so that the temperature applied at one point of the 3D-beam section can be approximated by Eq. (1).

$$T(Y,Z,t) \approx T_{avg}(t) + TGy_{avg}(t) \times Y + TGz_{avg}(t) \times Z \qquad (1)$$

In Eq. (1), T_{avg} is the average section temperature applied at the centroid. TGy and TGz are the positive or negative average horizontal and vertical gradient values of the section, respectively. Y and Z are the point coordinates (positive or negative), according to point position concerning the origin of the reference system located at the centroid of the section. In Eq. (1), lines of average gradients pass through the section centroid so that average gradient components are null at the centroid, and the temperature applied at the centroid is equal to the average section temperature.

Non-uniform temperature components in Figs. 3b to 3d are determined by carrying out thermal analyses of the framework sections. Thus, the full methodology requires that the following procedures be performed:

1) 2D-thermal analysis of each framework mixed-section with plane elements to obtain the thermal response, i.e., the time-histories of temperature and thermal gradients (horizontal and vertical) in all of the mesh's finite elements.

2) The steel section results are separated to determine only the thermal response in this material because concrete elements are not present in the structural model.

3) Average temperature (Avg_Temp) and average thermal gradients (Avg_Grad_YY and Avg_Grad_ZZ) of the steel-section are calculated at each time to obtain the time-history results of each one. For calculating these three time-varying average components (see Fig. 3), the thermal gradient results in the steel section's finite elements are averaged in each direction at each time. In addition, temperature results are also averaged in the steel section's finite elements to obtain a temperature mean value of the steel-section at each time.

4) The framework's structural model is built with 3D-beam finite elements, where the time-varying non-uniform temperature applied in the 3D-beam finite element section is represented by the three time-varying average components calculated from the section heat transfer models previously done. In this approach, average temperature and average gradients in the section vary at each time during the whole fire scenario.

5) Static geometrically and materially nonlinear analysis (GMNA) of the framework is done to determine the framework's fire resistance time and the structural response to this failure time.

In this new proposal, the variation of the two average gradient components of the section in time makes the temperature applied to the 3D-beam element section be variable in the two directions of the section at each time; i.e., a non-uniform temperature is defined in both directions of the section at each time of the fire scenario. This temperature field varying spatially and temporally affects the temperature-dependent material properties. The elastic modulus, the steel stress-strain behavior, and the thermal expansion also change as a function of the steel temperature in space and time [63].

This simple methodology makes reasonable and natural use of gradient results of the section's thermal model to represent as closely as possible the non-uniform time-varying temperature field that is applied in the 3D-beam steel section when this type of finite element is used to model the response of a structure in a fire situation. It is essential to highlight that the present methodology, unlike others [35–40,60], uses all available results of the heat transfer analysis in the section, i.e., all of the elemental temperature and elemental thermal gradients results. A summary of the methodology is presented in Fig. 4.

Details of the full methodology are shown in Figs. 8, 9, and 13. The methodology also includes the time-varying temperature in the framework beam's length, as Franssen recommended [30]. This longitudinal variation of the temperature in the framework's beam is approximated through reduction factors (*fx*) determined by a sinusoidal function, which varies between 0.90 approx. (at the beam/column connection, according to EN 1993-1-2 [64]) and 1.00 (at mid-span), considering that the fire location is at the beam mid-span. Thus, the reduction factors (*fx*) are calculated at the mid-point of each 3D-beam finite element that discretizes the framework's beam. Then, the factor (*fx*) at the midpoint of each 3D-beam finite element is multiplied by the average temperature component of the section (T_{avg} in Fig. 2b) to include a variation of the temperature in length. Since the average temperature component applied to the 3D-beam finite element section varies in time, the temperature along the beam also varies in time.

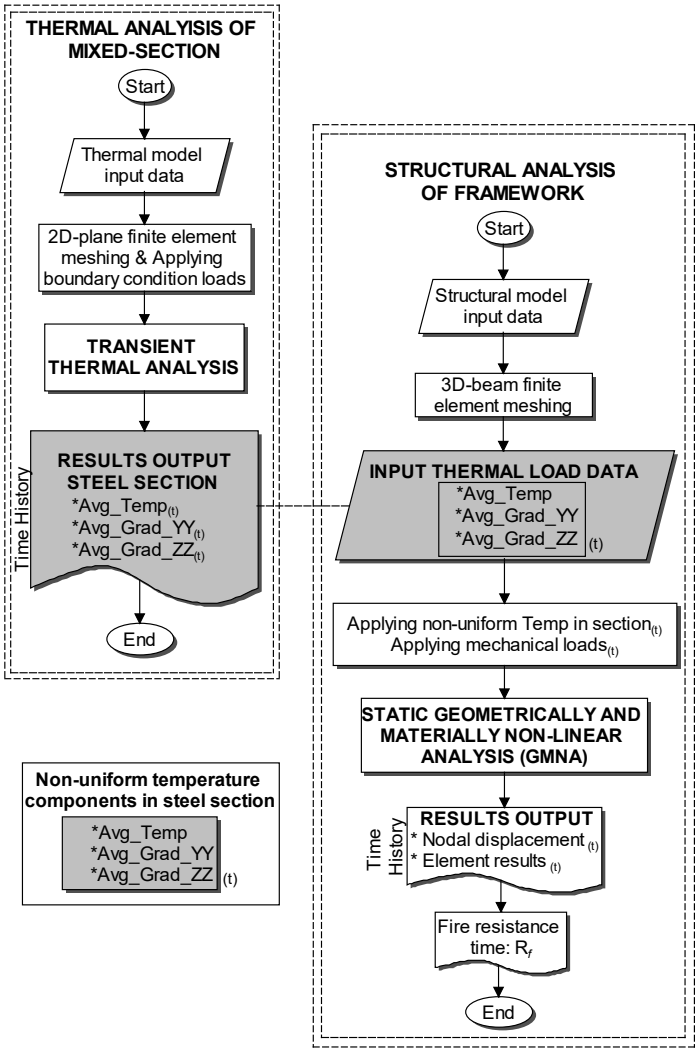

Fig. 4 Methodology summary

3.5 Heat transfer analysis of the framework sections

A complete heat transfer analysis was carried out in Ansys to determine the heat transferred to the framework sections. The thermal model includes conduction and convective-radioactive boundary conditions. The Cardington framework steel-concrete mixed-sections (beam-slab and column-block) for the transient thermal modeling are detailed in Fig. 5.

The specific heat (C_a) and thermal conductivity (λ_a) of steel with temperature were determined according to EN 1993-1-2 [64]. The convective heat transfer coefficient (α_c=25 W/m^{2}K), the resulting emissivity between the fire source and the steel (ε_{res}=0.7), and the radioactive shading effect on the outer flange of the column (ε=0.3) were taken from [36]. The density (ρ_a) of steel was assumed to be independent of temperature with a constant value of 7850 kg/m^3. Variations of the specific heat (C_p) and thermal conductivity (λ_c) with the temperature of the concrete slab were determined according to EN 1992-1-2 [65]. The convective heat transfer coefficient (α_c) and the resulting emissivity between the fire source and the concrete slab (ε_{res}) were 25 W/m^{2}K and 0.8, respectively. The density (ρ_c) of the concrete slab was assumed to be independent of temperature with a constant value of 2400

kg/m^3. For the concrete blocks isolating the column, a variation of thermal conductivity (λ_c) given by 0.20+0.0004θ_a was considered, and the specific heat and density properties were assumed to be constant values of 1050 J/kg-K and 677 kg/m^3, respectively. Franssen *et al.* and Santiago *et al.* used these thermal properties of the concrete blocks in the Cardington framework thermal simulations [30,35,36].

The discretization is carried out for: i) the UB 406x178x54 steel beam section, attached to the 1200x150 mm concrete slab section and, ii) the UC 203x203x52 steel column section attached to the aerated concrete block sections on the flanges to provide thermal insulation. Direct contact between the steel section and the concrete was assumed (as in the Cardington test) in order to consider the heat transferred from the steel section to the concrete. As a result, concrete elements produce non-uniform temperature distributions in the beam and column steel-sections.

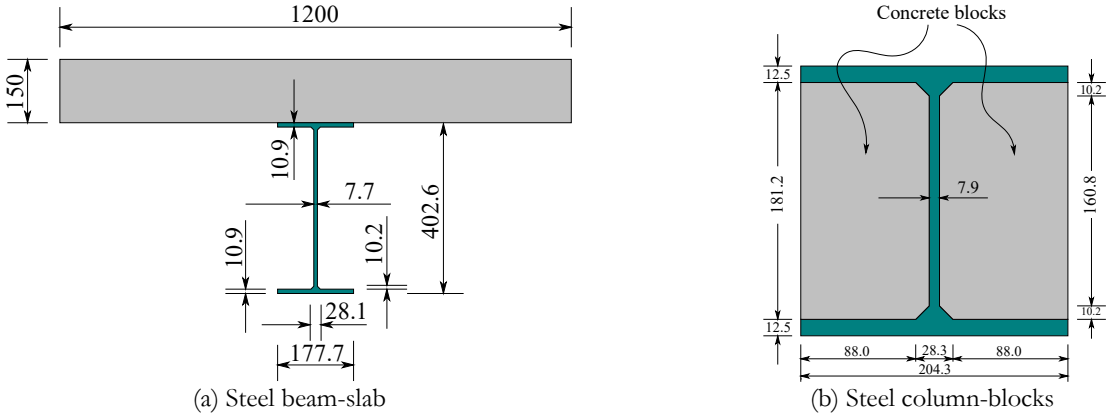

Fig. 5 Mixed cross-sections dimensions

The temperature of the environment (combustion gases) is the main parameter that affects the heat exchange between the environment (the fire) and the structure. The temperature of these environment combustion gases in the experiment was measured for 30 min. The evolution of the gas temperature over time (natural fire curve) is shown in Fig. 6 [36].

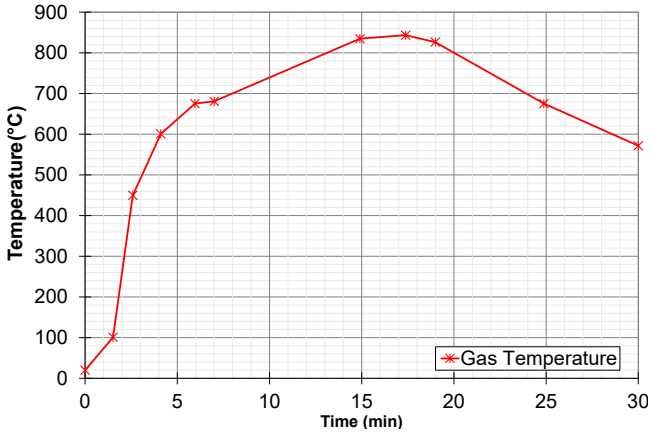

Fig. 6 Natural fire curve

Based on the thermal properties and the convection-radiation boundary conditions, 2D-heat transfer models of the steel beam-concrete slab and steel column-concrete blocks sections have been done in Ansys using PLANE35 elements. This finite element is a quadratic triangle of six (6) nodes, with a degree of freedom (temperature) per node, applicable to the transient state 2D-thermal analysis. Convection and radiation are introduced as surface loads at the model boundaries of each section.

The heat transfer analysis allows knowing the variation in space and time of the temperature field and the thermal gradient field in the section. This variation in temperature and gradients is the starting point for the methodology proposed.

Fig. 7 shows the discretization of the beam-slab and column-block sections with PLANE35 elements. These meshes do not require significant refinement since the finite element shape functions introduce a quadratic temperature approximation. Unstructured meshes of triangular-shaped elements are used because of the adaptability to the section shape (fillet zones) and the good aspect ratio, so that very good meshes are automatically generated. The number of elements *ne* in the beam and column steel sections is shown in Fig. 7a and Fig 7b.

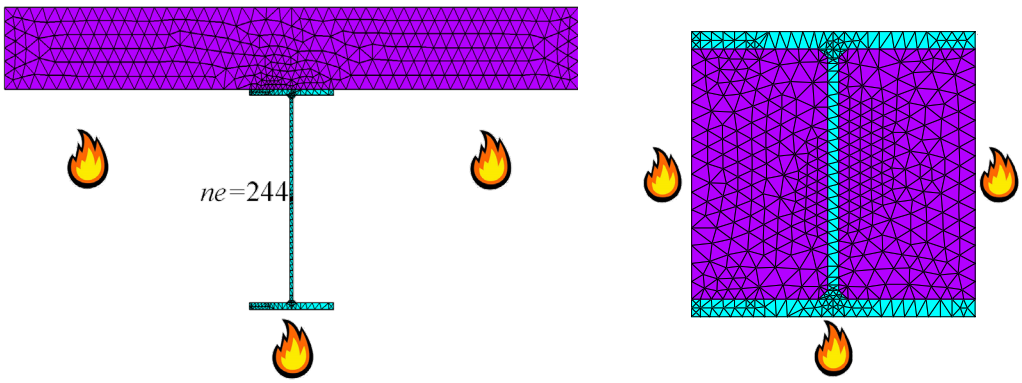

(a) Beam-slab (b) Column-blocks

Fig. 7 Cross-section's discretization

The beam and column steel-section temperatures obtained from the thermal analysis are non-uniform due to the slab on the beam and the concrete blocks in the column. The flowchart in Fig. 8a details the transient 2D-thermal analysis of the framework beam-slab and column-blocks sections subjected to non-uniform temperature fields.

The procedure starts with the input of the history-time curve of the gas temperature, the mixed-section geometry data (Fig. 8b and 8c), the temperature-dependent material properties, the Boltzman constant, the convection-radiation data, the time step Δt, and the total simulation time (ts). The mixed-section domain is discretized with PLANE-35 elements, and the transient thermal analysis is solved with Ansys. Finally, the full thermal response in the mixed-section is obtained at each time step, i.e., the time-history results of the temperatures and the thermal gradients (horizontal and vertical) in each of the finite elements of the mixed-section mesh. The horizontal and vertical thermal gradients are expressed with YY and ZZ, respectively, to relate them to the local directions of the structural beam finite element used in mechanical modeling (see Fig. 1).

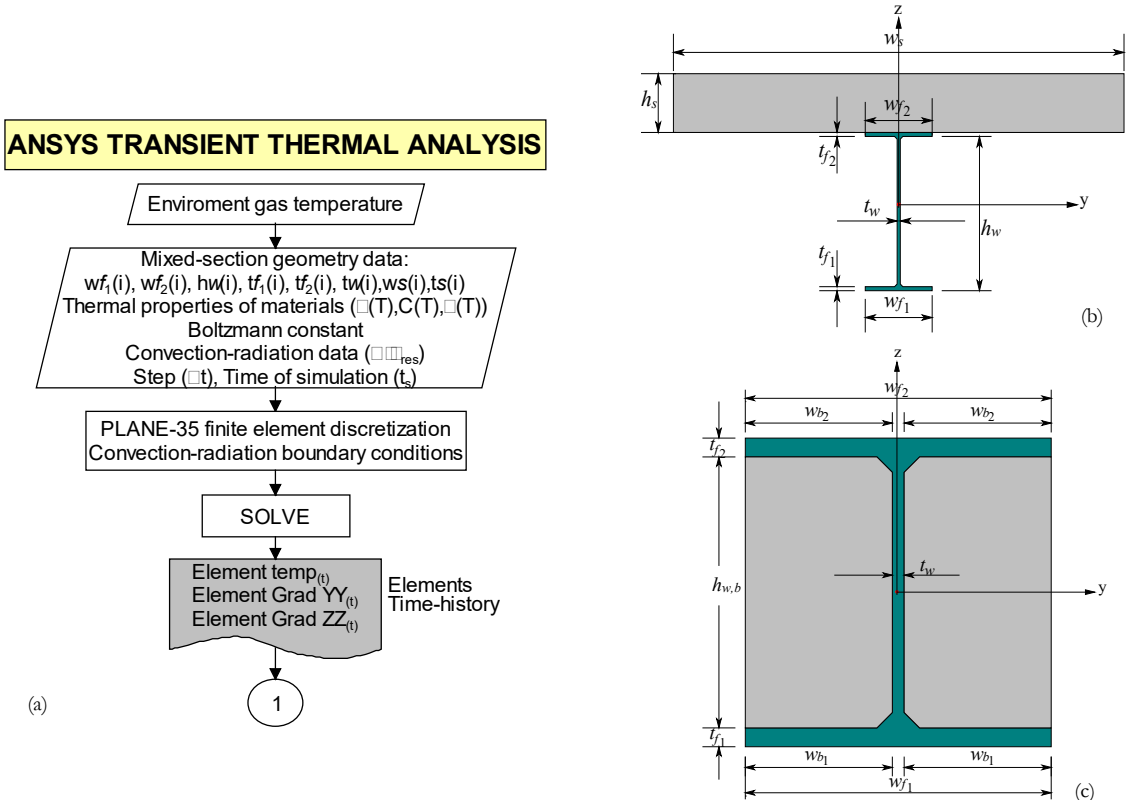

Fig. 8 Transient heat-transfer analysis flowchart of a mixed-section

Since concrete elements in the framework only fill an insulating role, only the thermal response in steel-section is considered at the end of the heat transfer analysis. Therefore, finalized the thermal analysis of the mixed-section in Fig. 8a, the procedure continues at ① to calculate the three time-varying average components described in Figs. 3 and 4, i.e., the time-history results of the average temperature and thermal gradients (horizontal and vertical) in steel-section. Before starting these calculations, temperature and gradient results in the steel-section are selected.

The flowchart in Fig. 9 details the methodology by which the three constituent components of the section temperature profile (in Fig. 4) are obtained. For each instant (t), the procedure starts from the steel-section elements thermal response obtained with the procedure detailed in Fig. 8a. The flowchart begins with the entry of the number of PLANE35 elements (ne) of the steel-section. To calculate the average temperature and the two average gradients of the steel-section at each instant (t), a cycle controlled by the counter (i) is performed, which counts the number of elements (ne) of the steel-section (i=1 to ne). In this cycle, the elemental temperatures and gradients YY and ZZ obtained from the transient thermal analysis are stored in the variables Temp(i), Grad_YY(i), and Grad_ZZ(i), then, they are accumulated in the variables Sum_Temp, Sum_Grad_YY and Sum_Grad_ZZ. Once the cycle is finished, the average temperatures and gradients of the steel-section are calculated, dividing each summation updated value by the number of elements (ne). The values of the averages are stored in (Avg_Temp), (Avg_Grad_YY), (Avg_Grad_ZZ) for each time (t). The process is repeated for each time ($t+\Delta t$) up to the total simulation time (ts). In the end, the complete tabulations of the

three history-time curves of average temperature, average YY gradient, and average ZZ gradient are obtained. The procedure is applied for each steel-section of the structural member considered. In the present case study, the number of sections analyzed is two, the beam steel-section, and the column steel-section. In the flowchart in Fig. 9, the number of PLANE35 elements in the beam steel-section is ne=244 and ne=278 for the column steel-section.

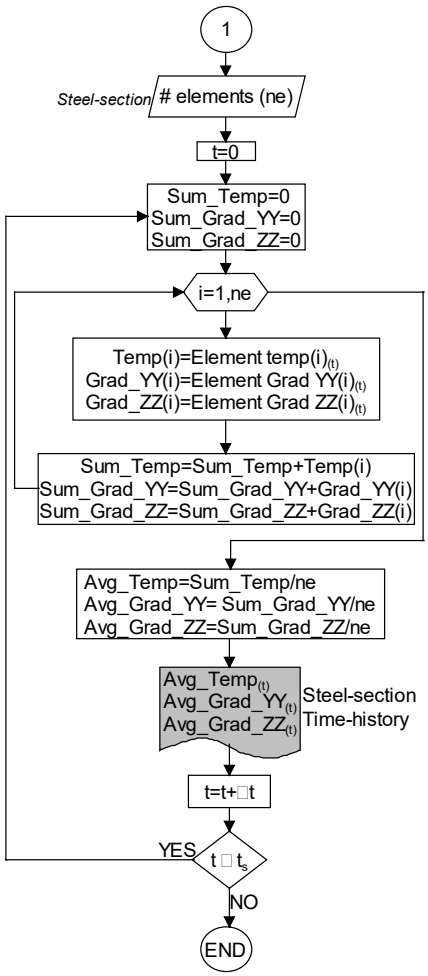

Fig. 9 Methodology for non-uniform temperature approach in a steel-section

3.6. Structural analysis of the framework

Since concrete only plays an insulating role in the framework, it only participates in the thermal resistance and not in the structural response. Therefore, the mechanical properties of concrete are not considered, only those of steel.

The real stress-strain ratio (σ-ε) of steel at high temperatures and the reduction factors k_{y},θ, k_{p},θ and k_{E},θ given by the EN 1993-1-2 standard, were used [64]. The yield stress of 408 MPa, the elastic modulus of 210 GPa, and the constant Poisson ratio of 0.3 were taken from [36]. The creep effect on the deformation of steel was considered implicit in the material model. The Ansys model multilinear isotropic hardening with temperature dependence was used, which can adequately represent the stress-strain relationships of steel with temperature (based

on Dounas and Golrand described in [66]). Variations of thermal expansion (α) of steel with temperature were also determined according to EN 1993-1-2 [64].

The thermal deformations introduced with thermal expansion (α) are very important in the mechanical analysis of the framework. Thus, the non-uniform field of temperature developed in the framework members sections by fire-action makes the material highly heterogeneous, resulting in additional bending deformations that increase with temperature.

In the Ansys structural analysis, geometric nonlinearity is activated to introduce the formulations of large deformations and deflections (GMNA). The convergence criteria for the solution of the nonlinear equations systems of the Newton-Raphson methods are defined. As concrete slabs and blocks only provide thermal insulation, they are not modeled in the structural analysis. The Cardington experiment reported that the joint remained intact and at lower temperatures than those measured at the beam and columns during the test; thus, the beam-column joint is considered rigid. The mechanical behavior of the half Cardington framework was modeled in 2D and 3D. Fig. 10 shows half of the steel 2D-framework idealization considering the symmetry. In the 2D model, XY-plane-frame restraints were included in all nodes. Additionally, the axial translation in the *x*-global axis and the rotation around the *z*-global axis at the beam mid-span were restrained considering the symmetry conditions; translations in the *x-global* and *y-global* directions were also restrained at the column bottom-end. Since the beam-finite element used for the modeling is 3D, translations in the *z-global* direction (out-of-plane) were restrained in all nodes in the 2D model. A bilinear spring with a nonlinear force-translation behavior was modeled at the position shown in Fig. 10 to represent the secondary framework constraint [30]. In the 3D model, XY-plane-frame restraints were released; additionally, symmetry condition at the beam mid-span remained (that means only translation in the *y-global* direction was allowed). Also, translations in three global directions and rotation about *y-global* direction were restrained at the column bottom-end in the 3D model.

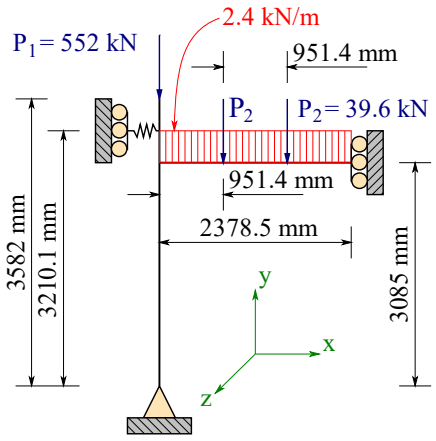

Fig. 10 Idealized Cardington framework

The meshing of the steel-beam and column cross-sections and the framework discretization with BEAM189 elements are shown in Figs. 11a and 11b. Half of the beam in Fig. 11c was discretized with five elements (*ne=5*), and the column was discretized with ten elements (*ne=10*).

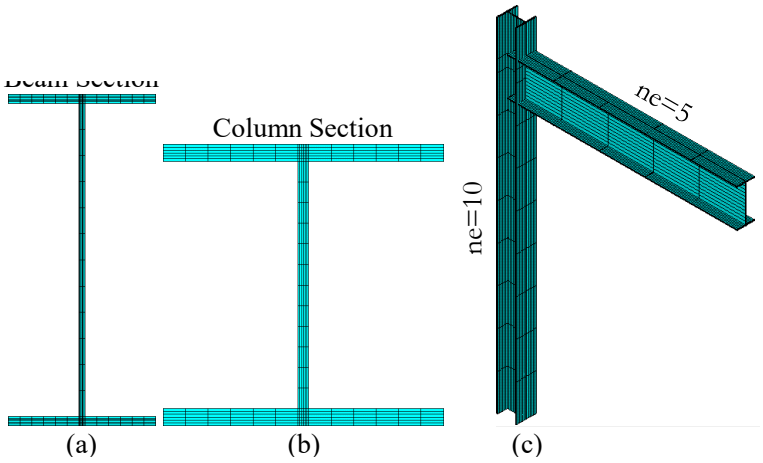

Fig. 11 Sections pseudo-meshing and BEAM189-framework discretization

Mechanical loads shown in Fig. 10 are applied at room temperature and remain constant during the fire. The non-uniform temperature in the steel-section is applied through the three time-varying components previously obtained from the procedure in Fig. 9. Besides, a linear variation of temperature in the beam length is considered. The longitudinal variation of the temperature in the beam is included through reduction factors (*fx*) determined by a sinusoidal function that varies between 0.90 (at the beam/column connection) and 1.00 (at mid-span), considering that the fire location is at the beam mid-span [30,64]. Based on the discretization of the half beam (see Fig. 11c), the reduction factors (*fx*) calculated at the mid-point of each BEAM189-element are shown in Table 1. Fig. 12 shows the approximation of the longitudinal temperature variation in half beam discretized with the five BEAM189 elements (*ne*=5).

Table 1. Temperature variation factors along the beam

	Relative distance	Length (mm)	Angle (x) (rad)	fx=sin(x)
Connection→	0.0	0.00	1.120	0.900
	• 0.1	237.85	1.165	0.919
	• 0.3	713.55	1.255	0.951
	• 0.5	1189.25	1.345	0.975
	• 0.7	1664.95	1.435	0.991
	• 0.9	2140.65	1.526	0.999
Midspan→	1.0	2387.50	1.571	1.000

The factor (*fx*) at the midpoint of each BEAM189-element is multiplied by the average temperature component (T_{avg} in Fig. 3b) to include the beam temperature longitudinal variation, as shown in Fig. 12. As the average temperature component applied to the BEAM189 section varies in time, the temperature in beam length also varies in time.

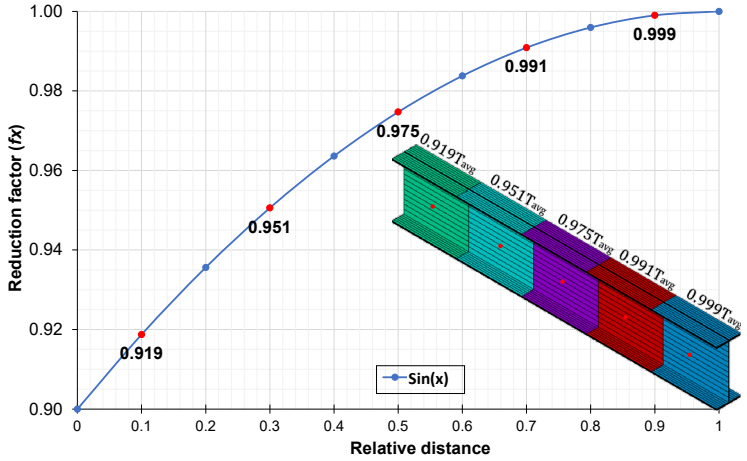

Fig. 12 Longitudinal temperature variation in half beam

The structural analysis under fire can be approached using a static pseudo-time scheme or a dynamic real-time scheme, including a quasi-static time integration method. In this methodology, a static pseudo-time scheme is used because the aim is to find the structure's fire resistance time and the structural response to this failure time, so a static analysis is enough for this purpose. However, the methodology can be used in explicit or implicit dynamic analysis introducing the appropriate command sequences. Fig. 13a shows the mechanical analysis flowchart, in which the average temperature and average thermal gradients results of the steel-section at each time obtained from the procedure illustrated in Fig. 9 are applied in the BEAM189 cross-section. Therefore, this approach can consider the different heterogeneous material behaviors produced by temperature changes in the section in time. This methodology can approximate the non-uniform temperature field in beam-type elements and is helpful for rigorously analyzing steel frames under fire, saving modeling and calculation times.

In the mechanical analysis in Fig. 13a: i) the structural members are the beams and columns; ii) each structural member has a single section (the member is prismatic over the entire length); iii) the geometric and material properties are assigned to each section, the section is assigned to each member, and loads are assigned to each BEAM189-finite element that discretizes the member; iv) all BEAM189-finite elements have a single section; v) the members are grouped by section, and the elements are grouped by member. In this way of working, as in object-oriented programming, heritages are transferred among objects, in this case, among sections, members, and elements. The analysis is defined through loops controlled by the following control variables: the pseudo-time (t), the number of sections counter (i), the counter of the members' number with the same section (j) and, the counter of elements number of each member grouped by section (k). The limits of these control variables are respectively: the pseudo total simulation time (ts), the number of sections (ns), the number of members ($nm(i)$) in the same section (i), and the number of BEAM189-elements ($ne(j,i)$) that discrete the member (j) with section (i). The number of sections (ns) controls the entire process since the section carries the nonlinearity of the material and the three time-history components that approximate the non-uniform temperature field. In general, $nm(i)$ is a size vector (ns), and $ne(j,i)$ is a matrix dimensioned from the largest number of members with the same section and the number of sections ($>$ nm(i),ns).

In this case study, there are two sections (*ns=2*) -Section 1 corresponding to the beam and Section 2 corresponding to the column-, so the loop controlled by the counter (*i*) goes from 1 to 2 (*i*=1,2). The number of members with Section 1 (beam cross-section) is *nm*(1)=1, and the number of members with Section 2 (column cross-section) is *nm*(2)=1, so the highest number of members with the same section is 1, and the cycle controlled by the counter (*j*) goes from 1 to 1 (*j*=1 to 1) for each section run. Therefore, the largest number of members with the same section is 1 (>nm(*i*)=1). The number of elements in Member 1 (beam) with Section 1 is *ne*(1,1)=5 and the number of elements in Member 2 (column) with Section 2 is *ne*(1,2)=10. The application of the procedure in the analyzed framework is detailed in Fig. 13b. The relations between the variables are shown in Fig. 13c, and the matrix forms of the variables *nm*(*i*) and *ne*(*j*,*i*) are presented in Fig. 13d.

The analysis procedure in Fig. 13a starts with the next entries: the number of sections in the structure (*ns*), the definition of the pseudo time step (Δt), and the total pseudo-time of the simulation (*ts*). The term pseudo-time refers to the static analysis incremental control that solves geometrical and material nonlinearity without the inertial effects of the dynamic schemes controlled by the real-time parameter [67]. The sub-process (1) starts with the section data entries through a loop controlled by the section's counter (*i*). In this loop (*i*=1 to *ns*), for each section, geometrical data (w_{f1},w_{f2},h_w,t_{f1},t_{f2},t_w, shown in Fig. 13e), the temperature-dependent material mechanical properties, and the number of members *nm*(*i*) with the same section (*i*) are entered. Then, through another loop (*j*=1 to *nm*(*i*)), each member (*j*) in section (*i*) is assigned: the member length L(*j*), the number of BEAM189-finite elements *ne*(*j*,*i*) that discrete the member, the section dimensions, the material properties, and the discretization are performed with BEAM189 elements. After assigning the boundary conditions to the model nodes according to the analysis dimension (2D or 3D) and the symmetry conditions, the sub-process (2) is started to assign the loads on the elements through a loop controlled by the elements counter (*k*) of each member (*j*) in section (*i*). In this loop (*k*=1 to *ne*(*j*,*i*)), the three components that approximate the non-uniform temperature field and the mechanical loads are assigned to each element (*k*). The reduction factor *fx*(*j*,*k*) is applied to each element (*k*) to discretize the longitudinal temperature variation. The uniform temperature component (Element Temp(*j*,*k*)) is the average section temperature (Avg_Temp(*i*)) multiplied by the factor *fx*(*j*,*k*), and the other two gradient components (Element Grad YY(*j*,*k*)) and (Element Grad ZZ(*j*,*k*)) are the average section gradients (Avg_Grad_YY(*i*)) and (Avg_Grad_ZZ(*i*)) respectively. Once the non-uniform temperature components have been applied, the uniform load on each element (*k*) and the nodal loads are applied. The sub-process (2) is carried out for each pseudo time (*t*) through nested loops controlled by the control variables (*i*), (*j*), and (*k*). Loops continue while the loads are assigned in all of the elements, and the nonlinear static analysis is performed for each pseudo-time step (Δt) up to the total pseudo simulation time (*ts*). Finally, the time-history results of the node displacements and the results in the elements are obtained.

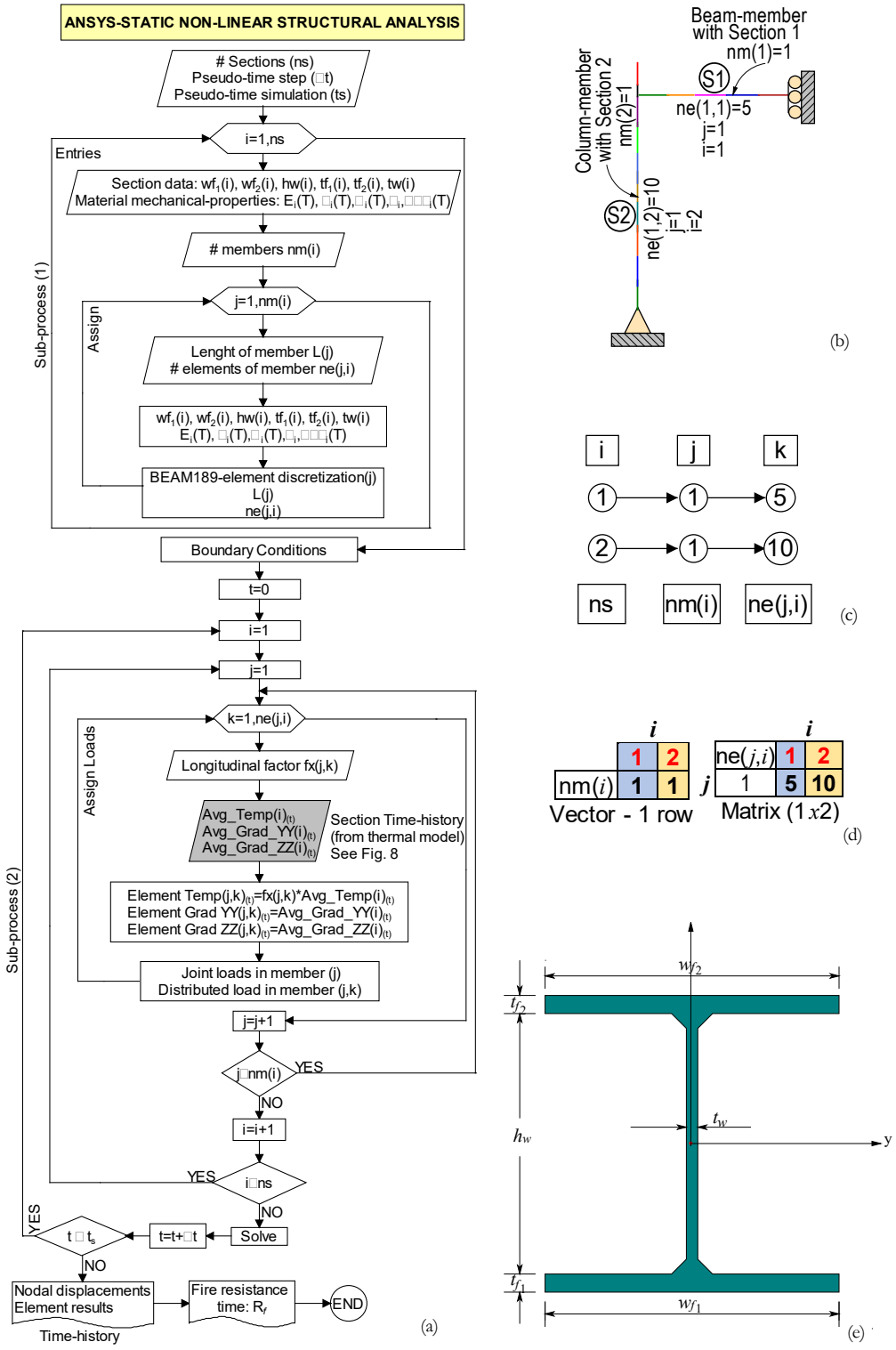

Fig. 13 Mechanical analysis flowchart

3.7. Thermal results of sections

Thermal results are temperatures and thermal gradients in the beam and column sections. In this case, the temperature is given by a field, T(Y,Z,*t*), so at each point (Y,Z) in a section, the two-dimensional field of the thermal gradient (TGy,TGz) shows the direction of

temperature rises. In contrast, the temperature gradient's magnitude determines how fast the temperature rises in that direction. The thermal gradient is directed from lower to higher temperatures. The gradient vector module is proportional to the temperature change per unit of length, °C/m (e.g., large vectors of thermal gradient correspond to those areas where the temperature changes quickly).

Figs. 14 and 15 show the temperature time-histories at three points (two on the flanges and one on the centroid indicated by the numbers 1, 2, 3) for the beam and column steel-sections. The temperature results at the three points obtained from the Ansys-heat transfer models (described in Fig. 8) compare very well with those of Franssen *et al.* and Santiago *et al.* done in Ceficoss, Safir, and Abaqus available in [30,35,36]. The temperature curves in the beam section top flange point and the column section web point are the lowest due to the concrete slab thermal insulation effect in the beam and concrete blocks in the column. Fig. 14 shows changes in the cooling speed at points 1 and 3 of the beam section. It can be seen that the highest heating rate during the first 25 minutes is on the web. After 25 minutes, the web cools faster than the bottom flange. In Fig. 15, the outer flange in the column has lower temperatures than the inner flange; therefore, the shadow effect is verified. This non-uniform temperature behavior influences the mechanical behavior of the framework.

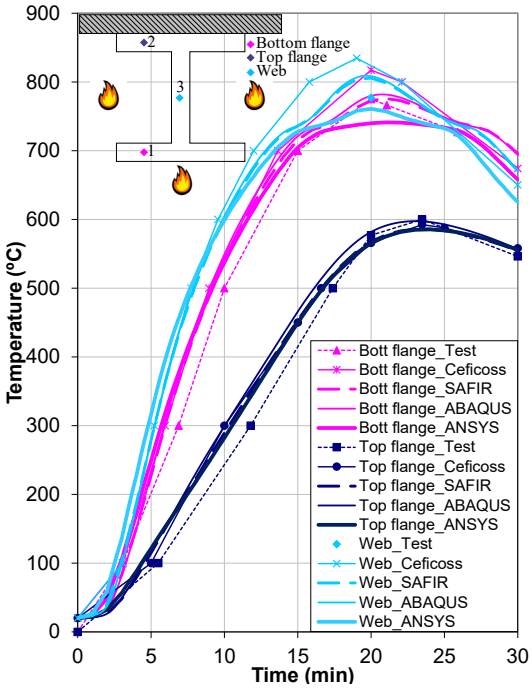

Fig. 14 Temperature at three points on the beam steel-section

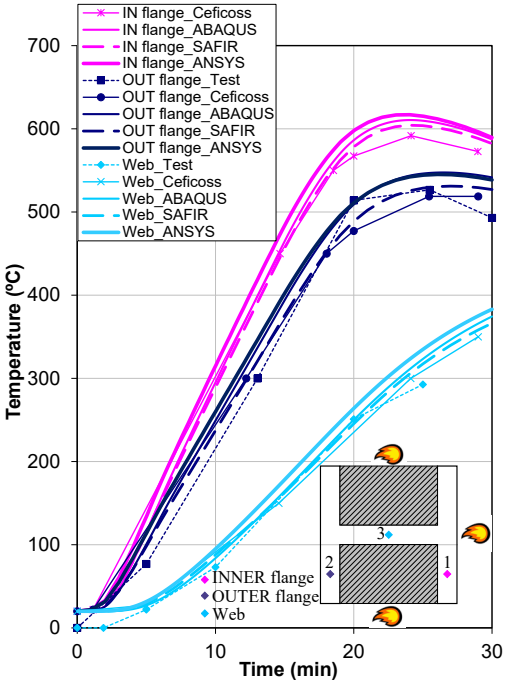

Fig. 15 Temperature at three points on the column steel-section

Figs. 16a and 17a show temperature isocontours in sections (including the concrete elements) at the end of the test (t=30 min). In Figs. 16b and 17b, the temperature isocontours in the steel sections more clearly show the temperature variation in the two directions, demonstrating the non-uniformity of the steel section temperature field. There is an apparent symmetry in the horizontal distribution that is not present in the vertical distribution. The web temperature profiles show the thermal insulation due to concrete elements and the shadowing

effect on the column outer flange. Since the sections are not heated uniformly around their perimeter, internal thermal gradients along the local ZZ axis (Figs. 16c and 17c) are important. E.g., the concrete slab creates non-uniform heating of the beam that causes the temperature to drop towards the slab (Fig. 16c), so an approximation of the temperature distribution in the beam section with a linear variation is adjusted. However, the non-uniform heating of the column cross-section created by the concrete blocks causes the web to maintain lower temperatures than the flanges, and the temperature in the section increases from the center of the web to the flanges. The shading effect on the outer face and the exposure to the inner face fire establish two temperature variations in the section; one that goes from the web center to the outer flange and another that goes from the web center to the inner flange. Therefore, the temperature distribution approximation in the column with a single linear variation can influence the prediction of the column lateral displacement; despite this, an approximation of the temperature distribution in the column section with a linear variation is acceptable (see Fig. 24). Horizontally (local YY-axis), the temperature variations are lower, so an approximation of linear variation in that direction is justified.

In Fig. 16c, the gradient sign on the entire web is negative; this means that the temperature increases from top to bottom in the Z-axis' negative direction as expected (see Fig. 16b). Similarly, in Fig. 17c, the gradient sign on the web is negative in the bottom-middle and positive in the top-middle since the temperature increases from the center to the web ends. That means the temperature increases in Z-axis's negative direction in the bottom-middle and Z-axis's positive direction in the top-middle, as expected (see Fig. 17b). In beam and column sections, it can be seen that: 1) the highest gradient values are at the ends of the web (just at the fillet), where the temperature values change more rapidly than other parts of the section, 2) in both flanges, the gradient slope changes because the gradient intensity becomes decreasing.

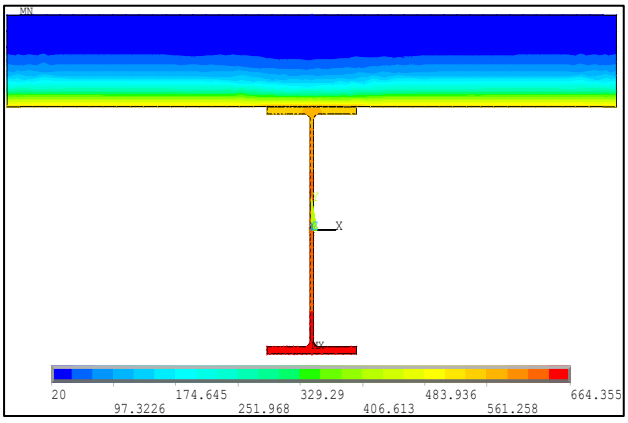

(a) Complete section temperature, [°C]

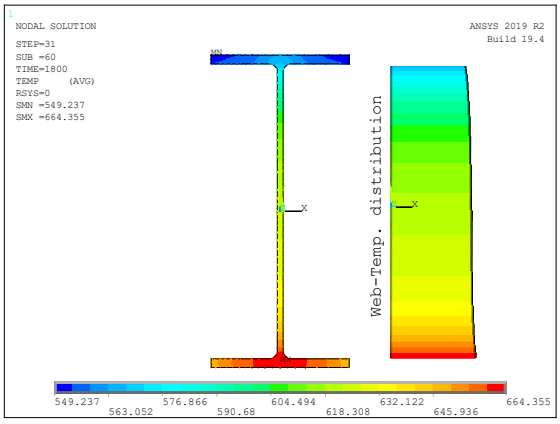

(b) Steel section and web detail, [°C]

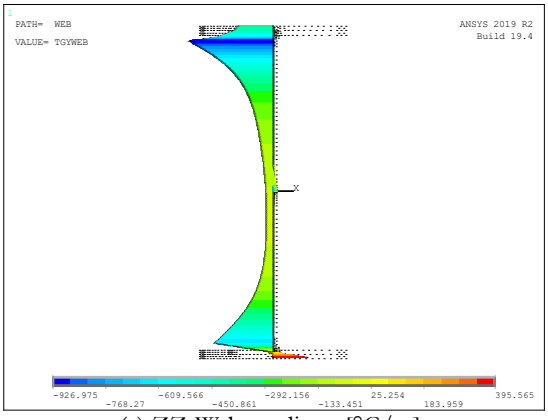

(c) ZZ-Web gradient, [°C/m]

Fig. 16 Temperature isocontours and ZZ-thermal gradient in the beam section at t=30 min

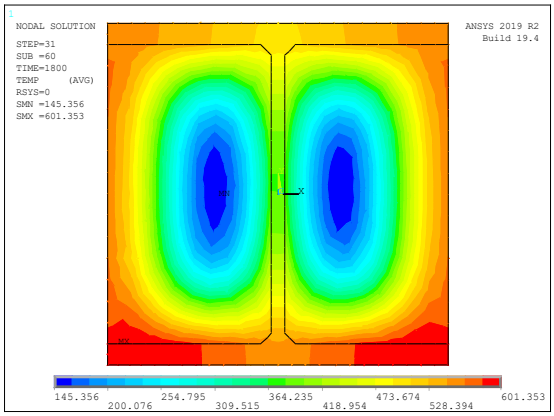

(a) Complete section temperature, [°C]

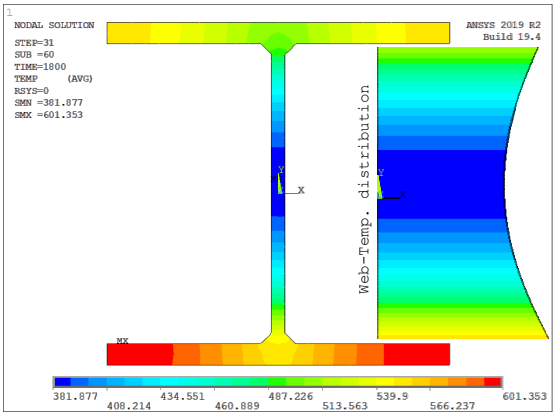

(b) Steel section and web detail, [°C]

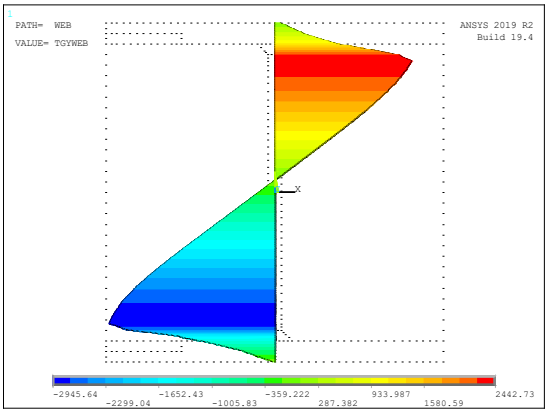

(c) ZZ-Web gradient, [°C/m]

Fig. 17 Temperature isocontours and ZZ-thermal gradient in the column section at t=30 min

Fig. 18 shows the horizontal and vertical thermal gradient isocontours in the beam steel-section for three representative times (5, 15, and 30 min). Fig. 19 shows the horizontal and vertical thermal gradient isocontours in the column steel-section for three representative times

(5, 20, and 30 min). The two gradients show an initial upward behavior. The beam gradients grew up to about 15 min and in the column up to about 20 min. Then, they begin to decrease until an almost uniform distribution of temperatures exists towards the end of the test (t=30 min).

Thermal gradients are element results and are located at the centroid of each PLANE35-element. Isocontours in Figs. 18 and 19 are the smoothed results of the sections' thermal gradients in the indicated times. In these results, small localized areas are observed (denoted by MN (minimum) and MX (maximum)) where the gradients achieve relative values that are high (positive or negative) and which indicate large temperature changes in a small region of the section. These are shown, e.g., in Fig. 19e, where there are small zones where the vertical gradient ZZ in the steel beam section achieves a minimum value MN of -5.87 °C/mm and a maximum gradient MX of 1.34 °C/mm. Also, in Fig. 19b, there are small horizontal gradient zones YY in the steel column section where the MN gradient is -2.65 °C/mm, and the MX gradient is 2.64 °C/mm. Figs. 18 and 19 show simultaneous positive and negative gradient values, which tend to balance out, resulting in almost zero positive or negative values.

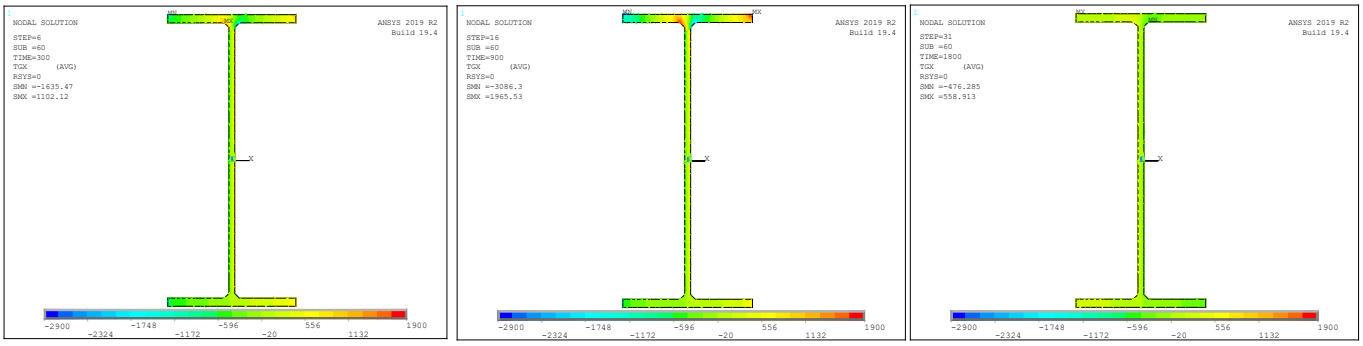

(a) YY-Gradient (t=5 min) (b) YY-Gradient (t=15 min) (c) YY-Gradient (t=30 min)

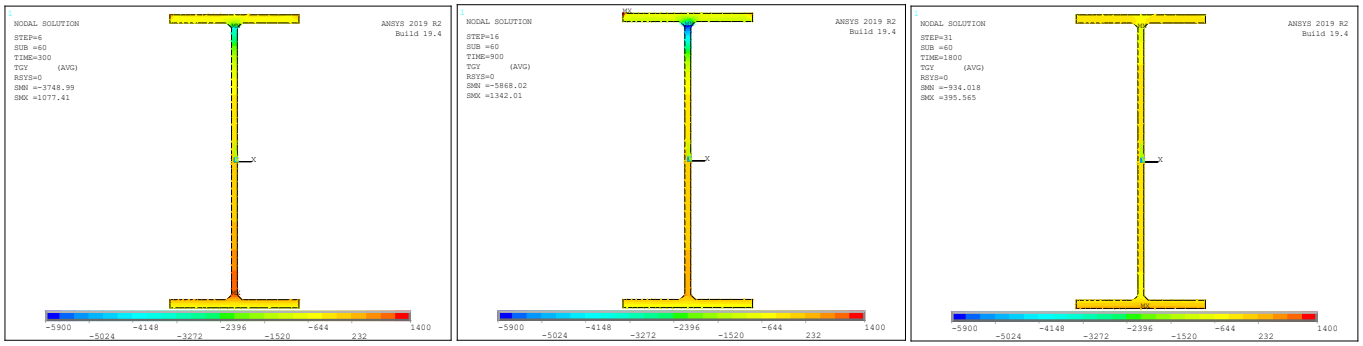

(d) ZZ-Gradient (t=5 min) (e) ZZ-Gradient (t=15 min) (f) ZZ-Gradient (t=30 min)

Fig. 18 Isocontours of YY-horizontal gradient and ZZ-vertical gradient in the I-profile section of the steel beam, in °C/m

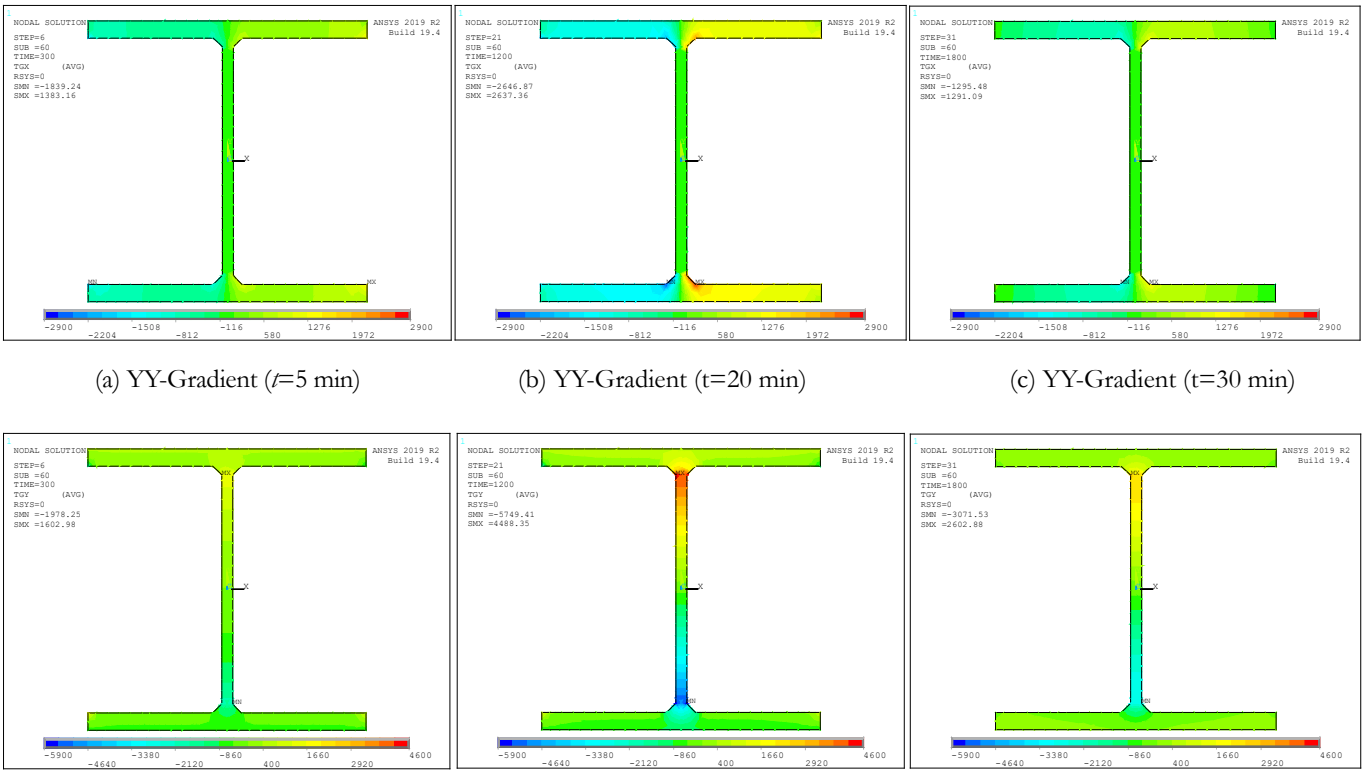

(a) YY-Gradient (t=5 min) (b) YY-Gradient (t=20 min) (c) YY-Gradient (t=30 min)

(d) ZZ-Gradient (t=5 min) (e) ZZ-Gradient (t=20 min) (f) ZZ-Gradient (t=30 min)

Fig. 19 Isocontours of YY-horizontal gradient and ZZ-vertical gradient in the I-profile section of the steel column, in °C/m

Meanwhile, Figs. 20a and 20b show the average thermal gradient histories of the steel sections in the beam and the column, where most of the time, the resulting gradient is negative, indicating that the temperature decreases in the direction of the concrete slab in the beam and, the direction of the outer flange in the column due to the shading effect. In Figs. 20a and 20b, average thermal gradients are not constant in time, and their behavior is different in the heating and cooling phases. Fig. 20a shows that thermal gradients magnitude increases and decreases in the heating and cooling stage, respectively, i.e., gradients magnitude increases from start fire up to 15 min in the beam section and 17 min in the column section; then, gradients magnitude decreases until the end of the fire. Hence, knowing the gradients' behavior in the whole fire scenario is important mainly for the subsequent three-dimensional analysis of post-buckling or collapse, which can occur in the cooling phase [68].

In Fig. 20a, the average ZZ gradient values (in the web) of the beam section are higher due to the asymmetry of the section in the vertical direction: $\langle \frac{\text{concrete}}{\text{steel}} \rangle$, while the low average gradient values YY are due to the section symmetry in the horizontal direction: ⟨steel|steel⟩ on the bottom flange, and $\left\langle \frac{\text{concrete}}{\text{steel}} \middle| \frac{\text{concrete}}{\text{steel}} \right\rangle$ on the upper flange. The average ZZ gradient values (in the web) of the column section are lower than those of the beam because of the concrete blocks between the flanges that protect the web from the high fire temperatures.

In Fig. 20b, the horizontal average gradient values YY in both sections show a more uniform behavior. They are lower than the vertical ones, with the maximum horizontal average

gradient being one-seventh of the maximum vertical average gradient in the beam and half in the column. Although the horizontal average gradient values YY are similar in both sections, it takes only 5 min for the beam to get the maximum value. In comparison, the column takes 15 min to get the same value. In both sections, horizontal average gradient YY values are lower than those of vertical average gradient ZZ; however, it was confirmed that horizontal gradients are indispensable in approximating the section's non-uniform temperature distribution. Not including them creates problems of non-convergence of the solution. In Fig. 20a, the vertical gradient peaks ZZ in the beam and column sections are presented at t=15 and t=17 min, respectively. It can be seen that when the gradient is maximum, inflection points occur in the deflection curves of the beam and column where the deflection rate increases (see Fig. 24). This drop in the average values of the ZZ gradients is due to two considerations: i) the drop in the gas temperature in the compartment from t=15 min (see Fig. 6), and ii) the decrease in the steel thermal conductivity with the temperature.

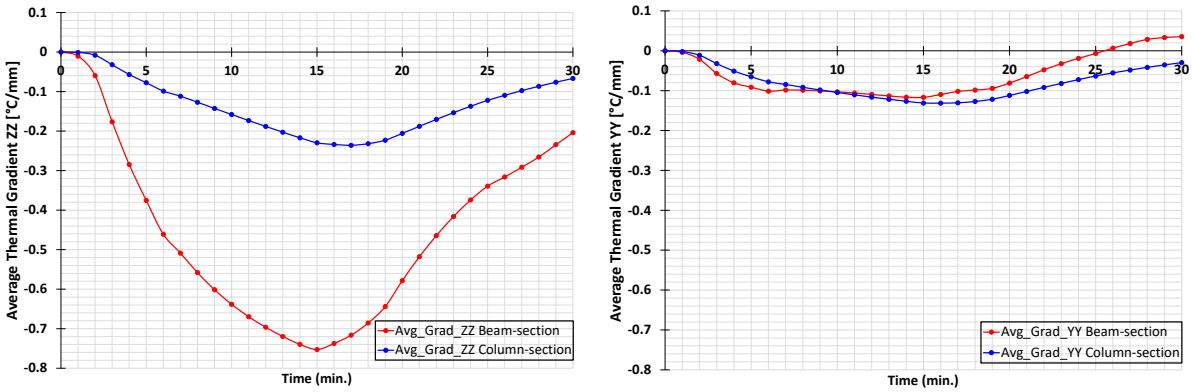

(a) Time-history of ZZ-vertical average gradient (b) Time-history of YY-horizontal average gradient

Fig. 20 Average transversal gradient time-histories in the steel sections of the beam and column

Figs. 21a and 21b show for the three points on the flanges and the web centroid of the beam and column sections (indicated by numbers 1, 2, and 3) the temperature histories calculated in the thermal model against temperature histories applied in the structural model using the proposed methodology. Temperatures applied at these points (for each time) are approximated by Eq. (1). According to this equation, the average section temperature is applied at the centroid where gradients are null so that, at the centroid, the temperature applied is the average section temperature. Figs. 21a and 21b show the average temperature histories $T_{avg}(t)$ at the centroid of the beam and column sections used in the methodology for approximating non-uniform temperature in the section. Although these average temperatures are applied at the centroid, the $T_{avg}(t)$ curve is not compared with the calculated temperature curve at the centroid in the thermal model because they have different meanings. I.e., the average section temperature applied at the centroid represents the uniform temperature component used to approximate the temperature applied at one point of the section in the structural model, which does no-match the centroid temperature calculated in the thermal model. Besides, the temperature time-history curves calculated in the thermal model and those applied in the structural model (at the two points of the flanges) do not match. That is because the applied temperature field using the average temperature and the two average gradients of the section

are approximations that balance the over and under errors in the section domain at each time step.

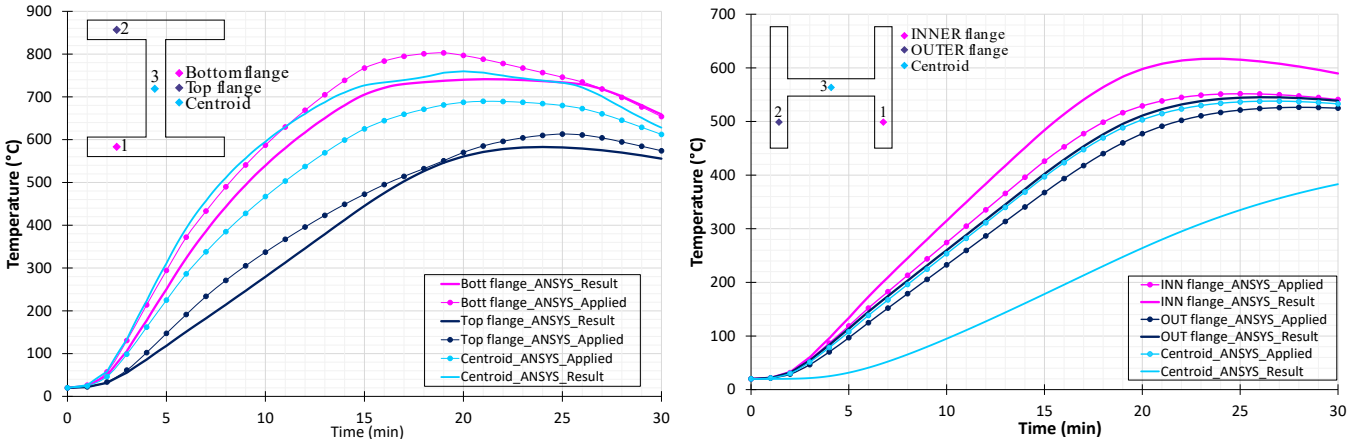

(a) Beam steel section (b) Column steel section

Fig. 21 Time-histories of average temperatures calculated and applied at three points in the sections

By approximating the non-uniform temperature distribution in the section (a curved surface in space) through an average oblique plane, points of temperature above and below the plane (overheating in some cases and underheating in others) are located that balance the result in each time step. Figs. 22 shows this situation for a time t=15 min in the beam section and for a time t=20 min in the column section. These two figures represent the temperature curved surfaces from the thermal model calculations and the average temperature planes used in the methodology to approximate the non-uniform temperature in the structural model sections. On the surfaces, the isocontours indicate the temperature values, and the surface slopes represent the thermal gradients.

E.g., in the beam section (Fig. 22a), the high slope of the temperature surface at the web reproduces the high vertical gradient value in the Z-direction. In contrast, the low slopes at the flanges denote the low horizontal gradient values in the Y direction. In the column section (Fig. 22b), high slopes are observed over the flanges and the web that mean high values of the horizontal and vertical gradient in the Y and Z directions, being the gradients in the web larger. This situation is verified by the gradient distributions in Figs. 18b and 18e on the beam and Figs. 19b and 19e on the column. On the other hand, the result of the approach-plane cut in the temperature surface explains the temperature balance. Above means, in the centroid of the section, the plane height is equal to the average section temperature, and the slope of this plane in each direction (Y and Z) coincides with the values of the average gradients (horizontal and vertical) of the section. E.g., in the beam section (Fig. 22a), the Z-direction slope approaching-plane is higher than the Y-direction slope. In the column section (Fig. 22b), the slopes of the temperature approaching plane in the two directions (Y and Z) are more similar to each other because of the section symmetry. The highest average gradient values are in the Z-direction and the lowest in the Y-direction. The temperature surfaces are helpful insofar as they allow the influence of boundary conditions on the section to become evident. E.g., when comparing Figs. 22a and 22b, it is observed that the impact of the radioactive shadow on the steel thermal gradient (in the column) is less than the concrete boundary condition effect (in the beam).

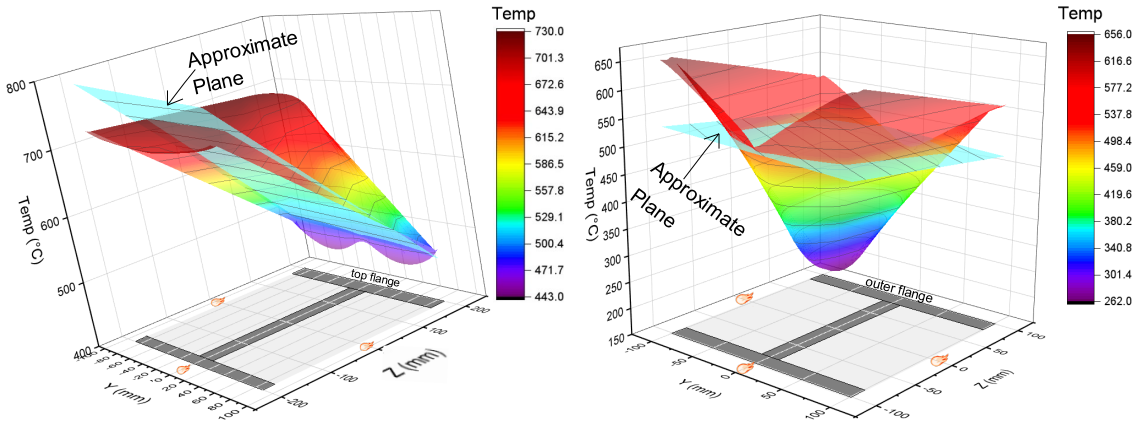

(a) Beam steel section (t=15 min) (b) Column steel section (t=20 min)

Fig. 22 Calculated temperature surfaces and applied approximate temperature planes

3.8 Framework's mechanical results

In this work, three different mechanical models have been done to validate and verify the proposed methodology:

- A 2D model with the spring shown in Fig. 10, whose calibration allows representing the bending of the beam-column assembly properly. This 2D model was done to verify the 2D simulations of the experiment carried out by Santiago *et al.* available in [36].
- A 3D model with the same spring as the 2D model mentioned above. This model is necessary to check 3D effects such as section warping and flexural-torsional buckling that can appear in frames at elevated temperatures and cannot be captured with 2D models.
- A springless 3D-model for evaluating the influence of the subsidiary framework lateral resistance on the three-dimensional fire response of the framework.

The validation of the proposed methodology is carried out based on the following results of: (a) the Cardington test, which are included in the Latham *et al.* report [61,62], and (b) the 2D-numerical simulations of the experiment carried out by Santiago *et al.* [36]:

- Maximum deflection in midspan beam.
- Lateral displacement at column mid-height.
- Column end extension.
- Fire resistance time.

Lateral displacement at column mid-height and column end extension are both new analyses that make it possible to validate the proposed methodology and take advantage of the 3D-modeling capabilities using 3D-beam finite elements.

Fig. 23a compares the experimental beam mid-span deflections with those obtained by Santiago *et al.* [35,36] and the three proposed mechanical models. It is observed that all models make a good prediction. Safir results match those of the Ansys-3D models up to about the

16th minute. The 2D model, on the other hand, is closer to results given by Ceficoss and Abaqus. Fig. 23b compares only the lateral (central) displacements at half the column height obtained with the different programs. All deflection predictions are in the centroid. It can be seen again that the results obtained with all of the models are similar.

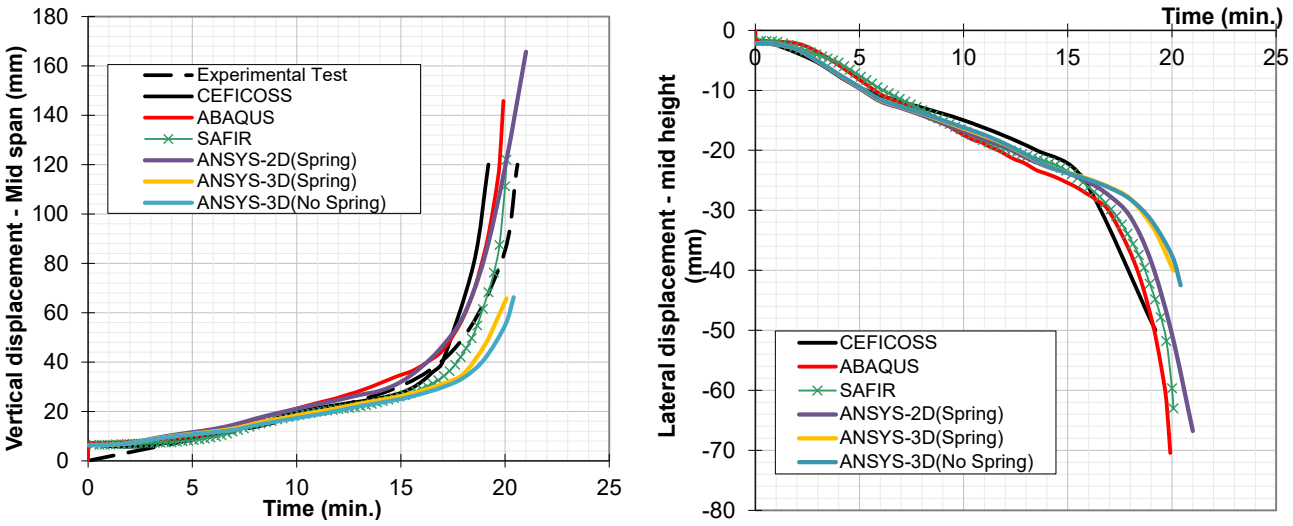

(a) Max. vertical displacement - beam midspan

(b) Lateral displacement - column mid-height

Fig. 23 Deflection comparison of the framework members (centroidal results)

Fig. 24 compares the lateral displacement at column mid-height measured by the extensometer (located about a quarter of the outer flange width: ¼*w*) with those obtained from the Ansys-3D models. Deflection predictions are obtained outside the centroid at the extensometer position located on the column's outer face.

It is observed that, in the first 16 minutes, the calculated deflections are higher than measured, probably because the approximation of linear variation of the temperature in the section does not completely represent the bi-laminate effect. This effect is the curvature produced by expanding the heated inner face when the section perimeter temperature is not uniform. The bi-laminate effect in the column, in turn, produces a balancing of internal forces by the temperature that makes the deflections in the column laterally smaller, as observed in the measurements of the experiment. However, it is essential to note that from 17 minutes (the same time of the average vertical gradient peak ZZ, see Fig. 20a and until the final failure time, the prediction of lateral displacement of the column is very close to the experiment (in the cooling zone, see Fig. 6).

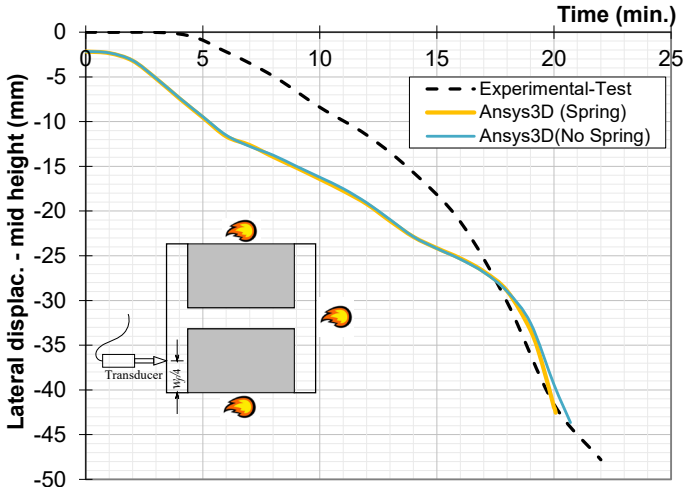

Fig. 24 Lateral displacement - column mid-height, (¼w_f)

Figs. 25a and 25b show the lateral displacements at mid-height of the column at three points located on the outer face in the Ansys-3D models at t=20 min. The 39.43 mm model prediction without spring (in the extensometer position, indicated in red color) compares very well with the 41.6 mm reported in the experiment. If the spring is included, the prediction slightly increases to 41.3 mm, closer to the experiment value. These non-centroidal results are calculated into the pseudo-mesh nodes of the BEAM189 element section. Results querying in the nodes of the finite element outer face (in extruded view) are possible by interaction with the results' database in the pseudo-mesh nodes of the section.

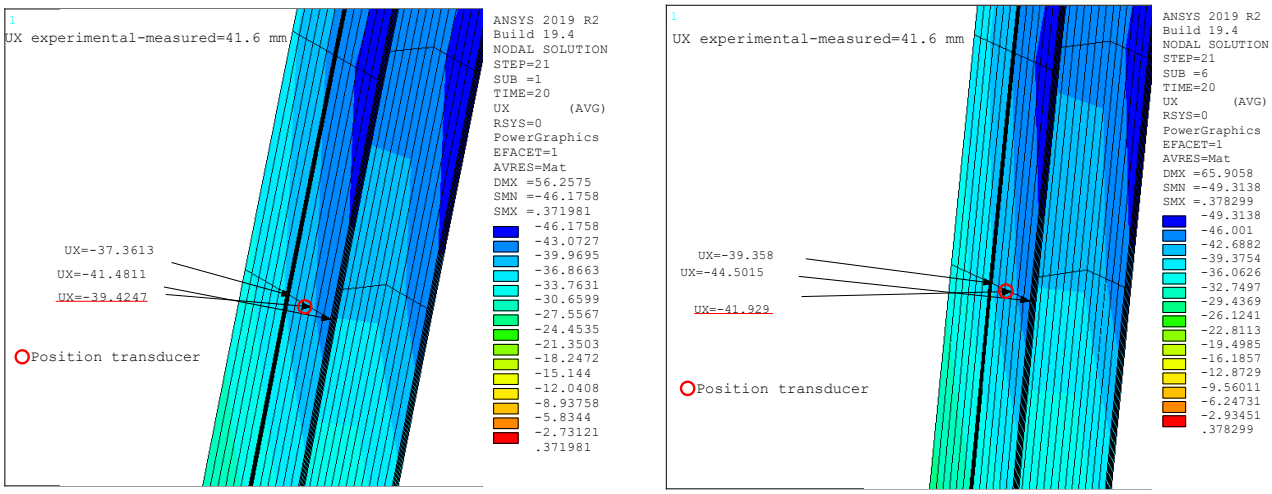

a) Ansys-3D (No Spring) model (b) Ansys-3D (Spring) model

Fig. 25 Lateral displacement on outer face (w_f/4) - column mid-height (t=20 min), in extruded view

Table 2 shows the fire resistance time according to the simulations carried out by Santiago *et al.* [35,36] and by the authors with the new methodology implemented in Ansys. The results are compared with the fire resistance time of 20'36" reported in the test. It is observed that the

Ansys-3D (No Spring) model gives the best prediction, although the results are similar for all the Ansys structural models.

Table 2. Time of fire resistance (R_f)

Numerical model	R_f	Ratio (Num./Exp.)
Ceficoss	19'12"	0.93
Safir	20'04"	0.97
Abaqus	19'51"	0.96
Ansys-2D (Spring)	21'00"	1.02
Ansys-3D (Spring)	20'04"	0.97
Ansys-3D (No Spring)	20'28"	0.99

Finally, Table 3 shows the CPU time for the three models built in Ansys using parallel distributed memory-MPI calculation in 6 physical cores on a Dell Mobile Workstation 7530/64 bits, Intel Xeon Processor-2.71 GHz, and Ram-32 GB. Despite the high nonlinearities present, the results show that CPU times are low in the three models (less than 1 minute).

Table 3. Calculation time for Ansys models

Numerical model	CPU Time (sec)
Ansys-2D (Spring)	27.000
Ansys-3D (Spring)	40.625
Ansys-3D (No Spring)	32.938

From the analysis carried out, the capacity of the three models developed in Ansys with the strategy presented in this paper to correctly predict the response of the framework with a low computational cost is concluded. Considering that the two framework 3D-models' deflections predictions are practically the same, the following results focus on analyzing the Ansys-3D (No Spring) model results as it is the model that includes 3D-phenomena that better approximates the failure time and has the smallest CPU cost.

Fig. 26 shows the vertical deflection predictions at two points in the middle and corner top end of the outer flange (column end extension). The test report exactly no-specified the extensometer position, so it was assumed from the photographic evidence it was the midpoint. Both predictions show similar behavior to that measured in the experiment. The 20.68 mm calculated in the middle flange at t=20 min is closer to the 20.6 mm measured in the experiment. At the outer end of the flange, the computed value is 22.04 mm. The differences between the measured and simulated values depend on the experimental measurement point location as the section is rotated.

A detail of the extruded column end is shown in Fig. 27. The colors of the vertical displacement isocontours (t=20.47 min) at the end of the column indicate the section rotation (differential displacements at all of the section points are not constant). This situation affects the measurement of vertical deflection.

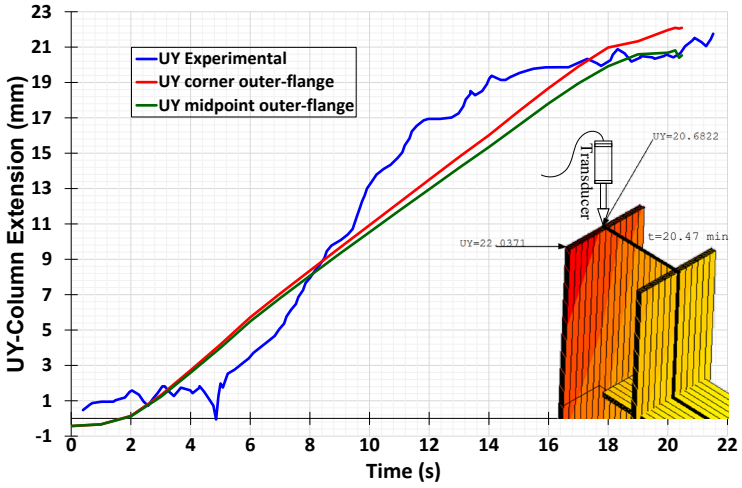

Fig. 26 Column end extension in two points (*t*=20.47 min)

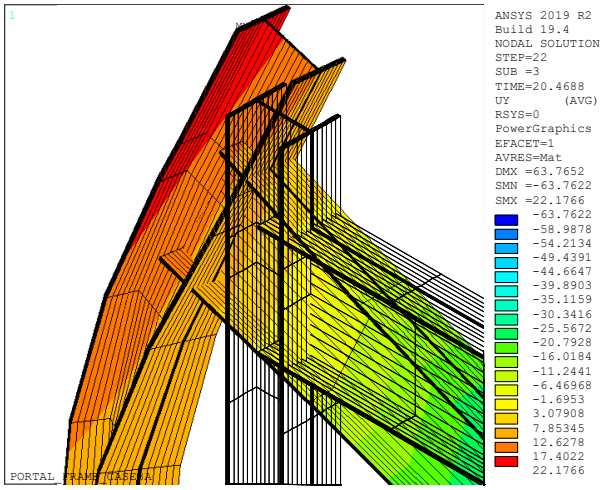

Fig. 27 UY-displacements in the column end (t=20.47 min), in extruded view

Fig. 28 shows the lateral column deflections (UZ) perpendicular to the plane of the framework. Deflections are calculated at the mid-height and the top end of the column. Initially, the values are small, and as time goes by, when the material weakens by fire, sectional warping and buckling appear, which can compromise the column stability. Some oscillations and startles are observed in small time fractions at the final times, allowing some instability to be inferred. The UZ values in the mid-height of the column are positive, and those at the top-end are negative, indicating inflections.

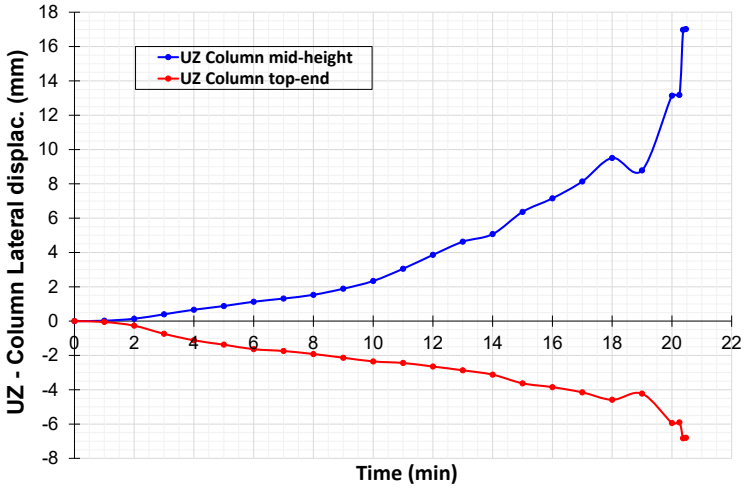

Fig. 28 Normal column displacement (t=20.47 min)

Fig. 29 shows the applied temperature distribution to the frame (t=20.47 min) using the non-uniform temperature approximation in the sections and the temperature reduction factors in the beam length. The different colors indicate the different temperature values in the sections and along the beam. With these temperature loads applied adequately in space and time through the proposed methodology, mechanical results are obtained reasonably adjusted to the structural response measured in the laboratory (see Figs. 23 to 26). The applied temperature values (806 °C in the beam and 605 °C in the column) look like the maximum temperatures calculated in Figs. 14 and 15.

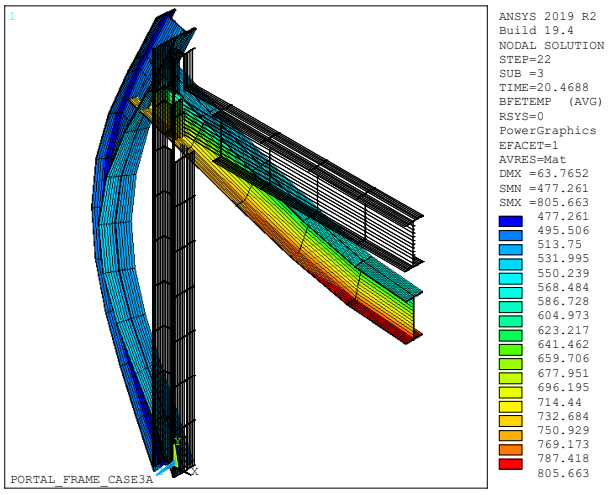

Fig. 29 Non-uniform temperature applied (t=20.47) min), in extruded view

Fig. 30a shows the 3D deformation of the frame. A buckling is identified in the column of greater intensity towards the end time of the test. In the front view (Fig. 30b), a flexural-torsional buckling is also observed in the column, which can only be seen when the complete framework response is modeled in 3D. The structural response shows that the non-uniform

temperature field in sections and elements affects the structure displacement field in all three dimensions.

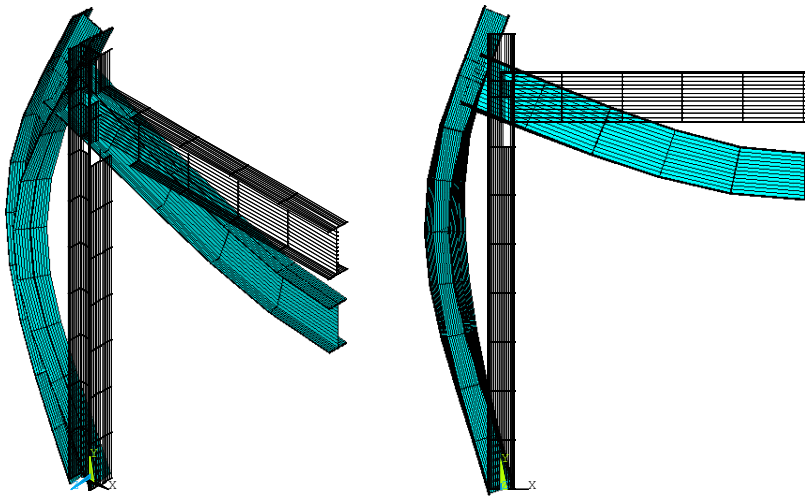

(a) Deformed-isometric view (b) Deformed-frontal view

Fig. 30 Flexural-torsional buckling (t=20.47 min), in extruded view

Fig. 31 shows the three-dimensional displacement field presented in the framework by the simultaneous action of applied loads, the deformations due to non-uniform temperatures, and buckling phenomena due to high temperatures. The following reasons can cause the latter: i) the weakening of the material, ii) imperfections or second-order phenomena (instability because of large deformations which appear due to considerable differences between deformed and non-deformed shape) and, iii) the coupling of the displacements because of heterogeneity created in the material by the internal thermal gradients (under the fire action, each cross-section becomes composed of a large number of different materials due to the different mechanical features which occur at each temperature, at each time and each point of the section [69]). In Figs. 31a to 31f, it can be seen that all the degrees of freedom vary within the section of the elements, confirming that the displacement field is 3D. Furthermore, the column rotation in the three global directions, *x*, *y*, *z*, demonstrates a biaxial stress state. In this case study, two bending planes are generated (produced by moments, buckling, flexural-torsional buckling, warping, and temperature), which cannot be considered when the frame is modeled for a 2D-displacement field.

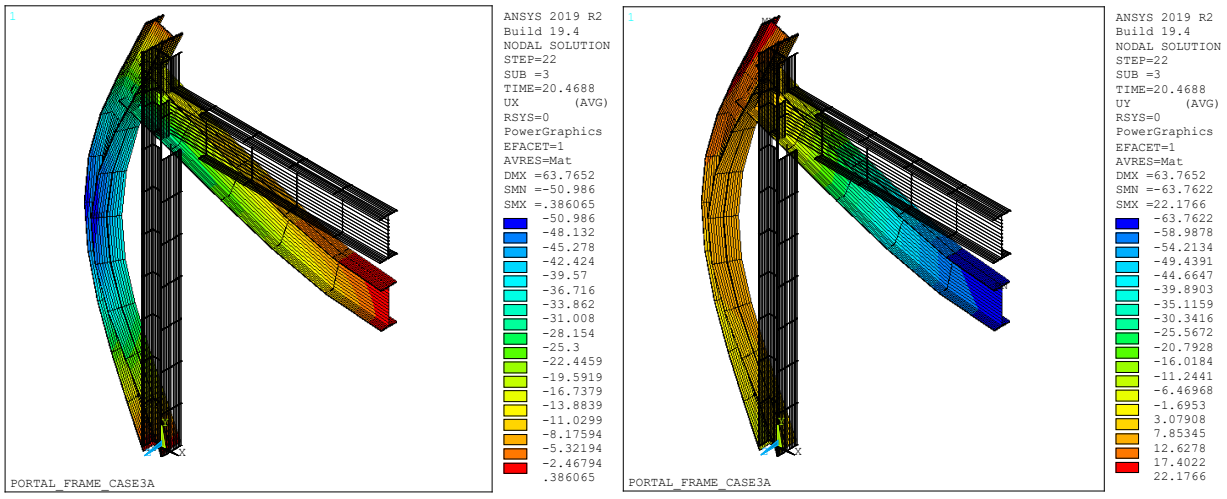

(a) *x*-translation (mm) (b) *y*-translation (mm)

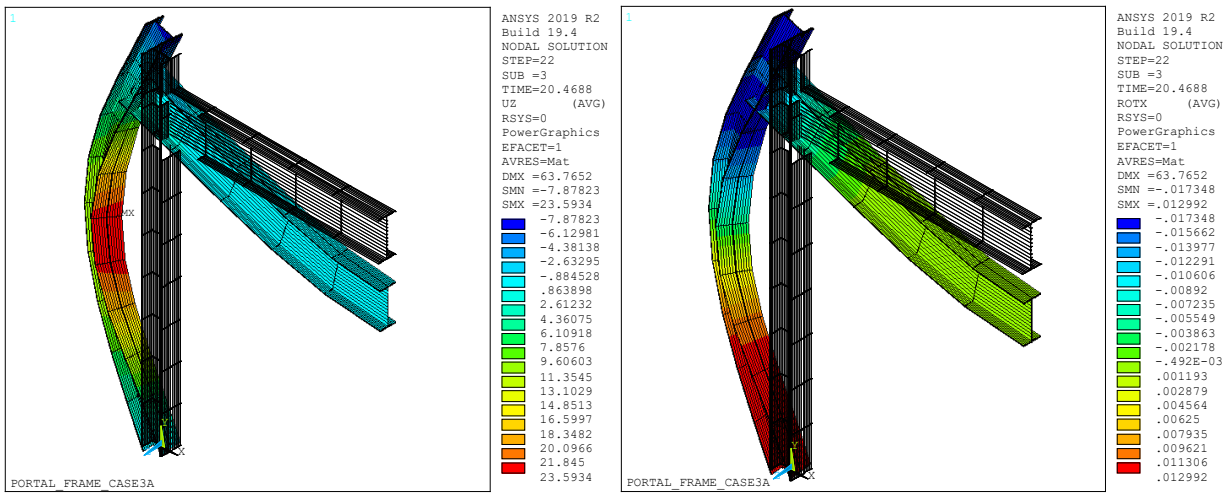

(c) *z*-translation (mm) (d) *x*-rotation

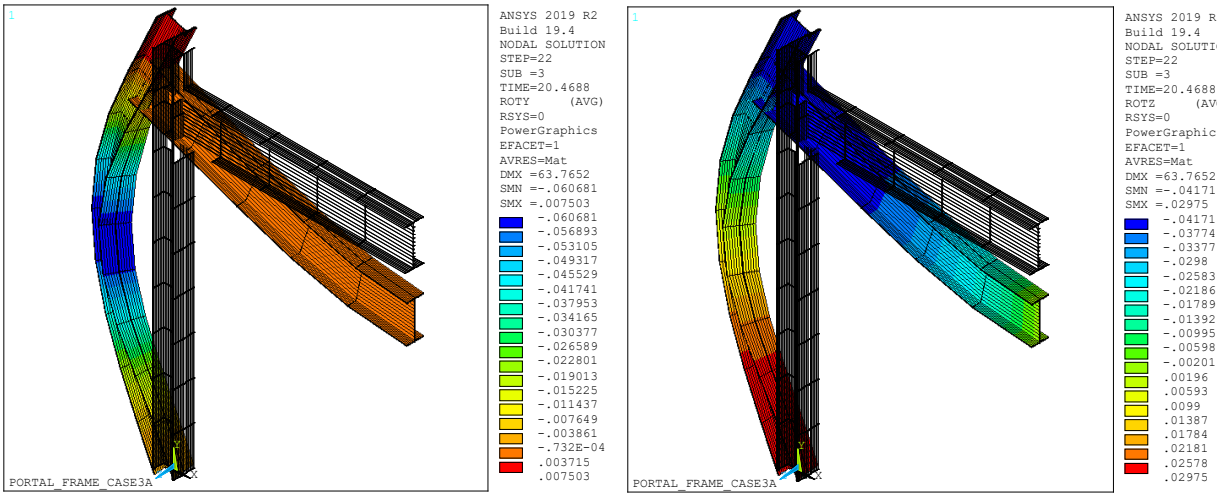

(e) *y*-rotation (f) *z*-rotation

Fig. 31 3D-displacement field isocontours (t=20.47 min), in extruded view

The displacements by the steel-ductility and the thermal expansion cause plasticization of the material. Figs. 32a and 32b show the Von Mises plastic deformations produced by the action of mechanical loads and temperature loads (t=20.47 min), respectively. It can be seen that the order of magnitude of the plastic deformations produced by mechanical loads and those created by temperature loads in the final fire resistance time is very similar. Approximately 50% of the framework plastic deformation is produced by mechanical loads and the other 50% by temperature loads. Consequently, temperature deformations are significant for calculating the framework deformation field and studying its mechanical behavior.

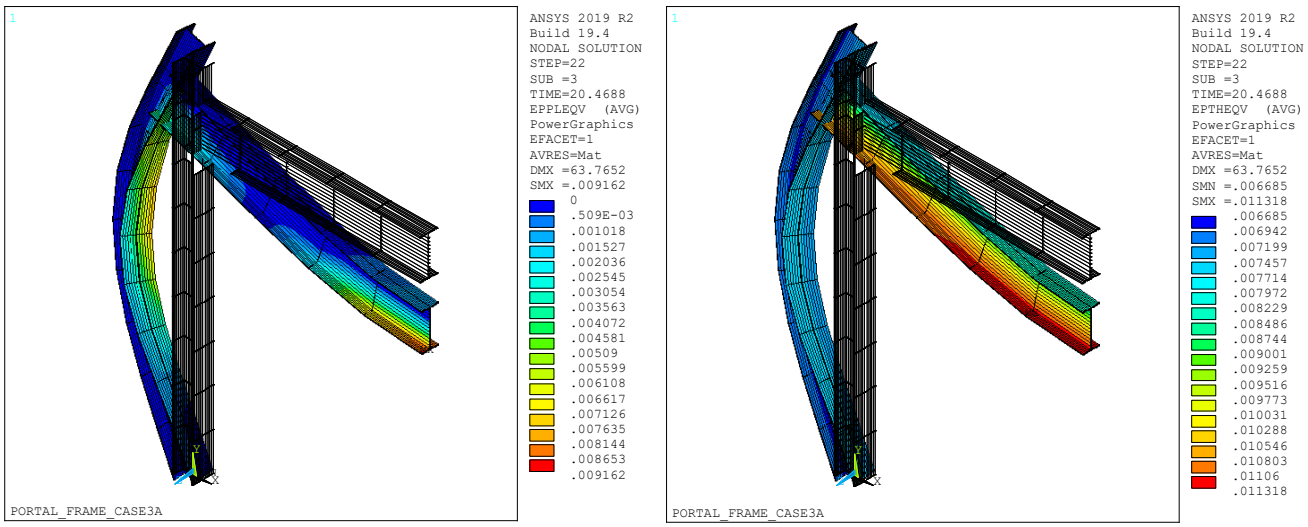

(a) Plastic deformation due to mechanical load (b) Plastic deformation due to temperature load

Fig. 32 Von Mises plastic deformations in the framework (t=20.47 min), in extruded view

Results of warping, bicurvature, and bimoment are important insofar as they allow inferring the presence of possible flexural-torsional buckling in places where large changes in the angle of torsion occur, suggesting zones of local instability in the members of the structure. Fig. 33 shows the warping behavior in the frame (t=20.47 min). This effect is relevant as the open sections of the framework decrease the torsional stiffness with increasing temperature. Fig. 33a shows warping due to high temperatures, mainly in the column, verified with the bicurvatures and bimoments shown in Figs. 33b and 33c, respectively. The influence of warping in the simulation is more remarkable in the column than the beam because there was no restriction to warping (since there were no point loads along the column). For stability considerations, warping had to be restricted towards the beam midspan (due to the applied loads), precisely where the beam distortions were significant, according to the experiment. Solvers with greater capacity to overcome the convergence problems caused by the instability resulting from the high fire nonlinearity are necessary to get better results from the beam warping.

The torsional rotation results, warping, bicurvature, and bimoment, are related to each other and make sense when analyzed together. I.e., since warping is the first derivative of torsional rotation, the zero-warping point is where the maximum torsion occurs (in the column, it is between the positive and negative warping points). This condition is verified in the middle zone of the column when Figs. 31e and 33a are compared. Similarly, being the bicurvature, the

first derivative of the warping, and the bimoment a function of the bicurvature, the two points of maximum and minimum value of warping present in the column (Fig. 33a) match the points of zero bicurvature shown in Fig. 33b. The bicurvature is significant at the column middle and upper zones where the lateral bending is registered (see Fig. 30). The column positively twists in the middle of the column and negatively at the end. Bicurvature signs indicate changes in the direction of twisting along the column. The almost constant values of bimoment in the central zone of the column in Fig. 33c just in the region where the bicurvature is maximum (between the positive and negative warping) suggest that in this region, the rotated sections no longer present large relative changes of position or shape between them.

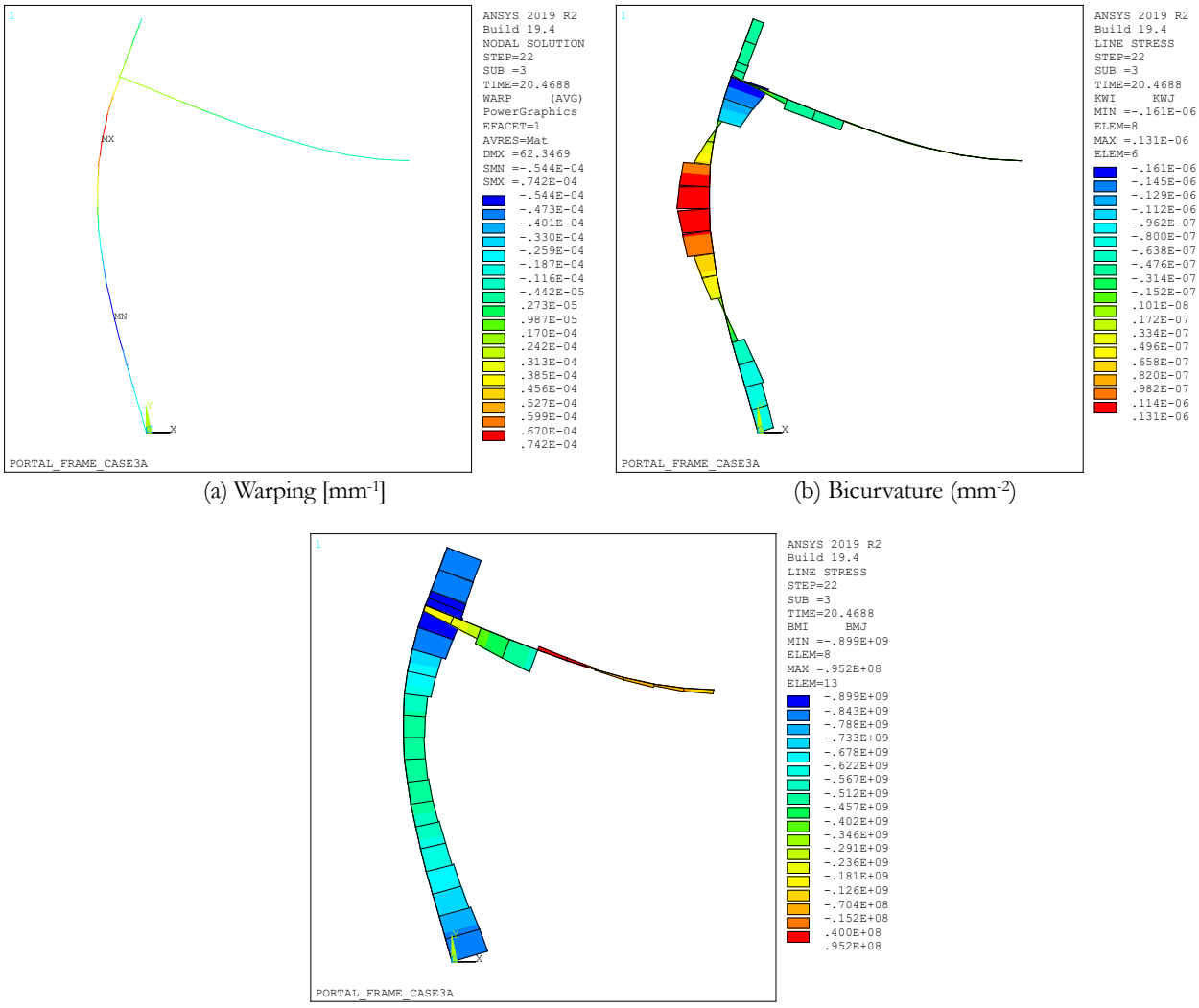

(a) Warping [mm^{-1}] (b) Bicurvature (mm^{-2})

(c) Bimoment (N-mm^{2})

Fig. 33 Flexural-torsional effects in the framework (t=20.47 min)

Chapter 4

NEW PROPOSALS FOR MODELING LATERAL-TORSIONAL BUCKLING IN CLASS-4 STEEL MEMBERS AT ELEVATED TEMPERATURES USING BEAM-TYPE ELEMENTS

This chapter includes sections 1 to 6 from paper "New modeling strategies for analyzing lateral-torsional buckling in class-4 steel structural members at elevated temperatures using beam-type elements" published in the December 2021 issue of the Journal Structures, vol. 34; p 3508–3532. https://doi.org/10.1016/j.istruc.2021.09.087.

4.1 Justification and antecedents

Current requirements for building structures and large-scale roadway structures, such as bridges, are becoming increasingly demanding, requiring elements of larger dimensions that make them more costly [70]. On the other hand, current trends in the construction of large-scale projects have made steel structures a major construction alternative [71]. The inevitable need to optimize costs under allowable performance levels has greatly interested in using lighter sections. Recent cases demonstrated it. For example, in the Wirkowice bridge in Poland (2020), hot-rolled high-strength lightweight steel sections were used to reduce the weight and increase the bridge span [2]. Another illustrative case is Chicago's Union Station Tower (2020). In this 51-floor office steel building, designers reduced the total structural steel in the upper perimeter columns by almost 20% using stronger but lighter steel elements (552 MPa), creating more open space in upper floors [3].

However, the decrease in the amount of material in the fabrication of steel members to make them lighter also makes them slenderer. That condition may compromise the structure's stability because of the possible activation of global or local buckling failure phenomena that, in practice, are more critical when the structure is in a fire situation [4]. Examples of such failures have been observed in buildings (e.g., the 2001 fire in New York City's World Trade Centre 7 [6,7] or the 2017 fire in Tehran's Plasco building [8,9]) and bridges (e.g., the I-65 overpass fire in Birmingham, Alabama, USA [10] and similar cases reported in [11–14]).

The trend towards cost-benefit optimization has led to increasing the use of lightweight and slender sections classified by Eurocode as class-4 [72] in construction projects. Class-4 cross-sections are those in which local buckling will occur before attaining yield stress at any cross-section point because its parts have a minimal thickness compared to the width [64]. Therefore, the analysis is limited to the elastic range (see Fig. 34, which illustrates the ideal plastic behavior achieved for compact class-1 and class-2 sections but not for the non-compact class-3 and slender class-4 sections). These welded or hot-rolled class-4 cross-sections usually are built to safely cope with possible lateral-torsional buckling (LTB) phenomena in beams and flexural buckling in columns at room temperature [73,74]. However, it is also essential to know the performance of these sections when the adverse effects of imperfections and fires are present [4] because they may compromise the stability of the structure and, ultimately, its safety.

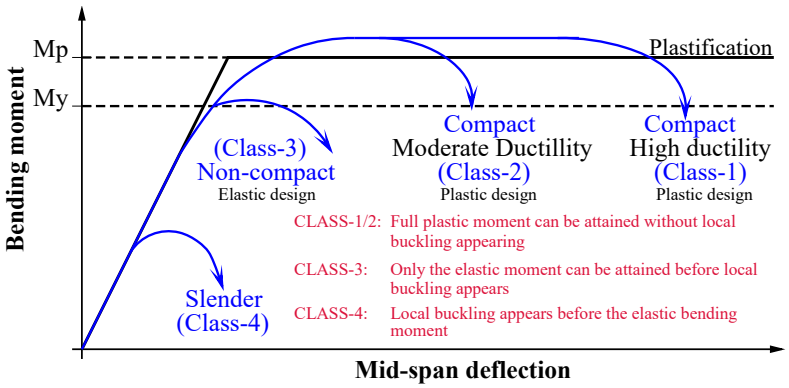

Fig. 34 Moment-deflection relationship for a simply supported steel beam according to cross-section class. Adapted from [75]. M_y is the cross-section elastic bending moment, and M_p is the cross-section plastic moment

The Geometrically and Materially Non-linear Mechanical Analysis with Imperfections (GMNIA, henceforth) is the most advanced and accurate method to solve the LTB problem in steel members [76]. GMNIA can predict the structural member critical loads considering local and global buckling failures (buckling loads), which can appear even before the cross-section plastifies, and define the actual load-bearing capacity of the member [42,77]. The geometrical nonlinearity in the GMNIA is due to large displacements, which are especially important under fire. The material nonlinearity is caused by the creep and the elastoplastic behavior of steel. The imperfections of welded class-4 cross-section steel members come from geometrical and material defects appearing in the plate fabrication process and later in the cut and welding process [78]. Geometrical imperfections can be measured on trajectories along the flange and web plates of the steel member. They can then be drawn to define longitudinal imperfection profiles that approximate the imperfect shape of the flanges and web [23]. These imperfection profiles resemble sinusoidal shapes and provide an approximated idea of the number of undulations in a steel member area. The measured amplitude is the maximum imperfection value of the profile. For modeling purposes, the assumed shape of the initial global and local geometric imperfections can be obtained from combining elastic buckling mode shapes. This method enables the calculation of the amplitude of imperfections in slender steel members [79]. On the other hand, structural (or material) imperfections in steel members with class-4 cross-sections are caused by the high temperatures applied in the welding process that induce a state of residual stresses that remains in the whole section of the unloaded member, even after cooling [78]. Thus, these residual stresses are present before beam loading as an initial condition at room temperature in the modeling.

Several numerical studies have considered that the increase of temperatures in steel members caused by fires relaxes the residual stresses and makes its influence on failure loads small or even neglectable. For example, in a study for predicting the plastic capacity of axially loaded steel beam-columns with thermal gradients, Quiel *et al.* [31] did not consider residual stresses in the computational models because they assumed these stresses relaxed due to increasing steel temperature. In an experimental study of the strength of wide flange columns at elevated temperature, Yang *et al.* [32] concluded that the initial residual stresses affected significantly less the local and global buckling failure modes in fire situations than at room temperature. Heidarpour and Bradford [33] showed similar results in a separate parametric computational study of the effects of residual stresses in heated steel members. The initial LTB numerical models of class-4 tested beams under bending carried out in the "Fire design of steel

members with welded or hot-rolled class-4 cross-section" (FIDESC4 henceforth) research project [23] neglected thermal expansion as well as residual stresses [26]. However, Couto *et al.* [29], in a later study based on the LTB results of FIDESC4, concluded that residual stresses negatively influence the LTB strength under fire of beams with slender cross-sections with LTB strength reductions under fire of a maximum of 15%.

Practically all of the LTB numerical simulations of slender section steel members under fire have used models with shell elements (see, e.g., those of the FIDESC4 report [23] and later works based on the FIDESC4 test results [24–27] as well as other LTB assessment of steel beams included in [28,29]). Nguyen and Park [19] also used shell elements in numerical simulations to evaluate the LTB resistance of steel H-beams exposed to a localized fire considering the combined effects of initial geometric imperfections and residual stresses. Kucukler [20] used shell elements to study LTB in steel beams not susceptible to local buckling, without local imperfections, and under the combined effects of fire and a constant bending moment. Based on the results of an extensive parametric study, Kucukler [20] also proposed an equation for the LTB assessment, which can only be applied to steel beams with class 1 and 2 cross-sections because only global buckling was studied.

Typical shell models naturally capture buckling (local and global) in slender steel section members but at high modeling and CPU time costs, making them difficult to use in parametric and probabilistic studies [38]. Thus, it is necessary to devise simpler beam-type models as reliable as shell-type models to carry out these analysis types at lower costs. This type of model has eventually been used in the bridge deck analysis. For example, Hambly [81] explains the use of grillages and space frames to calculate bridge decks subjected to bending, shear, and torsion. In these methods, the structure is represented by equivalent beam elements. Following this trend, some LTB simulations have been carried out using beam-type finite elements. Quiel *et al.* [31] evaluated the fire response of beam-columns with an I-section subjected to flexural compression under non-uniform temperature gradients with a fiber model of beam elements without including global imperfections and residual stresses, finding a good correlation with the experimental results. These researchers concluded that the added computational cost and complexity of a shell model were unnecessary to predict fire-exposed behavior when the failure mode is entirely plastic. Smyrnaios *et al.* [44] applied an Equivalent Truss Model proposed in [81,82] to determine the LTB resistance of I-section beams at room temperature. The Truss Model idealizes the beam through an equivalent system where two T-sections represent the upper and lower third parts of the beam connected through X-bracing truss elements representing the remaining part of the web. This technique was satisfactorily verified at room temperature with shell models through a parametric study for different geometric imperfection levels. Still, it was not validated with experimental results and was not tested at high temperatures. The Truss Model disadvantage is the impossibility of including the residual stresses in the X-bracing elements, which are naturally present in localized zones of the I-section. Possidente *et al.* [45] developed a 3D-beam finite element for modeling the fire behavior of open cross-section steel elements subjected to torsional effects. Displacement predictions in the LTB behavior of an L-frame carried out with a typical beam discretization model indicated a good agreement with shell-based models if local buckling, residual stresses and imperfections are not present. This work does not contain any validation of the 3D-beam element with experimental results and local buckling was not considered. Franssen *et al.* [46] proposed an effective stress-based method for slender steel members exposed to high temperatures, which was implemented on fiber-type beam finite elements in Safir. This model is a constitutive law of steel that considers the local instabilities in slender steel sections in

numerical models based on Bernoulli finite beam elements. The method was validated against experimental results from three FIDESC4 column tests at high temperatures [23]. The validation of the results was satisfactory, although conservative. Maraveas *et al.* [47] refined the methodology and revised some assumptions [48–50] to improve the original model proposed by Franssen *et al.* [46]. As a result, they developed an equivalent law to be used in the nonlinear numerical analysis of the fire resistance of thin-walled steel members. The constitutive model was implemented in Safir and validated against experimental results of columns subjected at elevated temperatures (FIDESC4 Test-3 [23] and others column tests reported in [83]). Although the simulation results revealed good agreement with the tests, the improved model still gave conservative results for large compressive load eccentricities, so the model is currently still under development.

Within this context, this study proposes two new modeling strategies based on beam-type elements that reduce the high modeling and analysis time costs of shell models typically used to carry out the GMNIA analyses to determine the strength of class-4 steel members. These modeling strategies use 7-DOF second-order Timoshenko beam finite elements (Ansys BEAM189) and include: a) geometrical and material nonlinearity, b) thermal strains, c) Poisson effect on the cross-section owing to mechanical and thermal loading (i.e., the cross-section is scaled as a function of axial stretch), d) imperfections and residual stresses as initial conditions, e) non-uniform temperature, f) preliminary thermal conditioning (perturbed shape and additional thermal stresses), g) self-weight, h) non-linear stabilization of non-linear buckling and post-buckling solution. The first strategy is called the Fiber Beam Model (FBM) and uses a single fiber of I-section BEAM189 elements located at the center of the bottom flange to represent the steel member. The second strategy is called the Cruciform Frame Model (CFM) and idealizes the steel member with a cruciform grid of fibers, where rectangular BEAM189 finite elements make up each fiber. The CFM grid provides flexibility and enables capturing local buckling.

These new numerical strategies are validated using the test results (Test-1 and Test-3) of the FIDESC4 research project reported in [24] conducted with built-up welded steel beams with class-4 cross-sections heated and loaded until LTB failure. To get additional information about the accuracy and advantages of the proposed strategies, a full GMNIA of a shell model of both tests, including the application of residual stresses as zero state, imperfections, and thermal strains, were also carried out in Ansys. The numerical results and computational times of these shell models were compared with those of the FBM and CFM to analyze the performance of the proposed modeling strategies. In addition, FMB and CFM without residual stresses and thermal strains were also carried out to evaluate how the LTB response of the tested beams is affected by not including these two initial conditions.

This chapter is structured as follows: Section 4.2 describes the setup of the FIDESC4 Test-1 and Test-3 used to validate the proposed modeling strategies; Section 4.3 presents the FBM and CFM modeling strategies; Section 4.4 presents the implementation of the GMNIA in the FBM and CFM strategies; Section 4.5 presents the validation of the two strategies with experimental and numerical results of FIDESC4 Test-1 and Test-3. Section 4.5 also includes the numerical results of Test-1 and Test-3 simulations with the modeling strategies without residual stresses and thermal strains and their comparisons with those having them and some further important analyses of the LTB phenomenon in the FBM related to warping, bimoment, and bicurvature.

4.2 Description of the FIDESC4 tests used for validation

The results of two fire experiments on constant cross-section beams (Test-1 and Test-3 of the FIDESC4 experimental and numerical investigation of class-4 beams [23]) were used to validate the proposed modeling strategies. Therefore, this section describes the main features of these fire tests. Both experiments were carried out with slender, simply supported, built-up welded beams with constant cross-section representing structures with a class-4 cross-section (see Fig. 35 and Fig. 36 for a detailed geometrical definition of the tests). The beams spanned 5 m and were heated along the central part where the temperature was intended to be constant and uniform and then loaded until failure due to the local instability of the plates.

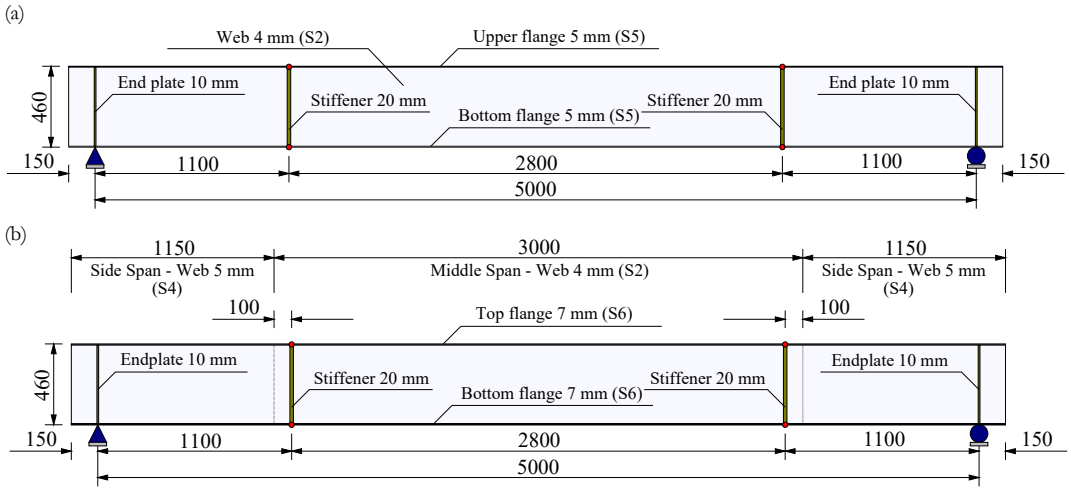

Fig. 35 Dimensions and materials of tested beams. (a) Test-1. (b) Test-3 [23]

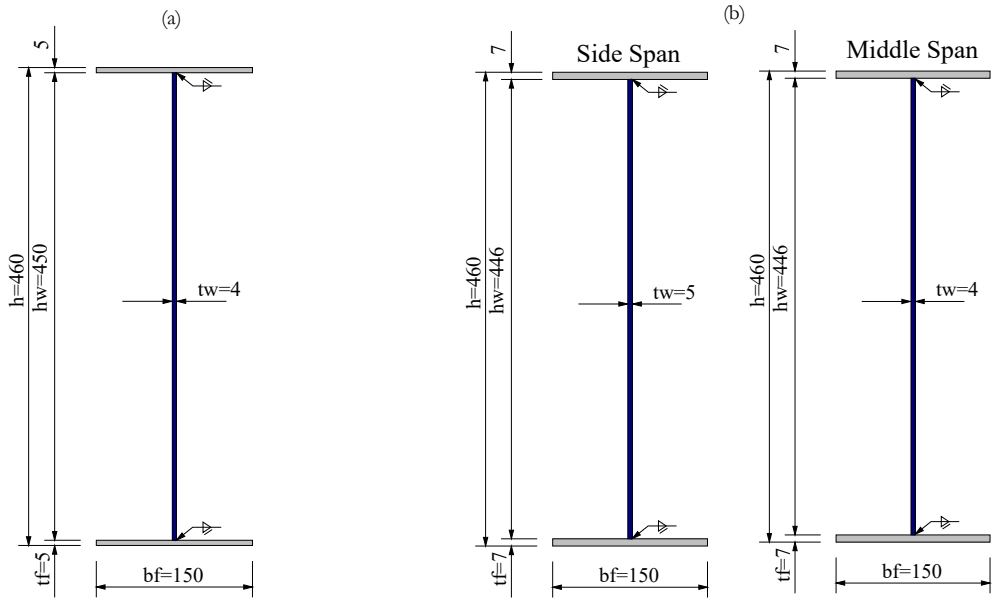

Fig. 36 Dimensions of welded I-sections, in mm. (a) Test-1. (b) Test-3 [23]

The loading consisted of two equal concentrated loads applied symmetrically so that the bending moment in the central heated part was constant. Fig. 37 illustrates the test setup, including the ceramic pads used to heat the beam and the devices used to load it. Fig. 38 exemplifies the tested beam subjected to pure bending in the central heated zone.

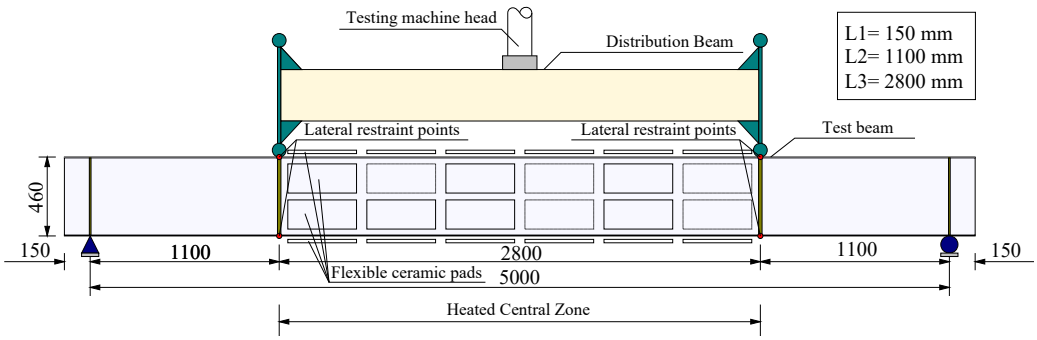

Fig. 37 Scheme of the experiment (based on [23])

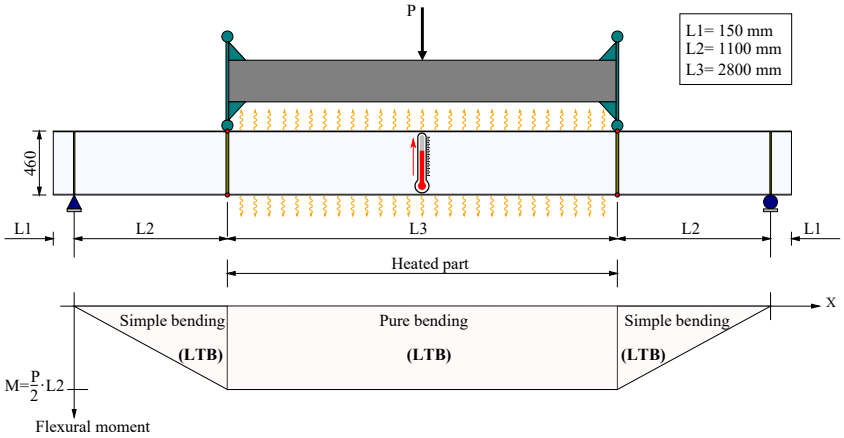

Fig. 38 Tested beam subjected to pure bending (based on [23])

Before the tests, the steel properties of the beam plates were obtained at room temperature (see Table 4). According to EN 1993-1-2 [64], the slenderness of the web plate was $\bar{\lambda}_p$=1.33 for Test-1 and $\bar{\lambda}_p$=1.13 at the middle span for Test-3 [23]. After placing the beams on the supports, laser scanning and manual measurements established the initial geometry with imperfections. For the measurement of the global imperfection amplitude, the deviation between the stiffeners was measured. In the central zone of the tested beams, local imperfections were measured on the web and the top flange. Local imperfections on the web were measured in points placed in the compression part. On the top flange, they were measured over the edges where the cut-off imperfections of the plates are expected to be higher. Then local imperfection profiles were drawn. The maximum absolute value of these local imperfection profiles was assumed as the local imperfection amplitude. Table 5 lists the amplitude of local and global imperfections for each test [23].

Table 4. Steel properties at room temperature [23]

Test / Part of beam	Steel samples	Average Yield Stress (MPa)	Elastic Modulus (MPa)
Test-1/ Web Test-3/ Web middle span	S2	392.8	176897
Test-1/ Flanges	S5	381.5	209988
Test-3/ Web side span	S4	368.5	199200
Test-3/ Flanges	S6	421.5	208900
Stiffeners	---	355.0	210000

Table 5. Amplitudes of local and global imperfections, in mm [23]

Imperfection	Test-1	Test-3
Local (Top flange)	2.27	0.69
Local (Web)	7.36	5.80
Global	2.50	1.50

Fig. 39a shows the setup of the experiments. Point pinned supports were located at the end extremities of the beam, as shown in Fig. 39b and Fig. 39c. All rotations and transverse deflections between these point supports were allowed, except at the stiffener points where the lateral deflection was restrained. Displacements in all directions were restrained in the left support, while only the axial displacement was released in the right support. In addition, both supports allow free torsion of the end cross-section. The beam was heated with Manning heat power units and flexible ceramic pads (see Fig. 37). Temperatures were measured from the beginning of the heating to the end of the tests. For this purpose, thermocouples along the beam according to the position of the ceramic pads were distributed. Both tests were set to be at 450 ºC. However, the measured temperatures slightly varied during the tests and were non uniform for the whole section. The average measured temperatures at each part of the beam (top flange, web, bottom flange) used for numerical modeling are shown in Fig. 40a. The load was applied through a hydraulic jack and introduced by a distributing beam at the edges of the heated central part, as shown in Fig. 37 and Fig. 39d. The two vertical load application points were laterally restrained by frames contacting the beam through gadgets, as shown in Fig. 39e. Four potentiometers were used to measure the displacements in the load application points and calculate the deflections in the bottom flange center and the lateral rotation of the beam at mid-span. The tests were deflection controlled with a vertical deflection rate of 3.5 mm per minute (see Fig. 40b). The final vertical deflection measured at mid-span at the end of the experiments was 50 mm [23].

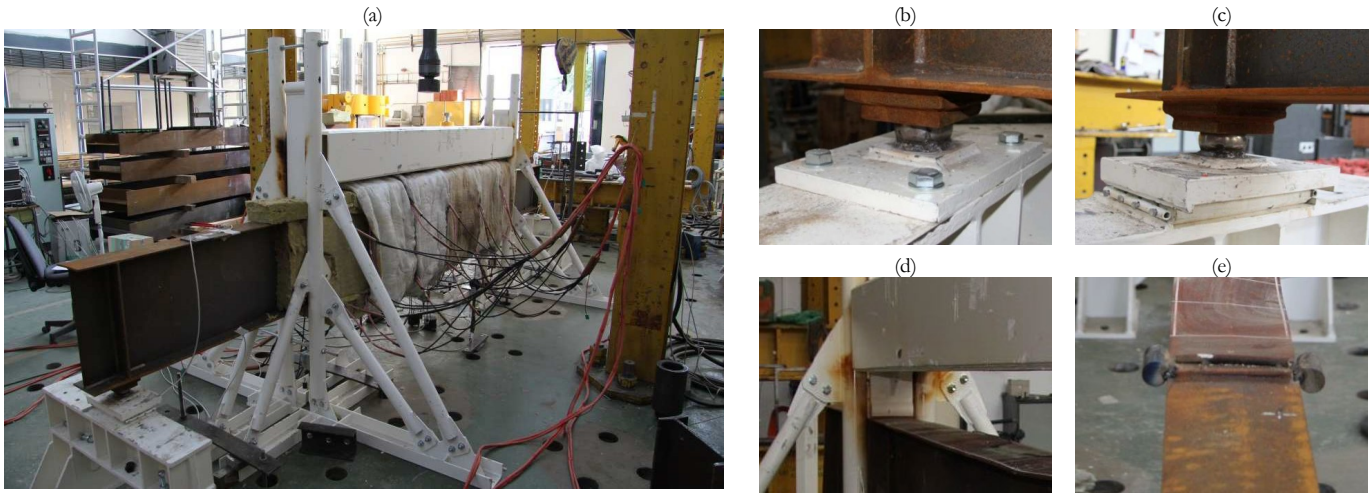

Fig. 39 (a) Test setup. (b,c) Pinned supports. (d) Application of load through a distribution beam. (e) Gadget on beam for lateral restraint [23]

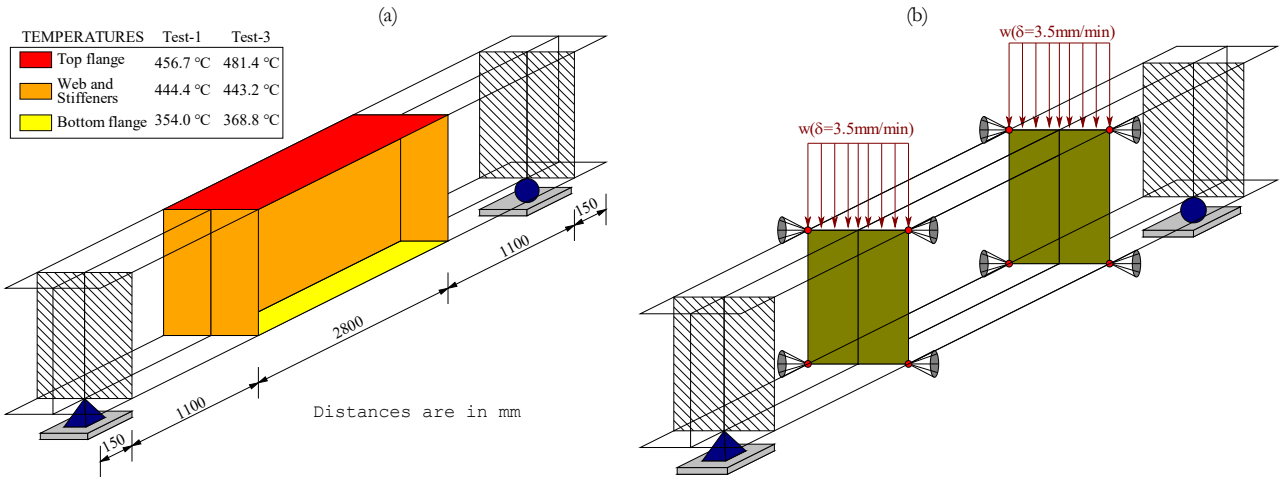

Fig. 40 (a) Average steel temperatures in the heated zone of the beam. (b) Test boundary conditions and loads

4.3 Proposed modeling strategies

FIDESC4 investigation [23] used shell elements instead of beam elements in the numerical models because local buckling was one of the dominant failure modes, and it depends on localized residual stresses and imperfections that are difficult to include in beam elements. However, this paper proposes two new modeling strategies to analyze class-4 beams subjected to LTB under elevated temperatures using Ansys 3D beam finite elements. These modeling strategies are denoted by FBM (Fiber Beam Model) and CFM (Cruciform Frame Model). Both modeling strategies are made up of appropriate Timoshenko BEAM189 finite elements available in Ansys.

In the FBM, the tested beam is discretized as a fiber (see Fig. 41a) of I-section BEAM189 elements. In the CFM, the beam is represented as a cruciform arrangement of fibers (see Fig. 41b) to make the model more flexible with a greater number of degrees of freedom and thus

be able to emulate the behavior of a model with shell elements at a lower computational cost, taking advantage of the extrusion of the BEAM189 element. CFM can also be understood as a grid of rectangular BEAM189 elements capable of reproducing the local buckling failure. In FBM, non-linear LINK180 compression truss elements are additionally included, just where the stiffeners are located, to reproduce the three-dimensionality of the test and the boundary conditions. In CFM, endplates and stiffeners are vertical fibers of rectangular BEAM189 elements, and boundary conditions can be easily applied to the model nodes.

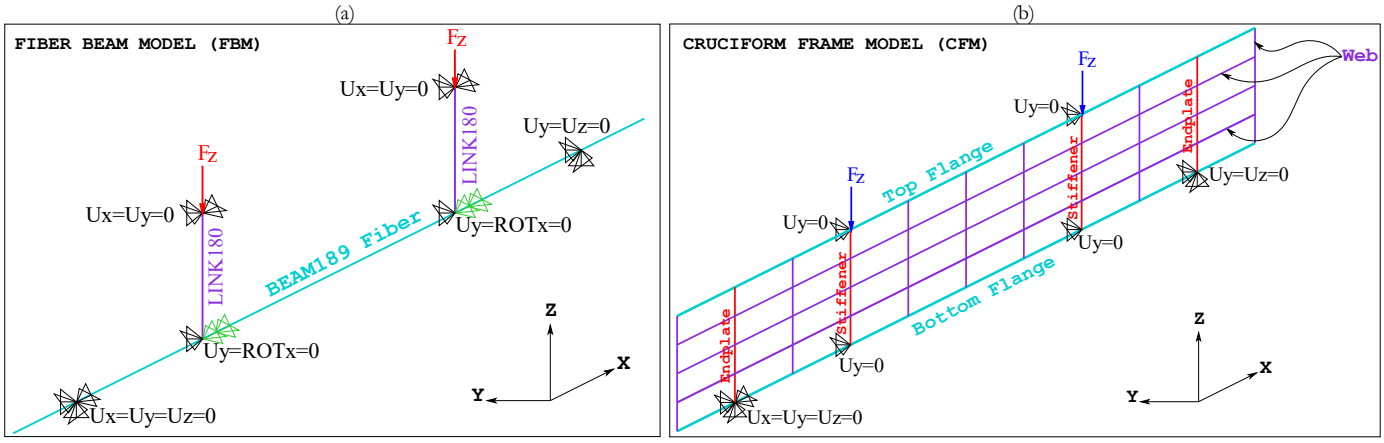

Fig. 41 Idealization of the tested beam in each proposed modeling strategy. (a) FBM. (b) CFM

4.4 LTB-GMNIA of the tested beams

The LTB problem of the beam with class-4 cross-section in fire is solved through a GMNIA in Ansys, including a linear buckling analysis and the imperfection amplitudes measured to introduce the initial imperfections. GMNIA also involves non-linear buckling and post-buckling analyses. Non-linear buckling analysis is a static analysis with large deflections active, extended to a point where the beam attains its limit load or maximum load, including the material nonlinearity. Meanwhile, the post-buckling analysis is a continuation of the non-linear buckling analysis after the load attains its buckling value. A special non-linear stabilization technique is applied to overcome the local and global buckling instability problems due to the post-buckling stage is unstable [53]. Numerical instability matches the instability of the structure. When instability appears in the structure, large changes in displacements occur with only small load perturbations. Ansys program uses an internal non-linear stabilization technique to solve the numerical instability by applying artificial dampers to the nodes with unstable degrees of freedom. A damping force is calculated proportionally to the pseudo velocity at these nodes, which is determined as the displacement increment divided by the pseudo time increment of the sub-step. For nodes with practically stable degrees of freedom, the influence of damping is negligible since the displacements and stabilization forces are relatively small compared to the physical forces. Although the stabilization forces (or damping factors) have the same unit and definition as the classical damping forces, the concept, in essence, is numerical and artificial for the calculation of non-linear stabilization [84]. The GMNIA steps applied in the FBM and CFM strategies are outlined below, followed by an explanation of each step.

1. Finite element model definition. Creation of the model and boundary conditions.
2. Eigenvalue analysis (linear elastic buckling analysis).
3. Implementation of initial imperfections.
4. Implementation of internal residual stresses.
5. Application of the first load phase called thermal conditioning, henceforth. This phase includes the progressive heating of the model up to the target temperature level and the activation of self-weight stresses. Additional thermal stresses and strains are generated in this phase.
6. Application of the second load phase called post-conditioning, henceforth. This phase includes the application of loading by increments maintaining the loads from the previous stage.
7. Results of displacements, applied load, ultimate load, and the ultimate moment of the section.

4.4.1Finite element model definition

A fiber model (FBM) and a cruciform model (CFM) are created to simulate the LTB of FIDESC4 Test-1 and Test-3 following the idealizations shown in Fig. 41a and Fig. 41b. In the FBM, lateral restraint in the global *y-y* direction and torsional restraints to ensure stability are applied to the two nodes on the fiber axis, matching the location of stiffeners. Lateral restraint in the *y-y* direction and an axial restraint in the *x-x* direction are imposed on the LINK180 end nodes where the stiffeners are located, as shown in Fig. 41a. In CFM, *y*-displacements are null in the four nodes where the imposed lateral restraint is, as shown in Fig. 41b. In both FBM and CFM modeling strategies, displacements in all global axes are restrained in the first point pinned support, and displacements in global *y-y* and *z-z* axes are restrained in the second one. The stress-strain ratio (σ-ε) of steel at high temperatures and the reduction factors $k_{y,\theta}$, $k_{p,\theta}$ and $k_{E,\theta}$ given by EN 1993-1-2 [64] were used in the models. The values of yield strength and elastic modulus of materials for flanges, web, and stiffeners at room temperature used for modeling were given in Table 4. A constant Poisson ratio (ν=0.3) was also assumed. The creep effect on the deformation of steel was considered implicit in the material model. The Ansys multi-lineal isotropic hardening with temperature dependence model was used to adequately represent the stress-strain relationships depending on temperature [66]. Variation of thermal expansion (α) of steel with temperature was also determined based on EN 1993-1-2 [64]. The geometric nonlinearity was activated to introduce the formulations of large deformations and deflections. All numerical model data were taken from the FIDESC4 investigation report [23], and some validation details were taken from Prachar *et al.* [24,80].

4.4.2 Eigenvalue analysis

An eigenvalue analysis was carried out to establish the initial imperfections in the numerical models of the tested beams. The buckled mode shapes (global and local) resulting from eigenvalue analysis approximately represent the global and local imperfection shapes measured before the test. The eigenvalue buckling analysis process includes two steps: a linear static

solution and an eigenvalue buckling solution. The first step involves a linear analysis with unit loads (Fz=1 kN in Fig. 41). In the second step, the eigenvalues are calculated, and the elastic buckling analysis is expanded to find the buckling mode shapes associated with each calculated eigenvalue. Two buckling mode shapes are selected adequately after that, i.e., one consistent with the measured global imperfection shape and the other congruent with the local imperfection profile on the web measured in the central part of the beam. According to [23], a simple lateral curvature in the *y-y* direction characterizes the global buckling mode shape, and the local buckling mode shape resembles well-defined undulations in the *y-y* direction in the central part of the beam. E.g., six undulations (three peaks and three valleys) on the web for Test-1 and eight undulations for Test-3 [23]. The nodal solution for the global and local buckling modes can be expanded to the pseudo-mesh nodes of the BEAM189 element cross-section in the post-processing stage. In the expansion, vertical undulations also appear in the top flange, which can be evidenced in the extruded view. These web and top flange undulations represent the shape of the initial geometric imperfections measured on the tested beams used in the LTB simulations. The amplitude or absolute maximum value of the imperfections is extracted from the two selected buckling mode shapes in order to scale them to the size of the measured amplitudes. In the proposed strategies, the global amplitude is the maximum lateral deflection, in the *y-y* direction, of the selected global mode shape. This global amplitude is extracted from the entire model. The local amplitude on the web is the maximum lateral deflection, in the *y-y* direction, of the selected local mode shape. The local amplitude in the top flange is the maximum vertical deflection, in the z-z direction, of the selected local mode shape. The local amplitudes are extracted from the heated zone (central part) of the beam model because this was the location where the imperfections were measured.

4.4.3 Implementation of initial imperfections

In order to simulate the initial shape with imperfections, the geometry of the finite element model is updated according to the displacement results of the global and local buckling mode shapes (obtained from the previous eigenvalue analysis) so that a modified geometry based on the deformed configuration of the previous analysis is created. In other words, the displacement results of the global and local buckling mode shapes on the original geometry are added. Before being added together, these displacements are multiplied by a factor that scales and weights them. This factor is responsible for adding a percentage of the displacements to the geometry of the finite element model (e.g., factor 1.0 adds the full value of the displacements to the geometry of the finite element model). This factor results from multiplying two other factors, i.e., one for scaling and one for weighting. The scale factor is a multiplier that adjusts the displacements of each buckling mode shape to the size of the measured imperfection amplitude. The scaling factor is determined as the ratio of the measured imperfection amplitude (given in Table 5) to the simulated amplitude. Therefore, three scaling factors are defined, one to scale the *y-y* displacements of the global mode shape, and two for scaling the *y-y* and z-z displacements of the local mode shape. These simulated amplitudes are extracted after the local and global buckling mode shapes are carefully chosen. The simulated global amplitude in the *y-y* axis is extracted from the entire model, while the simulated local amplitudes (on the web about the *y-y* axis and the top flange about the z-z axis) are drawn from the central part of the beam. GSF is the global scale factor, and LSF1 and LSF2 are the local scaling factors on the web and top flange, respectively. They are calculated by Eq. (2-4).

$$GSF = \frac{\text{Measured global imperfection amplitude}}{\text{Simulated global amplitude } (y\text{-}y \text{ axis})} \quad (2)$$

$$LSF1 = \frac{\text{Measured web local imperfection amplitude}}{\text{Simulated local amplitude } (y\text{-}y \text{ axis})} \quad (3)$$

$$LSF2 = \frac{\text{Measured top flange local imperfection amplitude}}{\text{Simulated local amplitude} (z\text{-}z \text{ axis})} \quad (4)$$

The participation factor is responsible for weighting the displacements of each buckling mode shape (global and local). It defines the portion of the displacements of each two buckling mode shapes contributing to the initial imperfect geometry. GPF denotes the participation factor of the global mode shape displacements and, LPF1 and LPF2 are the participation factors of the web and top flange displacements of the local mode shape, respectively. In the proposed numerical modeling strategies, each participation factor is assumed to be 1/3 due to the number of imperfection amplitudes measured, as shown in Eq. (5).

$$GPF = LPF1 = LPF2 = 1/3 \quad (5)$$

In this way, the imperfections added to the original geometry are the scaled and weighted displacements of the global and local buckling mode shapes. The nodal x, y, z-displacement results of global and local mode shapes are stored in arrays denoted as GMS and LMS, respectively. Therefore, GMS contains the nodal displacements of the global mode shape, and LMS contains those of the local mode shape in the central zone of the beam. Thus, the imperfections added by the global mode shape (called GI) and those added by the local mode shape (called LI) result from scaling and weighting the GMS and LMS arrays with the scaling and participation factors, as shown in Eq. (6) and Eq. (7). Therefore, GI and LI can be understood as arrays of nodal imperfections (equivalent to the scaled and weighted nodal displacements). GI stores the imperfections of each node of the finite element model, while LI stores the node imperfections in the central zone of the beam model.

$$GI = \underbrace{GMS(GSF \times GPF)}_{\text{Whole Beam}} \quad (6)$$

$$LI = \underbrace{LMS\left(\underbrace{LSF1 \times LPF1}_{\text{Web}} + \underbrace{LSF2 \times LPF2}_{\text{Top flange}}\right)}_{\text{Central zone}} \quad (7)$$

However, in the FBM and CFM modeling strategies, the scaling factor over the local imperfection of the top flange (LSF2) cannot be considered in Eq. (7). That is because the simulated local imperfection amplitude in the z-z direction is on the fiber axis and not in the cross-section of the elements, so this amplitude cannot properly represent the maximum simulated imperfection at the top flange edges where the local imperfections were measured.

Nevertheless, it was considered that the imperfections on the top flange could be approximately included through the local cumulative participation factor (LCPF) of 2/3, as shown in Eq. (8), which compensates for the non-inclusion of the local top flange imperfection. In other words, the local mode shape contribution was increased by 1/3. Therefore, the local imperfection array (LI) results from scaling the nodal displacements (in the x, y, z-directions) of the local mode shape with the scaling factor LSF1 and weighting them with the local cumulative participation factor LCPF, as shown in Eq. (9).

$$LCPF = LPF1 + LPF2 = 2/3 \tag{8}$$

$$LI = \underbrace{LMS\ (LSF1 \times LCPF)}_{\text{Web (Central zone)}} \tag{9}$$

To approximate the imperfect initial geometry (IIG) of the model, first, the global imperfections (GI) are added to the node coordinates of the finite element model. Then, from this revised geometry, local imperfections (LI, in Eq. 9) are added to the node coordinates of the central zone of the beam model, as illustrated in Eq. (10). The node coordinate array of the model is denoted in Eq. (10) as FGC (Full Geometry Coordinates), and that of the beam central zone is denoted as CGC (Central Geometry Coordinates). The largest displacements of the global and local buckling mode shapes are in the y-y direction, and displacements in the two other directions are too small (10E-13) so that the small displacements after scaling and weighting remain so. Therefore, x-x and z-z imperfections added to x, z-coordinates are too minor, so this methodology to create imperfections is correct.

$$IIG = \underbrace{[FGC+GI]}_{\text{Whole beam}} + \underbrace{[CGC+LI]}_{\text{Central zone}} \tag{10}$$

The web resulting shape in the central zone of the beam is a combination of the global and local imperfections. Out of the central part of the beam, only global imperfections are present. After that, the resulting imperfect shape is expanded to the cross-section pseudo-mesh nodes of the BEAM189 elements in the post-processing. As a result of the expansion, undulations appear out of the beam axis on the top flange edges. The resulting undulations on the web and the top flange after expansion depict the initial imperfections of the model.

4.4.4 Implementation of residual stresses

According to how the test was carried out, initial axial residual stresses are incorporated into the proposed numerical models of the tested beams before applying thermal and mechanical loadings. Residual stresses at room temperature are relevant because they act as an initial stress condition (σ_{x0}). In the finite element formulation of the problem, initial stresses and initial strains (ε^0) represent elementary equivalent nodal forces in the equilibrium equations. Therefore, they are part of the total equivalent nodal forces integrated by other force components such as body and surface forces and forces produced by initial strains coming from the thermal action [85]. In summary, the residual stresses are part of the global

equilibrium of the finite element mesh and the stress field of the structure, so they must be considered.

BEAM189 finite elements allow the application of these axial residual stresses in the cross-section pseudo-mesh cells. The cells are set so that the tensile and compressive residual stresses in the web and flanges can be applied as closely as possible over the cross-section regions where they are localized. Fig. 42 presents the residual stress pattern at room temperature for the welded I-section considered by FIDESC4 [23] based on [86] used in this study. In Fig. 42, the residual stresses act in the whole cross-section. The yield stress values f_y are at room temperature, and red areas (T) represent tensile stress while blue areas (C) represent compressive stress.

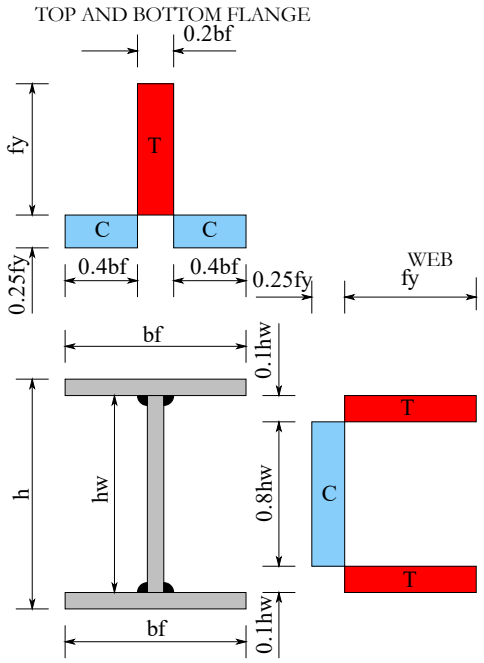

Fig. 42 Residual stress pattern for welded I-section at room temperature. Above: for both top and bottom flanges. Right: Web [23,86]

4.4.5 Application of the thermal conditioning

In the experiments, progressive heating of the central zone of the beam is performed from 20 °C until the target temperature level at each part (top flange, web, and bottom flange) is attained before applying the mechanical load (thermal conditioning). This change in the temperature results in thermal strains (ε_x^θ) [87]. The non-uniform temperature in the cross-section causes initial bending resulting in thermal stresses (σ_x^θ) that combine with initial residual stresses (σ_{x0}) and self-weight stresses (σ_x) modifying the initial stress state. Moreover, the Poisson effect induces transverse thermal strains (ε_y^θ, ε_z^θ) in the central zone of the beam that intensifies the initial geometric imperfections; in consequence, a revised imperfect geometry is generated. Furthermore, the temperature degrades the material and changes the stiffness in the central zone. As the side spans are unheated, their stiffness is higher than the stiffness of the central zone, acting as semi-rigid boundaries over the middle span (see Fig. 43), causing some

y-rotation restraints in these frontiers. Additionally, lateral stresses (σ_y^0) are induced on the stiffener ends (red points in Fig. 43) due to the lateral restriction imposed by the frameworks. As a result, axial and vertical strains (ε_x^0, ε_z^0) are generated by the Poisson effect. In summary, the thermal conditioning modifies the initial state of the tested beams, among others, for the following reasons: 1) the appearance of a thermal stress-strain state caused by the temperature rise from 20°C to the target temperature in each part of the beam and bending due to non-uniform temperature distribution in the cross-section; 2) the Poisson effect; 3) the appearance of additional imperfections; 4) the formation of semi-rigid boundaries. It should be noted that the geometric imperfections are the result of thermal strains. The initial geometric imperfections come from the thermal strains produced in the manufacturing and cutting process of the plates. In the thermal conditioning stage of the tested beams, the additional geometric imperfections come from the thermal strains produced by the temperature increase and the temperature differential of the cross-section. Finally, thermal strains must be activated in the simulation of the tested beams to account for all the effects of high temperatures in the thermal conditioning stage.

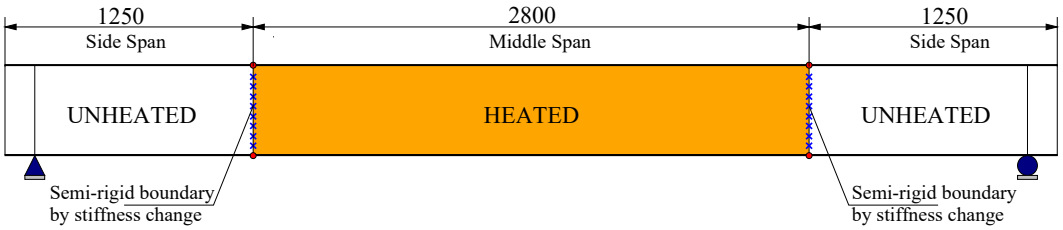

Fig. 43 Semi-rigid boundaries produced by stiffness change

According to how the test was carried out, the thermal condition is included in the numerical models of the tested beams before applying mechanical loadings. To do so, ramped temperature for a time t=1E-08 min is applied starting from the room temperature (20 °C) up to the target temperature at each part (top flange, bottom flange, and the web) shown in Fig. 7a in which non-heated zones are assumed to have a room temperature of 20 °C. The time is arbitrarily chosen as a very small value close to zero because the analysis is static; therefore, the mechanical response in this stage is not dependent on time. Once the residual stresses, temperature from thermal conditioning, and self-weight loads are applied, a first GMNIA is done here. Results of deformed shape (perturbed shape) and all analysis results are the starting point for the second GMNIA carried out in the next phase, including the controlled displacement mechanical loading.

4.4.6 Application of post-conditioning

According to how the test was performed, this second loading phase starts from the deformed shape and the stress-strain results of the previous analysis. In this second phase, the self-weight and the temperatures in each part of the beam (flanges, web, and stiffeners) remain applied. Additionally, the vertical load is applied to the upper nodes of the stiffeners through the displacement-controlled method at a rate of 3.5 mm/min during 6.5 min. Therefore, Fz (see Fig. 41) is applied as a vertical displacement (Uz) until a target value of 22.75 mm. This target displacement value is enough to evidence the load behavior, including the ultimate load

and the load-bearing capacity decrease of Test-1 and Test-3. In the FIDESC4 simulations [23], the load capacity was registered up to 25 mm of mid-span vertical deflection for Test-1 and 30 mm for Test-3. Once loads in this phase are applied, the full GMNIA-LTB is done.

4.4.7 Results

At the end of the GMNIA, time history results of the top flange vertical mid-span displacements, the applied load, ultimate load, and ultimate bending moment are obtained. The full GMNIA procedure implemented in the proposed numerical modeling strategies (FBM and CFM) is illustrated in Fig. 44.

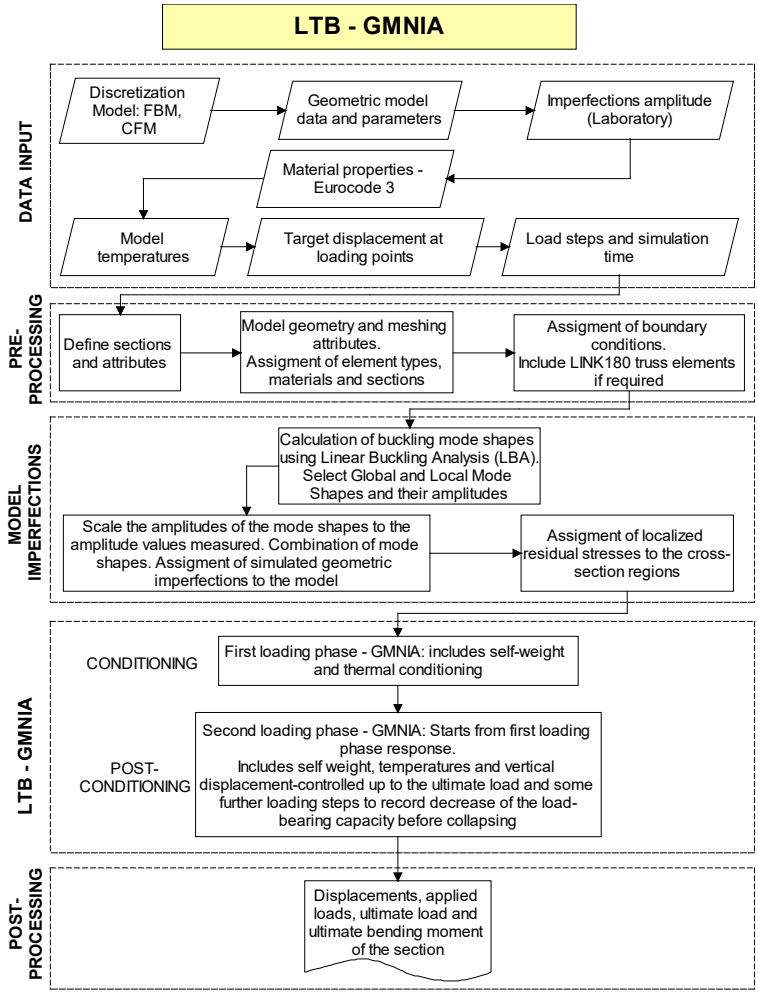

Fig. 44 Full LTB-GMNIA for the FIDESC4 tested beams

4.5 Implementation of LTB-GMNIA in the proposed modeling strategies

Hereafter the implementation of the LTB-GMNIA in the proposed FBM and CFM modeling strategies is explained in detail for Test-1. The reason is that the methodology of each strategy is the same for the tested FIDESC4 beams with constant cross-section.

4.5.1 Fiber Beam Model (FBM)

The tested beam subjected to LTB is idealized as a single fiber of 342 BEAM189 finite elements with endplates and stiffeners included. In this model, each finite element has a cross-section and a material depending on the part of the beam it represents, e.g., web, flange, endplate, or stiffener. The beam is made of three distinct types of cross-sections (welded I-section, endplate, and stiffener) and three different types of materials (one for endplates and stiffeners, and two materials for flanges and web -S2 and S5, respectively as shown in Fig. 35a and Table 4-). Therefore, three different sections and three different materials are defined in the model. Cross-sections are assigned to finite elements, while materials are assigned to the pseudo-mesh cells of the cross-section. This way to assign materials by cells enables differentiating zones with different materials in the steel member, i.e., flanges and web materials, and endplate and stiffener materials. The number of cells in the cross-section is set to apply the residual stress pattern shown in Fig. 42. For this purpose, 75 cells were defined at each flange and 50 cells at the web, as shown in Fig. 45.

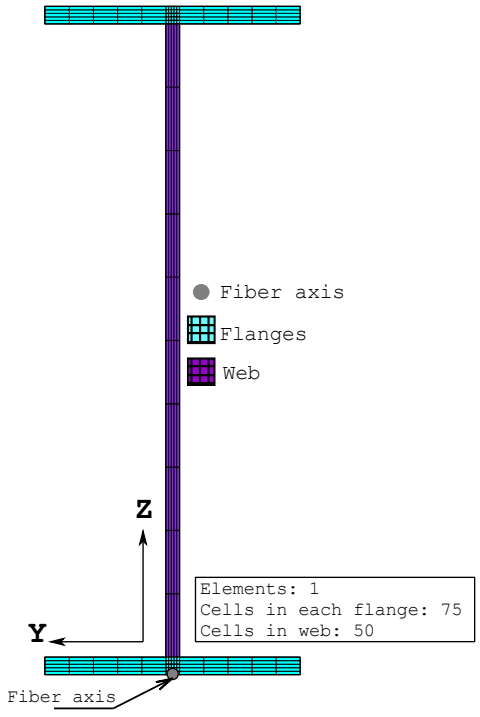

Fig. 45 I-cross-section discretization and cells for Test-1

The fiber axis is moved to the outer edge of the bottom flange, where the boundary conditions are applied, which means boundary conditions are eccentric. LINK180 truss elements between the two flanges transfer the load from the application points on the outer surface of the top flange to the outer surface of the bottom flange, where the fiber axis is located. Thus, LINK180 elements have the cross-section area of the stiffeners given in Fig. 35a. The meshing and boundary conditions in the fiber are shown in Fig. 46a, and the tested beam extruded in which all its components are visible is shown in Fig. 46b.

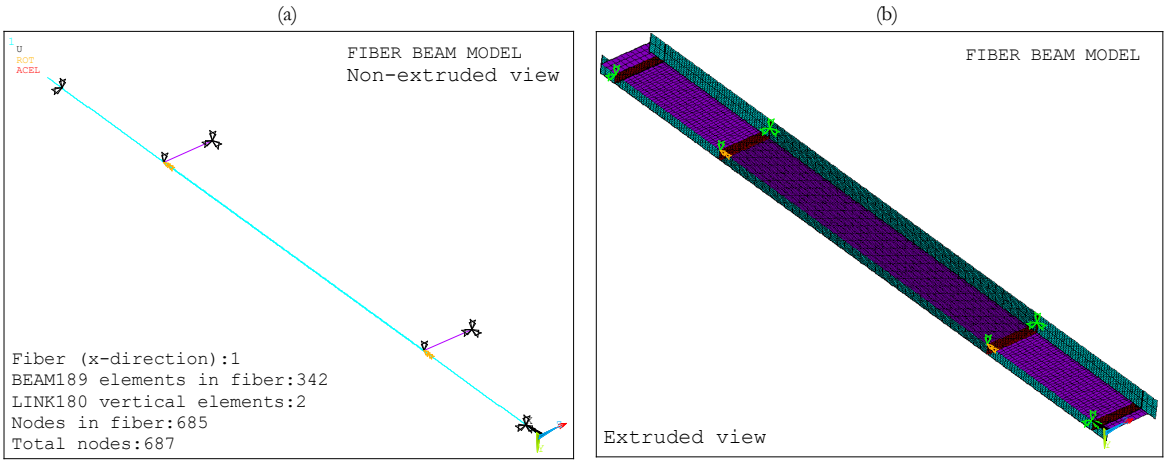

Fig. 46 FBM meshing and boundary conditions for Test-1.
(a) Non-extruded view. (b) Extruded view

Fig. 47 and Fig. 48 show the global and local buckling mode shapes chosen from the eigenvalue analysis. In the extruded view of Fig. 47b, a simple lateral curvature in the *y-y* direction is clearly observed. In the local mode shape of Fig. 48b, the slight lateral undulations in the central part of the beam depict the local imperfections on the web. Although this is a single fiber model, the extruded local shape in Fig. 48b also shows undulations on the top flange, allowing for the simulation of the measured local imperfections. Undulations out of the central part of the beam in Fig. 48b are not considered because local imperfections are only applied to the central zone of the beam where they were measured. In the FBM, it is assumed that the displacements in the *y-y* direction are from the web. Therefore, the simulated amplitude in the *y-y* direction is the maximum lateral deflection obtained from the fiber nodes for the global buckling mode shape (in Fig. 47a) and from the nodes in the central part of the fiber for the local buckling mode shape (in Fig. 48a).

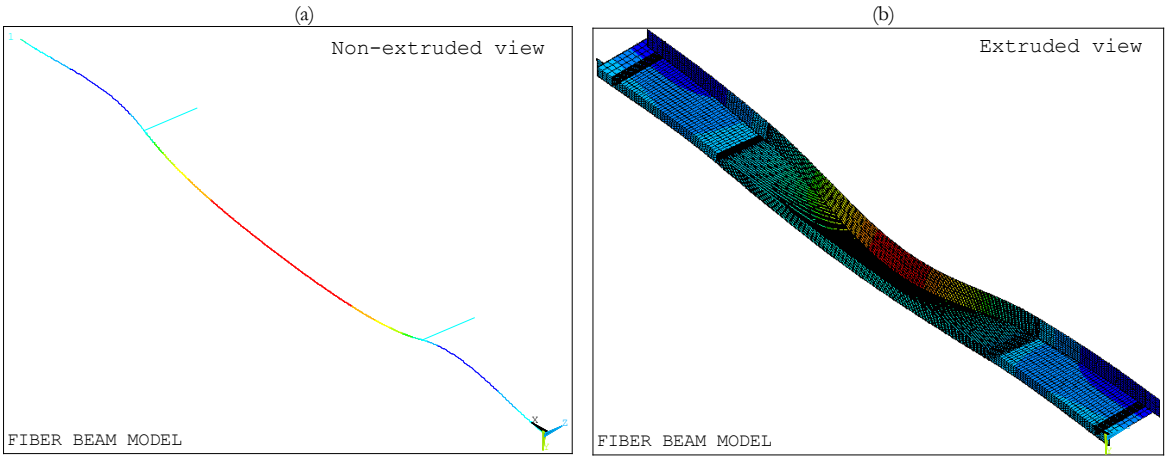

Fig. 47 FBM global mode shape for Test-1. (a) Non-extruded view. (b) Extruded view

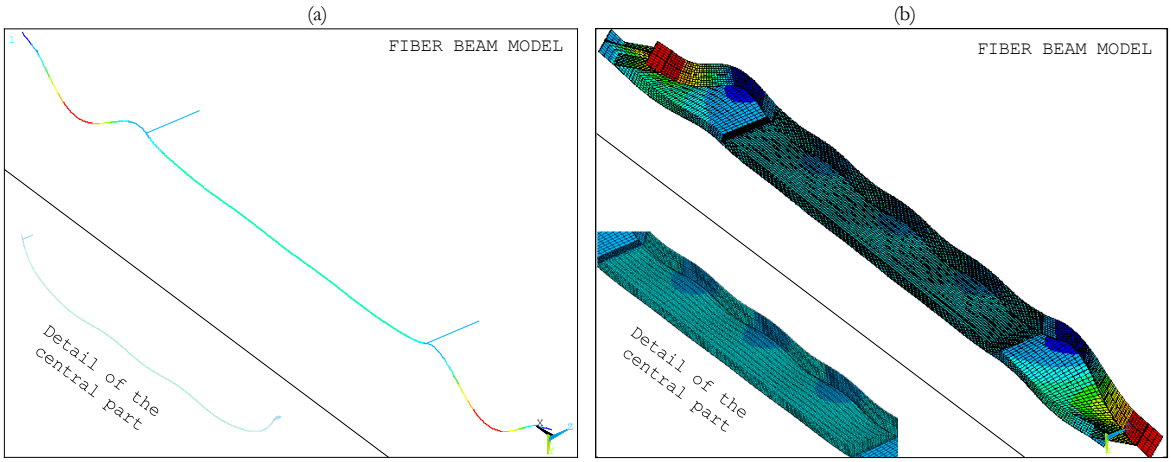

Fig. 48 FBM local mode shape for Test-1. (a) Non-extruded view. (b) Extruded view

The imperfect initial geometry is obtained by adding the imperfections to the node coordinates of the original model, according to Eq. (10). In both global and local mode shapes, x-displacements and z-displacements are almost zero on the fiber axis, so that x-imperfections and z-imperfections adding to x-coordinates and z-coordinates of the FBM are also almost null. Consequently, the x-coordinates and z-coordinates of the FBM are practically identical in the original and imperfect geometry. As y-coordinates, in this case, are zero, the imperfections in the y-y direction are equal to the y-coordinates of the FBM imperfect initial geometry. Since, in the FBM, the beam is modeled as a single BEAM189 finite elements fiber, it is assumed that the displacements in the y-y direction are from the web. Therefore, the y-y amplitude of the global and local mode shapes is used for calculating the global and local scale factor, GSF and LSF1, as shown in Eq. (2) and Eq. (3). Also, the global and local displacements occurring in the lateral direction are used to calculate the global and local y-imperfections, according to Eq. (6) and Eq. (9). The FBM y-y imperfections are plotted in Fig. 49.

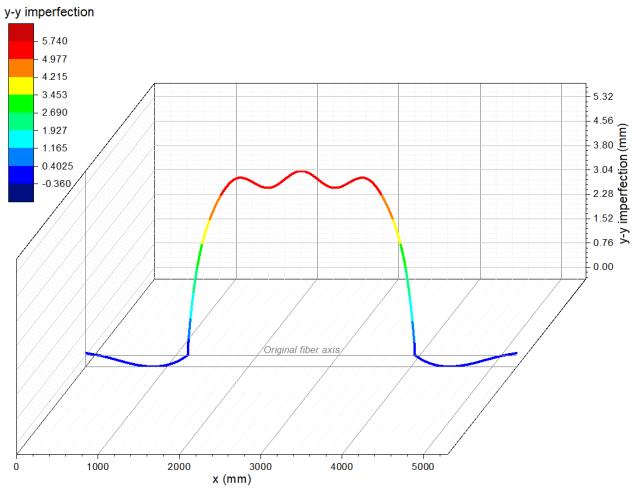

Fig. 49 Imperfect initial geometry of FBM for Test-1 (mm)

Imperfections in Fig. 49 are obtained from combining the scaled and weighted lateral displacements of both buckling mode shapes and are located in the central zone of the beam, as expected. The null imperfections in Fig. 49 match the points of the stiffeners and endplates where the *y*-displacement boundary condition is restrained in the model. Out of the central zone of the beam, very small imperfections are coming from global *y*-displacements.

According to Fig. 42, compressive (blue) and tensile (red) axial residual stresses at room temperature in the web and flanges are applied to the cross-section pseudo-mesh cells of the BEAM189 element, as shown in Fig. 50.

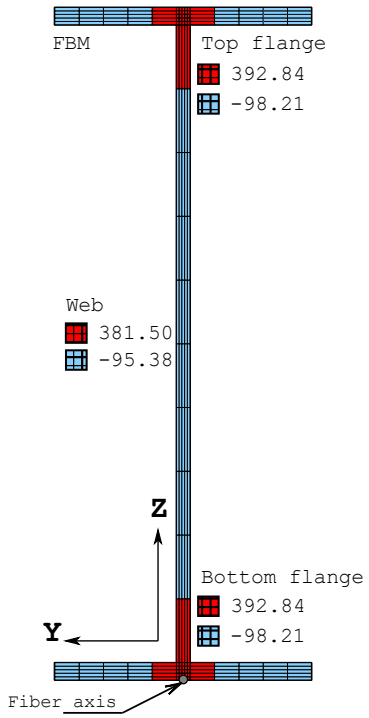

Fig. 50 FBM tensile and compressive residual stresses in the welded I-section for Test-1 [MPa]

BEAM189 finite elements making up the fiber do not have temperature degrees of freedom. However, they support uniform temperature loading and linearly varying thermal gradients within the cross-section [53]. These two components allow representing the non-uniform transverse temperature distribution in the element. For this reason, in the thermal conditioning stage of the LTB-GMNIA (see Fig. 44), the target temperature is established by a uniform temperature and a vertical gradient (in z-z axis) [43] to be attained in the BEAM189 elements in the central part of the beam following the procedure described in the thermal conditioning phase. Additionally, a target uniform temperature equal to that of the web in the test (444.4 °C) is specified in the BEAM189 elements symbolizing the stiffeners and LINK180 elements representing the load axes.

The two components approximating the non-uniform temperature in the cross-section are calculated by linear regression from the temperatures measured in the web and flanges (shown in Fig. 40a), as illustrated in Fig. 51.

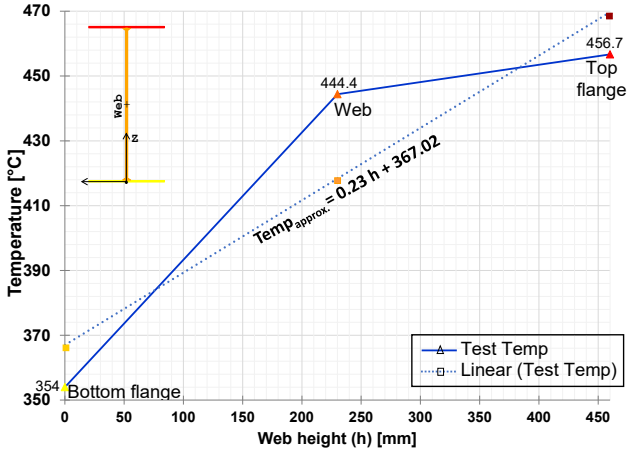

Fig. 51 Approximation of non-uniform temperature in the BEAM189 cross-section (Test-1)

In this sense, the non-uniform temperature in the cross-section (Fig. 52a) is approximated by two components [43]:

- A uniform temperature component (Fig. 52b) equal to the linear regression intercept (367.02°C in Fig. 51).
- A component of thermal gradient varying linearly on the z-z axis (Fig. 52c) equal to the slope of the regression line (0.23°C/mm in Fig. 51).

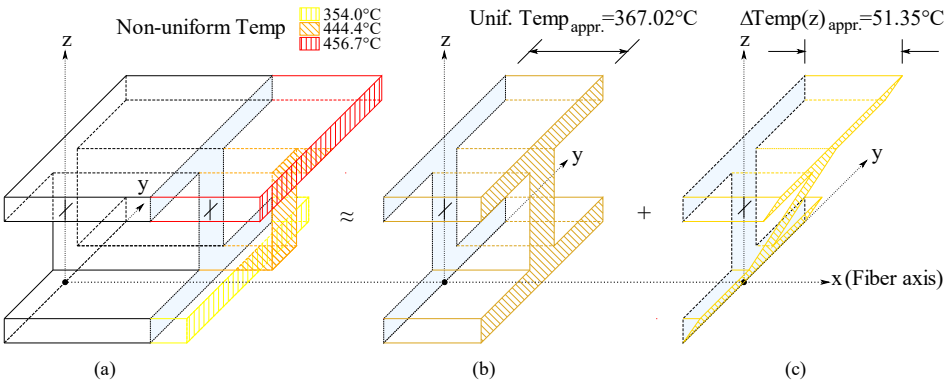

Fig. 52 Temperature components related to BEAM189 element axes (Test-1)

The uniform temperature component is applied at the lowest point of the BEAM189 cross-section since the fiber axis is at the outer edge of the bottom flange. So, the temperature at one point of the cross-section is approximated by Eq. (11).

$$Temp(z) \approx Unif\ Temp + Temp\ Grad(z) \times Z \tag{11}$$

In Eq. (11), *Unif Temp* is the approximate temperature value at the bottom flange (367.02°C), *Temp Grad*(z) is the thermal gradient in the web direction (0.23 °C/mm), and Z is the coordinate of a section point. Z-coordinates are positive since the reference system origin is at the outer point of the section over the fiber axis. As the gradient line passes through the lowest point of the cross-section, the gradient component is null at that point. Consequently, the temperature applied at the lowest point of the section is equal to the uniform temperature.

In the post-conditioning stage, the vertical load is applied at the upper-end nodes of the LINK180 elements by incremental displacements until the target value of 22.75 mm is attained. This target displacement value is adequate to record the ultimate load and the load-bearing capacity drop. A uniform temperature component and a z-z gradient are instantaneously applied to BEAM189 elements in the central part of the beam in this phase. The web temperature (444.4 °C) is also instantly applied as a uniform temperature in the BEAM189 elements representing the stiffeners and LINK180 elements. Fig. 53 shows a detail of the extruded stiffener displaying the controlled-displacement boundary condition. Time histories of vertical deflection (Uz) at the midpoint of the fiber and the force (Fz) in the top-end node of LINK180 elements are obtained at the end of the GMNIA.

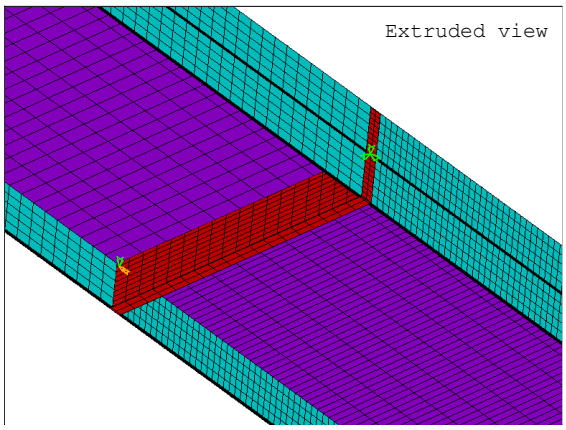

Fig. 53 FBM stiffener detail for Test-1

4.5.2 Cruciform Frame Model (CFM)

In the CFM, the tested beam subjected to LTB is idealized as a cruciform arrangement of fibers, where each fiber is made up of BEAM189 elements with rectangular cross-sections. This grid arrangement enables considering two bending directions for the web and better predicts the localized buckling produced by the high compressions on the thin web plate. The discretization consists of a grid of BEAM189 elements representing the web (illustrated in Fig. 54a in purple). Above and below the grid are grid lines idealizing the top and the bottom flange (cyan colored in Fig. 54a). The number of grid divisions in the vertical direction (*ndv*) is taken as 10, and the number of grid divisions in the longitudinal direction (*ndl*) is taken as 106. Therefore, the web is modeled with a grid with 11 horizontal fibers and 107 vertical fibers. In total, the web is made up of 1166 horizontal elements and 1070 vertical elements cruciform arranged. In turn, each flange is a fiber of 106 finite elements. Endplates and stiffeners are also vertical fibers of BEAM189 elements (red-colored in Fig. 54a), and they have the material and the cross-section indicated in the test (see Fig. 35a and Table 4). The cross-section dimensions

of the flange elements are the width and thickness of the thin plate defining the flanges (150.0×5.0 mm, in Fig. 36a). Besides, the material of the flange elements is that of the test (S5, in Fig. 35a). The cross-section dimensions of the web elements are 45.5×4.0 mm for the horizontal elements and 50.0×4.0 mm for vertical elements (4.0 mm is the thickness of the web plate, in Fig. 36a). The material of the web elements is the same as the web plate in the test (S2, in Fig. 35a). Lateral restraints in the global *y-y* direction are applied to the two nodes of the upper fiber where the load is applied and the two nodes of the lower fiber where the stiffeners are. Fig. 54b shows the finite element mesh extruded, showing all the components and the boundary conditions. Fig. 55 shows one vertical and one horizontal web fiber and the dimensions of their constituent BEAM189 elements.

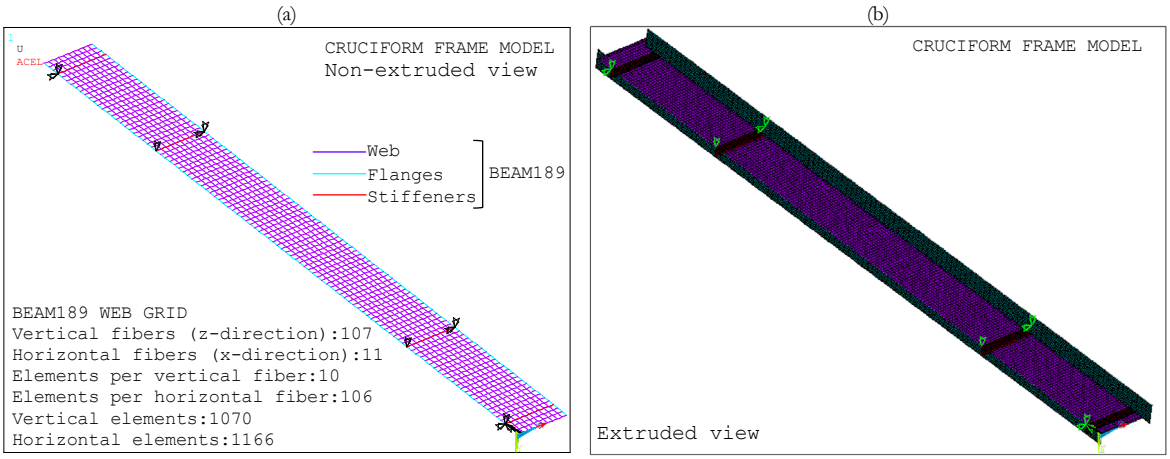

Fig. 54 CFM meshing and boundary conditions for Test-1.
(a) Non-extruded view. (b) Extruded view

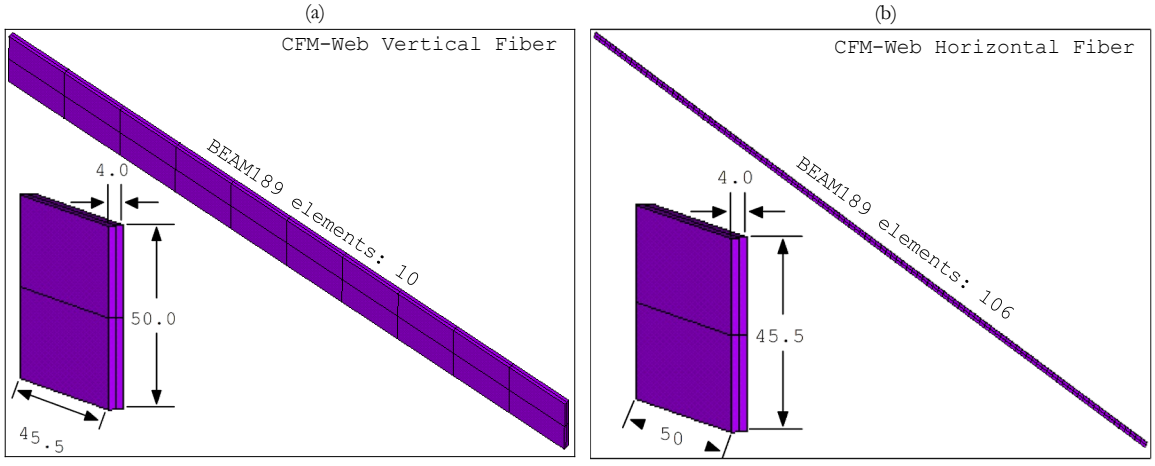

Fig. 55 Details of the CFM web fibers and dimensions of the fiber elements for Test-1, in mm. (a) Vertical fiber. (b) Horizontal fiber

The welded I-section is represented by the rectangular cross-sections of all its component elements, as shown in Fig. 56. The cross-sections of horizontal grid elements constitute the web. Each I-section flange is the cross-section of a BEAM189 finite element in the upper or

lower fiber as appropriate. The number of cells in the cross-section of elements forming the welded I-section is set to apply the pattern of residual stresses.

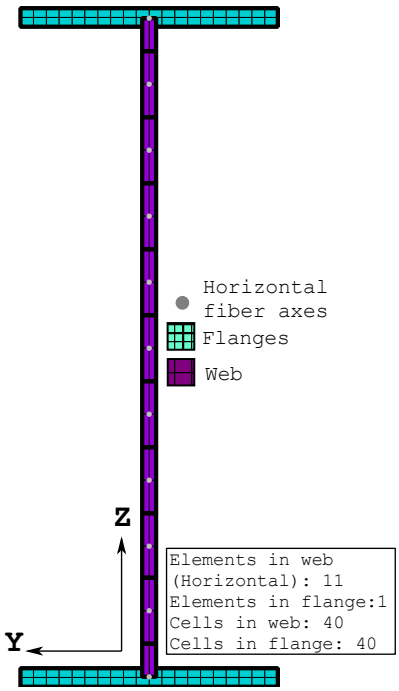

Fig. 56 CFM cross-section discretization and element cells for Test-1

Fig. 57 and Fig. 58 show the global and local buckling mode shapes chosen from the eigenvalue analysis, respectively. In Fig. 57b, the simple lateral curvature in the *y-y* direction typical of the global mode shape can be appreciated. In the local mode shape of Fig. 58a, the lateral undulations allow depicting the local web imperfections. Vertical undulations in the top flange in the extruded view of Fig. 58b are not visible in the non-extruded view of Fig. 58a. This occurs because, in the non-extruded deformed shape, only the fiber axes are shown. It means the fiber axis representing the top flange is not deformed, but its edges do, as expected. In the central zone of the beam, the extruded deformed shape of the top flange resembles a saddle surface containing various saddle points. The undulations of this surface depict local imperfections on the top flange. In the CFM, it is assumed that the displacements in the *y-y* direction are from the web. Therefore, the simulated amplitude in the *y-y* direction is the maximum lateral deflection obtained from the grid nodes for the global mode shape (in Fig. 57) and the grid nodes of the central part of the grid for the local buckling mode shape (in Fig. 58).

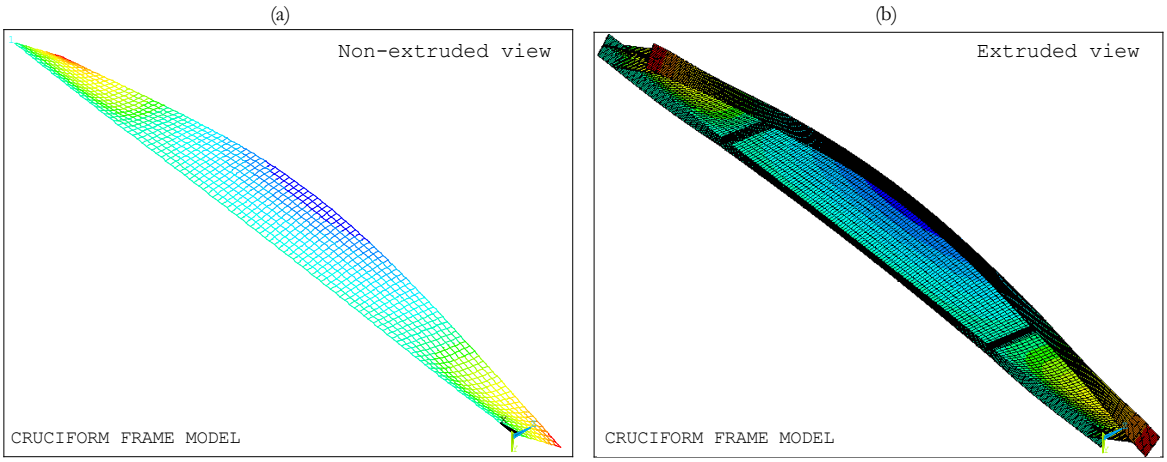

Fig. 57 CFM global mode shape for Test-1. (a) Non-extruded view. (b) Extruded view

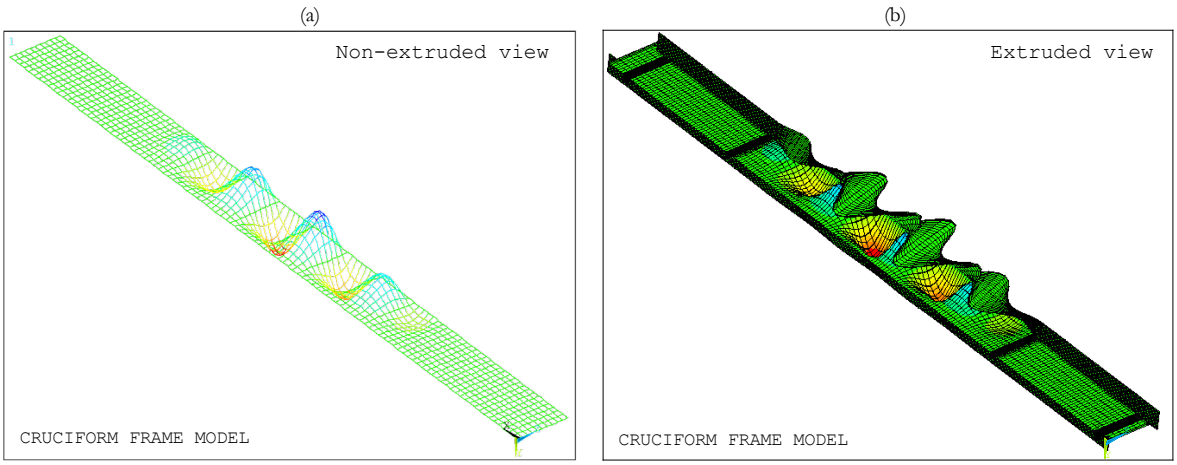

Fig. 58 CFM local mode shape for Test-1. (a) Non-extruded view. (b) Extruded view

The imperfect initial geometry is obtained by adding the imperfections to the node coordinates of the original finite element model, according to Eq. (10). In both local and global mode shapes, *x*-displacements and *z*-displacements are almost zero on the CFM fiber axes, so that *x*-imperfections and *z*-imperfections adding to *x*-coordinates and *z*-coordinates of the CFM are neglected. Consequently, the *x*-coordinates and *z*-coordinates are practically identical in the original geometry and the imperfect geometry. In the *y*-*y* direction, the imperfections are non-zero, but the *y*-coordinates of the original model, in this case, are zero. Therefore, the *y*-*y* imperfections are equal to the *y*-coordinates of the initial imperfect geometry. The global and local scale factors, GSF and LSF1, are calculated according to Eq. (2) and Eq. (3), and the global and local *y*-imperfections are calculated as shown in Eq. (6) and Eq. (9). The *y*-*y* imperfections plotted in Fig. 59 show similar positive and negative values. The imperfection values are obtained from combining the scaled and weighted lateral displacements of both buckling modal shapes and are present in the central zone of the beam, as expected. Out of the central zone of the beam and in the flanges, the *y*-*y* imperfections are null.

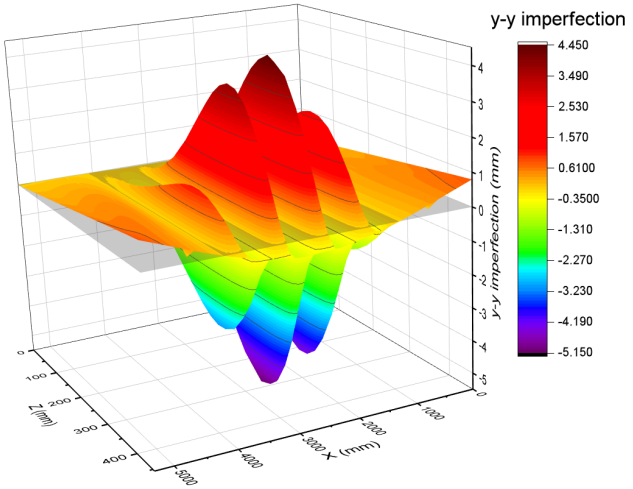

Fig. 59 Imperfect initial geometry of CFM for Test-1 (mm)

Compressive (blue) and tensile (red) residual stresses at room temperature in the web and flanges are applied to the cross-section cells of the BEAM189 elements that comprise the welded I-section, as shown in Fig. 60.

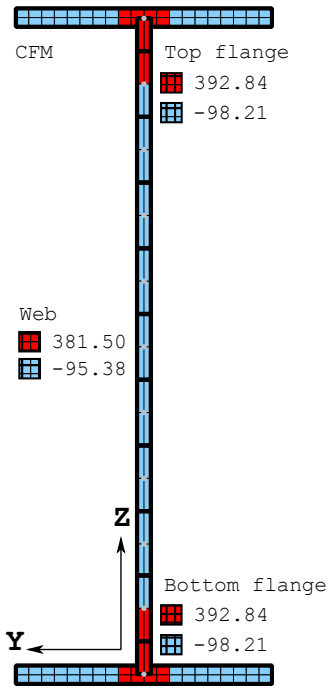

Fig. 60 CFM tensile and compressive residual stresses in the I-section for Test-1 [MPa]

For the thermal conditioning stage of the LTB-GMNIA, the target temperature at each part (top flange, bottom flange, and web) in the central zone of the beam (show in Fig. 40a) is directly specified as a uniform temperature to be attained in the BEAM189 elements of the top and bottom fibers (flanges) and the grid elements (web). Additionally, the web temperature

(444.4 °C) is directly specified as a uniform temperature to be attained in the BEAM189 elements representing the stiffeners. In the post-conditioning stage, the vertical load is applied at the top ends of the stiffeners by incremental displacements until the target value of 22.75 mm is attained. Uniform temperatures measured at each part of the beam are again applied instantaneously in this phase. Fig. 61 shows a detail of the extruded stiffener with the controlled-displacement boundary condition indicated. Time histories of vertical deflection (Uz) at the mid-point of the grid lower fiber and the force (Fz) in the top-end node of BEAM189 stiffeners are obtained at the end of the GMNIA.

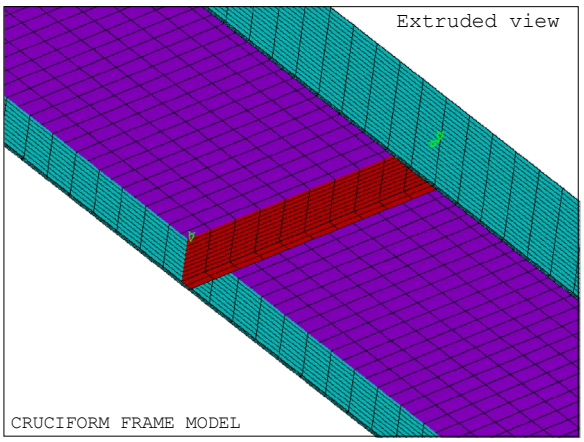

Fig. 61 CFM stiffener detail for Test-1

The summary of the full LTB-GMNIA implemented in both proposed Ansys modeling strategies for Test-1 and Test-3 is shown in the charts of Fig. 62a and Fig. 62b. The procedures are compatible with beams of constant cross-section.

4.5.3 Shell Models for numerical validation

Simulations of the tested FIDESC4 beams do not include residual stresses and thermal strains [23,24,80]. Therefore, they do not consider the same conditions as the FBM and CFM, making it challenging to compare numerical results directly. Consequently, new models with Ansys SHELL181 finite elements for Test-1 and Test-3, called Shell Models (SM, hereafter), were built to compare computation times. SHELL181 is a linear element with four nodes and six degrees of freedom at each node: three translations (Ux, Uy, Uz), and three rotations about the *x*, *y*, *z-global* directions (ROTx, ROTy, ROTz). This finite element is suitable in non-linear analyses of large rotations and large deformations where the thickness of the plates can change. It follows the first-order shear deformation theory of Reissner-Mindlin. A brief explanation of the LTB-GMNIA procedure implemented in a shell model is presented only for Test-1 because the methodology is the same for Test-3. The shell model for Test-1 is based on a geometry of 79 areas shown in Fig. 63a. The discretization is carried out with 14596 SHELL181 finite elements following the area distribution of Fig. 63a. The areas of the geometric model match the areas where the residual stresses are present, allowing their application to the shell elements following the tensile and compressive stress pattern of Fig. 42. According to the test setup, displacements in the global *y-y* axis are restrained at the eight points where the lateral restraint was applied (see red points in Fig. 40b). The load is applied at the edges where internal

stiffeners are located. Finally, the boundary conditions of the tested beam are imposed and shown in Fig. 63b together with the model mesh.

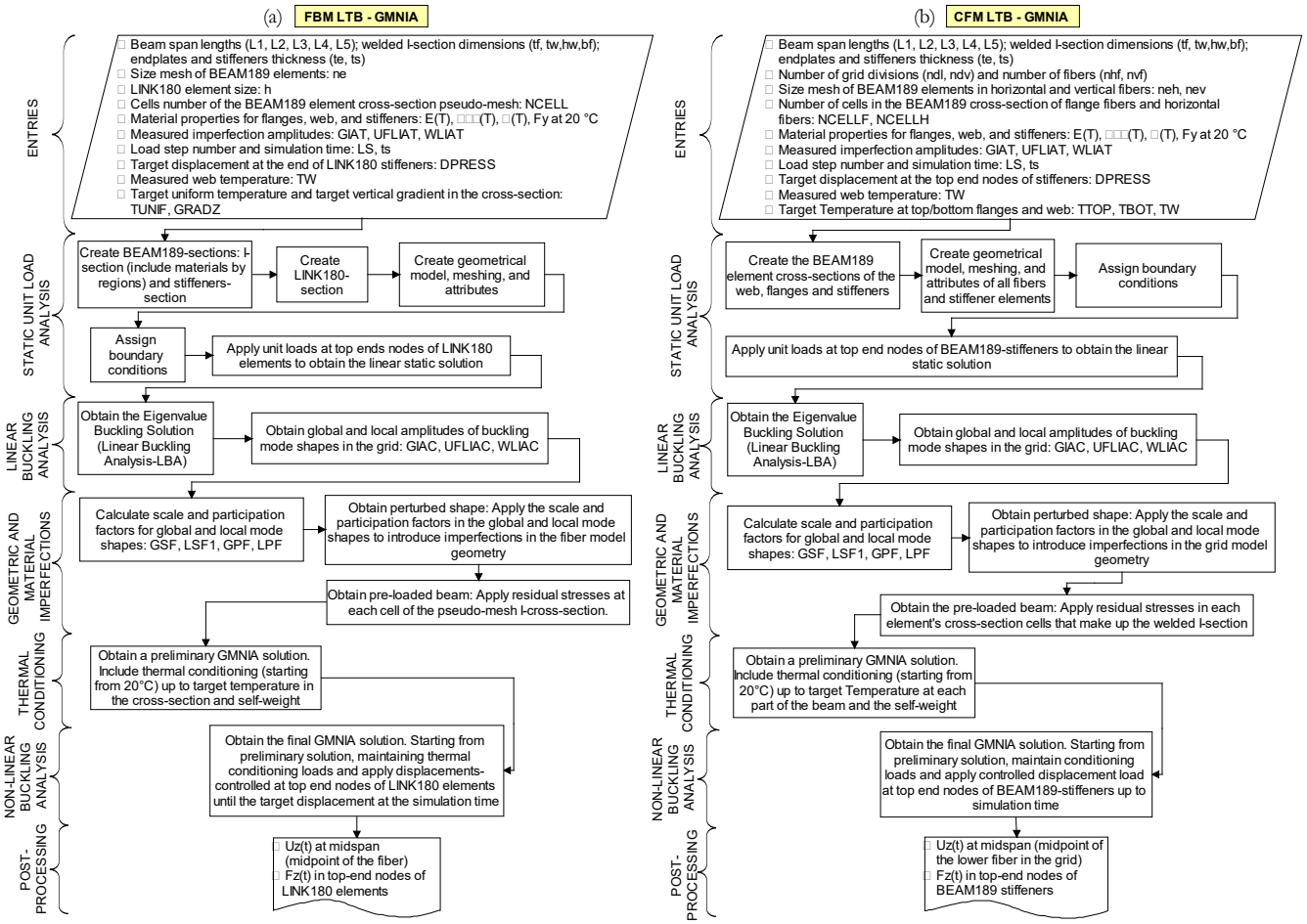

Fig. 62 Full LTB-GMNIA flowchart. (a) FBM. (b) CFM

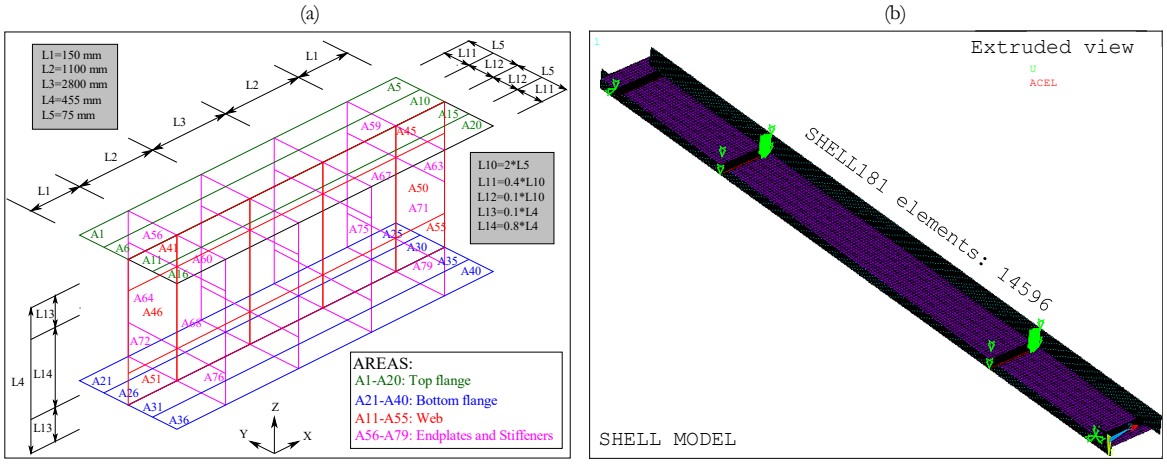

Fig. 63 Ansys-SM for Test-1. (a) Geometrical model: division into areas. (b) Meshing and boundary conditions

Fig. 64 shows the global and local mode shapes chosen from the linear buckling analysis. It can be seen that the global and local mode shapes exactly match those of the CFM modeling strategy shown in Fig. 57 and Fig. 58. For the global mode shape, the amplitude in the *y*-*y* direction is the maximum lateral deflection calculated at all nodes. For the local mode shape, the amplitudes are extracted from the nodes of the central part of the beam. Thus, the *y*-amplitude on the web is the maximum lateral deflection calculated at web nodes, and the *z*-amplitude on the top flange is the maximum vertical deflection calculated at top flange nodes.

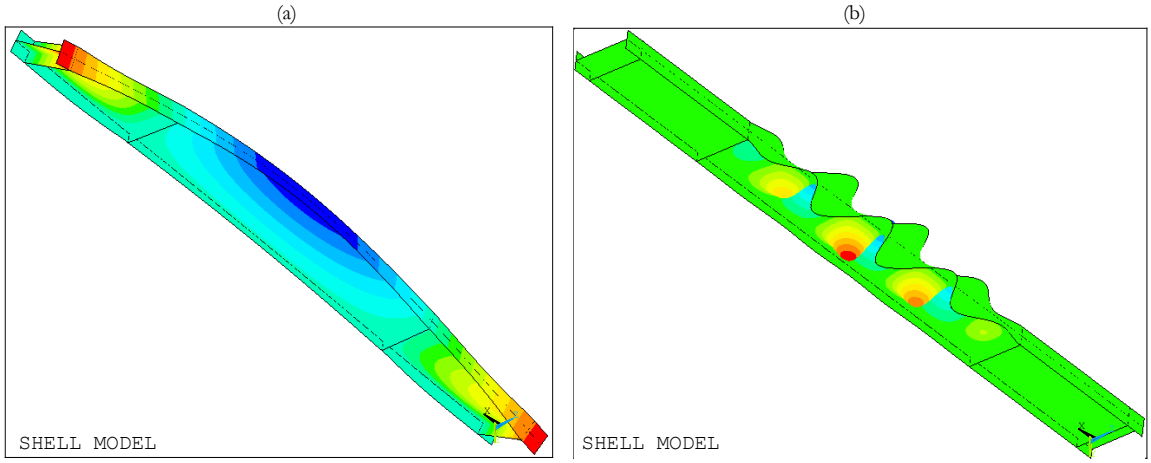

Fig. 64 Ansys-SM for Test-1. (a) Global mode shape. (b) Local mode shape

The SM discretization allows the scaling and combination of the two selected buckling modes considering the amplitudes of the measured and calculated imperfections in each beam region. Thus, the scaling factors (GSF, LSF1, and LSF2) are calculated by Eq. (2) to Eq. (4). In this model, the global and local buckling mode shapes contribute in half to the initial imperfect geometry of the web, meaning the participation factors GPF and LPF1 taking values of ½. On the other hand, the contribution of the local buckling mode shape to the initial imperfect geometry of the top flange is full, meaning the local participation factor LPF2 is 1. Therefore, the global and local imperfections (GI and LI) are estimated according to Eq. (6) and Eq. (7), respectively. Finally, the imperfect initial geometry (IIG) can be approximated by adding the imperfections to the node coordinates of the original model, according to Eq. (10). The web and top flange imperfections are plotted in Fig. 65a and Fig. 65b, respectively. After revising the geometry, these imperfections are obtained by combining the scaled and weighted displacements of the global and local buckling mode shapes.

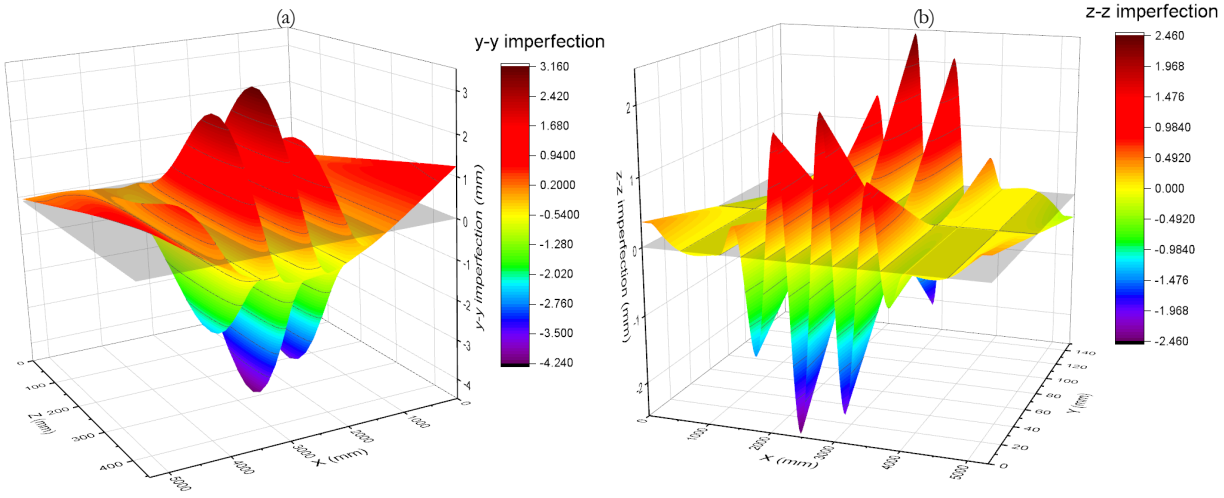

Fig. 65 (a) Imperfections added to *y*-coordinates of the web for Test-1 (mm). (b) Imperfections added to z-coordinates of the top flange for Test-1(mm)

The target temperature of the top and bottom flanges and the web in the thermal conditioning phase correspond to the measured temperatures. It is directly specified as a uniform temperature to be attained into the shell elements discretizing each part of the beam. The shell elements representing the stiffeners have the web temperature. In the post-conditioning stage, the controlled displacement mechanical load is directly applied at the top flange nodes on the top edge of the stiffeners until a vertical displacement target value of 22.75 mm is attained. The applied load is shown in Fig. 63b as green displacement boundary conditions. In this phase, measured temperatures are applied to the shell elements representing each part of the beam.

4.6 Validation of the proposed strategies

The proposed modeling strategies are validated using the experimental results of FIDESC4 Test-1 and Test-3 and compared to the results of the Safir and Abaqus numerical simulations reported in [23].

4.6.1 Test-1 validation

Fig. 66 shows the total force applied (P) versus the beam mid-span vertical deflection (Uz) at the bottom flange mid-point for Test-1, FIDESC4 simulations, and the proposed modeling strategies. Fig. 66 also includes the P-Uz relationships of the simulations carried out in Ansys without residual stresses and thermal strains to observe how these affect the force and displacement predictions. The total force P acting on the beam is obtained by adding the force in each stiffener. The P-Uz curves for Test-1, FIDESC4 simulations, and CFM and SM are drawn up to 25 mm of vertical deflection because it was the maximum deflection reported in the FIDESC4 numerical simulations included in [23]. The P-Uz relationship of the FBM is drawn up to 35 mm because the ultimate load is reached at 31.03 mm. The curves of Ansys simulations without residual stresses and thermal strains (indicated as FBM**, CFM**, and SM** in Fig. 66) are drawn at deflections higher than 25 mm because they all are advanced

from those including them. The total force and vertical deflection results show that both proposed modeling strategies (FBM and CFM) are validated satisfactorily against Test-1 results. Simulation results also reveal that CFM gets better deflection predictions than the FBM. Comparing the results of the FBM and CFM simulations with and without residual stresses and thermal strains shows that it is necessary to include these initial conditions in the GMNIA because they correct the force and deflection predictions, resulting in a P-Uz curve closer to the test. Including these initial conditions in the simulations significantly improve the P-Uz curve trajectory. It is noted that the predictions of the Ansys models without residual stresses and thermal deformations underestimate the stiffness for the early force values and overestimate the ultimate load and the deflections. Incorporating these initial conditions is manifested in an additional stiffness towards the first part of the P-Uz curve and a decrease of the ultimate load and the ultimate deflection. Since the beam is allowed axial displacement, the extra stiffness may be due to the tensile pre-stressing introduced by the initial thermal strains. The decrease in LTB strength is due to a mixture of the unfavorable effects of residual stresses and the adverse effects of geometric imperfections increased by thermal strains. In conclusion, modeling with residual stresses and thermal strains reproduces the conditions of tested FIDESC4 beams subjected to LTB since these are problems with initial stresses and initial strains.

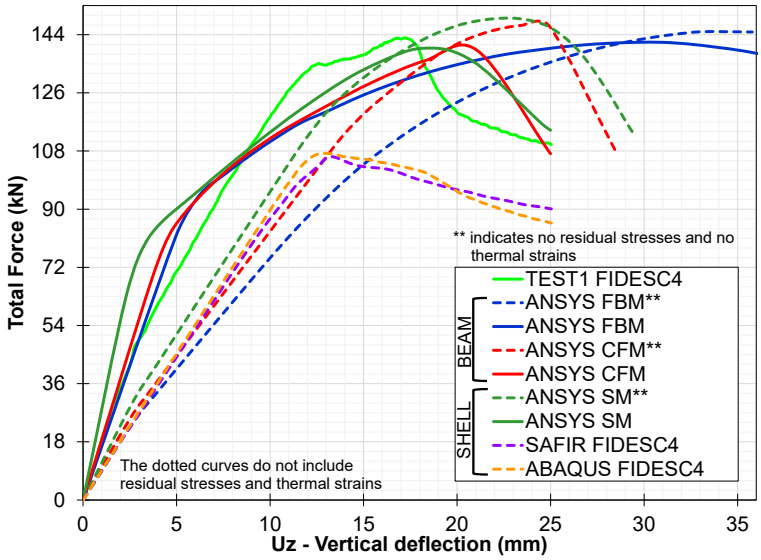

Fig. 66 Total applied load versus vertical deflection at the bottom flange mid-point in the beam mid-span for Test-1

The ultimate load (P_{ult}) and the ultimate vertical deflection (Uz_{ult}) at the bottom flange mid-point in the beam center from the test, FIDESC4 simulations, and the proposed modeling strategies with and without residual stresses and thermal strains are compared in Table 6. The ultimate cumulative strain energy (E^{ε}_{ult}) associated with the mechanical work in the beam is also included as a criterion to complement the evaluation of the simulation results. This mechanical work is related to the deformation (elastic and plastic) accumulated until the ultimate load capacity is reached; therefore, ultimate cumulative strain energy (E^{ε}_{ult}) is calculated as the area under the curve P vs. Uz up to the ultimate load in Fig. 66. In Table 6, the best result of the two proposed modeling strategies, FBM and CFM, is underlined and bold. It can

be seen that CFM adequately predicts both total force and vertical deflection. FBM predicts the ultimate load value well, but its ultimate deflection is larger than the measured, so its ultimate cumulative strain energy is overestimated by 1.13 times regarding the test. It means FBM does not fully represent the beam buckling scenario since the ultimate load occurs at a higher deflection value than the actual one. Table 6 also lists the ultimate flexural moment (M_{ult}) in the heated part of the beam in pure bending, which is calculated as half the ultimate load ($½P_{ult}$) multiplied by the distance from the end support to the load application point (L2) (see Fig. 38). Again, FBM has a slightly better prediction of M_{ult} than CFM, but CFM better reproduces the structure's response up to the end of the test.

Table 6. Comparison of results between FIDESC4 simulations, experimental test, and proposed modeling strategies with and without residual stresses and thermal strains for Test-1

		P_{ult} (kN)	Uz_{ult} (mm)	E^{ε}_{ult} (J)	M_{ult} (kN-m)	$\frac{P^{Num}_{ult}}{P^{Exp}_{ult}}$	$\frac{Uz^{Num}_{ult}}{Uz^{Exp}_{ult}}$	$\frac{E^{Num}_{ult}}{E^{Exp}_{ult}}$
BEAM MODELS	TEST 1 FIDESC4	142.96	17.13	1635.63	78.63	---	---	---
	Ansys FBM**	144.93	35.79	3599.20	79.71	1.01	2.09	2.20
	Ansys FBM	**141.61**	31.03	3485.31	**77.89**	**0.99**	1.81	2.13
	Ansys CFM**	146.88	24.95	2322.34	80.79	1.03	1.46	1.42
	Ansys CFM	139.05	**21.10**	**2147.61**	76.48	**0.97**	**1.23**	**1.31**
SHELL MODELS	Ansys SM**	148.96	21.78	2040.44	81.93	1.04	1.27	1.25
	Ansys SM	139.85	18.37	1877.84	76.92	0.98	1.07	1.15
	Abaqus SM FIDESC4	107.26	13.02	756.48	58.99	0.75	0.76	0.46
	Safir SM FIDESC4	106.26	13.23	757.50	58.44	0.74	0.77	0.46

** indicates that residual stresses and thermal strains are not included. The best result of the two proposed modeling strategies, FBM and CFM, is underlined and bold.

Table 7 shows the percentage overestimation of P_{ult}, Uz_{ult}, and E^{ε}_{ult} by the modeling strategies without residual stresses and thermal strains compared to those including them. Not considering these initial conditions in the models leads to overestimates of all three predictions, with the overestimation of the Uz_{ult} being higher. SM** makes the highest overestimates in all three predictions, followed by CFM** and the lowest by FBM**.

Table 7. Overestimation of the predictions of the proposed models without residual stresses and thermal strains for Test-1

	P_{ult} [%]	Uz_{ult} [%]	E^{ε}_{ult} [%]
Ansys FBM**	2.34	15.34	3.27
Ansys CFM**	5.63	18.25	8.14
Ansys SM**	6.51	18.58	8.66

Table 8 shows the ratio of Test-1 ultimate moment (M_{ult}) to the elastic bending moment of the section under non-uniform temperature (My_{fire}). The ratio indicates that the buckling limit state controlling failure occurs at an ultimate load (P_{ult}) equal to 46.8% of the elastic load (P_y= 305.43 kN).

Table 8. Relationship between the ultimate moment in the heated part of the beam and elastic bending moment for Test-1

M_{ult}^{Test} (kN-m)	$My_{fire}^{Theor.}$ (kN-m) [75,77]	$\left\lvert \frac{M_{ult}^{Test}}{My_{fire}^{Theor}} \right\rvert$
78.60	167.98	0.468

Fig. 67 compares the buckling shape (failure mode) of Test-1 with those obtained in previous FIDESC4 numerical simulations (Fig. 67e and Fig. 67f) included in [23] and with those obtained with the proposed modeling strategies. At the beginning of the experiment, a white-colored grid of 18 equal spaces was drawn on the top flange (in the heated central zone) to evidence the site of the local failure. The experimental deformed shape (Fig. 67a) shows that the local failure in the top flange is offset from the beam mid-span section, i.e., at the end of the first third of the heated zone over the 5th grid line drawn on the top flange. The FBM deformed shape (Fig. 67b) represents the global LTB failure in the heated central part of the beam but cannot capture the local failure shape in the top flange. However, vertical deflection isocontours on the web (blue colored) evidence the high compressions taking place in the failure zone. The CFM deformed shape (Fig. 67c) correctly reproduces the site where the local buckling on the top flange occurs and shows the web local buckling depicted by some web undulations in the middle span and the typical curvature characterizing the global LTB. The local buckling phenomena of the top flange and the web reproduced by CFM and Ansys-SM are shown in Fig. 67c, Fig. 67d, and Fig. 68. Images are practically identical, and both reproduce well the experimental failure, demonstrating that CFM can correctly reproduce the global and localized LTB failures. The advantage of CFM over Ansys-SM is its simplicity and the significant reduction of the number of elements used for the discretization, which reduces the computational cost. These advantages (accuracy and simplicity) make CFM a simple and low-cost alternative for simulating LTB in class-4 steel members under fire.

Since the bending generates compression stresses in the top flange and most of the web, the occurrence of tensile stress patterns in these areas demonstrates that some tensile residual stresses remain after the LTB failure. This phenomenon can be observed in Fig. 69, where general and detailed views of the axial stress isocontours at the simulation end time for each Ansys modeling strategy are shown. The details in Fig. 69d to Fig. 69f show red and yellow tension stress bands in the top welded zone at the simulation end time, demonstrating the existence of tensile residual stresses in the top compressed part of the beam. Fig. 69 also shows that tensile residual stresses in the top compressed part, in the unheated zone of the beam, are less dissipated than in the heated zone. This behavior indicates that residual stresses should not be neglected in the structural analysis of steel members with class-4 cross-sections under localized fire scenarios where the temperature along the members is non-uniform.

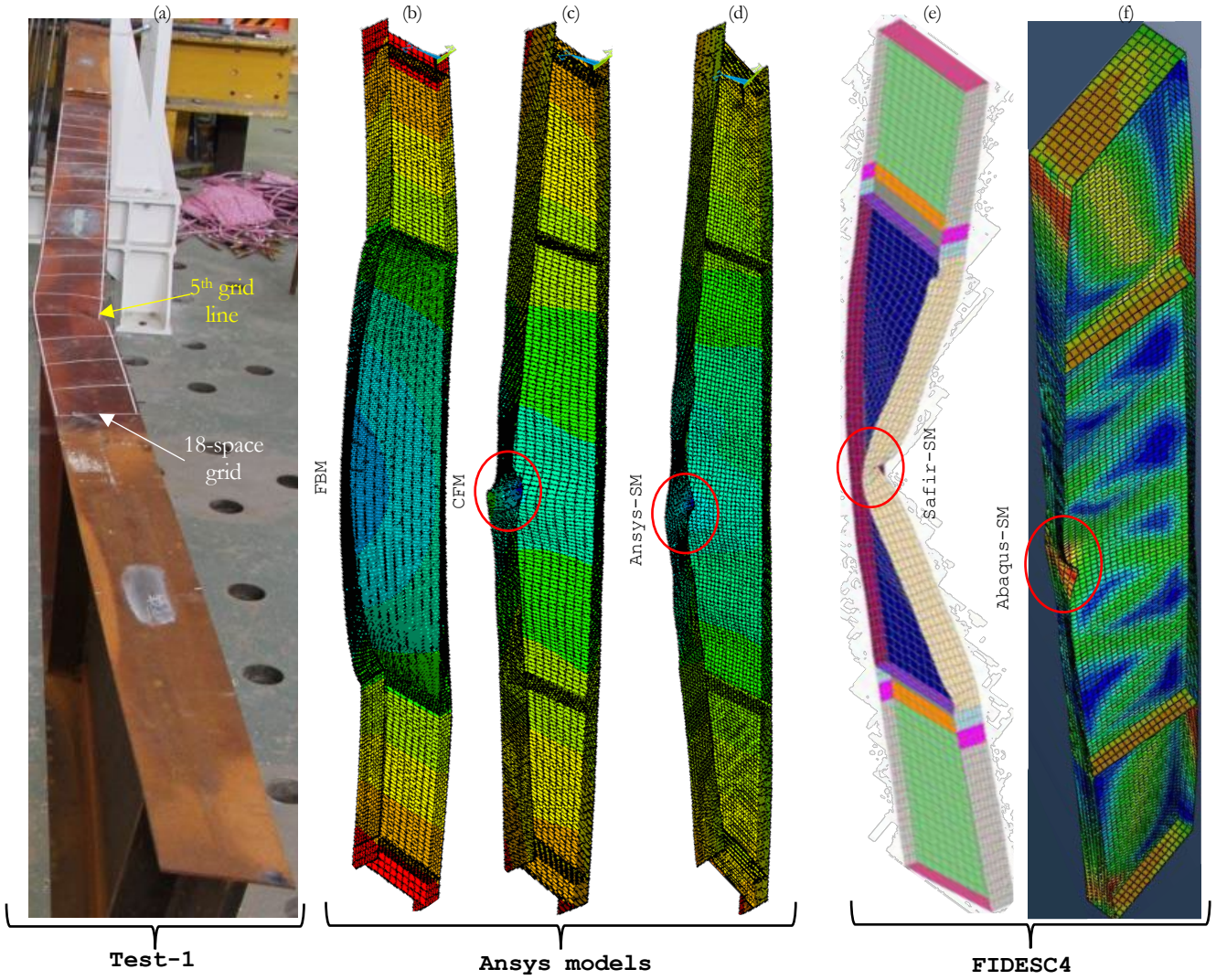

Fig. 67 Deformed shapes of Test-1 models. (a) FBM Uz deflection. (b) CFM Uz deflection. (c) Ansys-SM Uz deflection (d) FIDESC4 Test-1 [23]. (e) FIDESC4 Safir-SM [23]. (f) FIDESC4 Abaqus-SM [23]

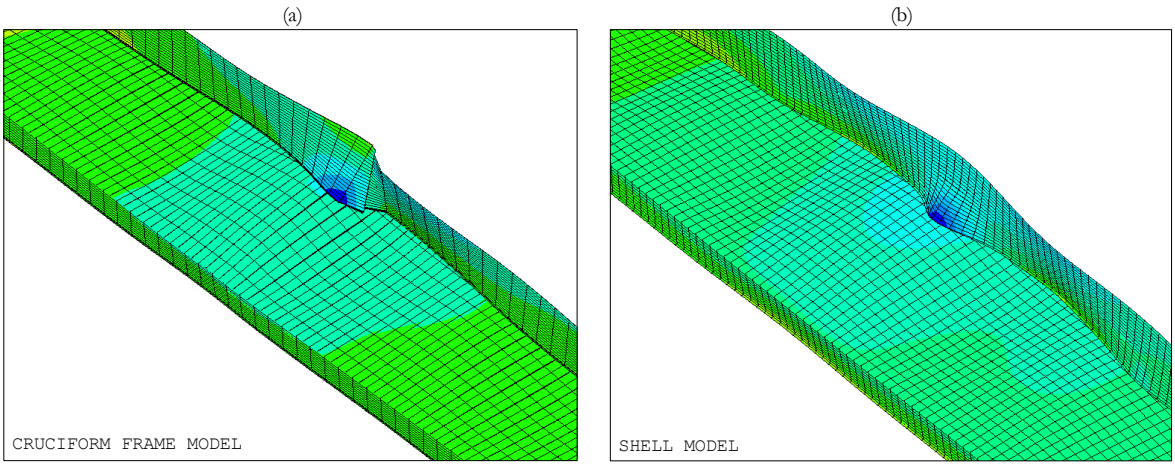

Fig. 68 Top flange and web local buckling detail. (a) CFM. (b) Ansys-SM

On the other hand, the tensile stresses localized on the web come from high web compressions produced by bending that generate buckling in the compressed zone of the web. Thus, the web behaves like a thin, slender plate subjected to compression, causing typical buckling undulations in the longitudinal direction, as shown in Fig. 69e and Fig. 69f. In other words, bending induces local buckling on the web. In Fig. 69, the compressive stresses are negative, and the tensile stresses are positive.

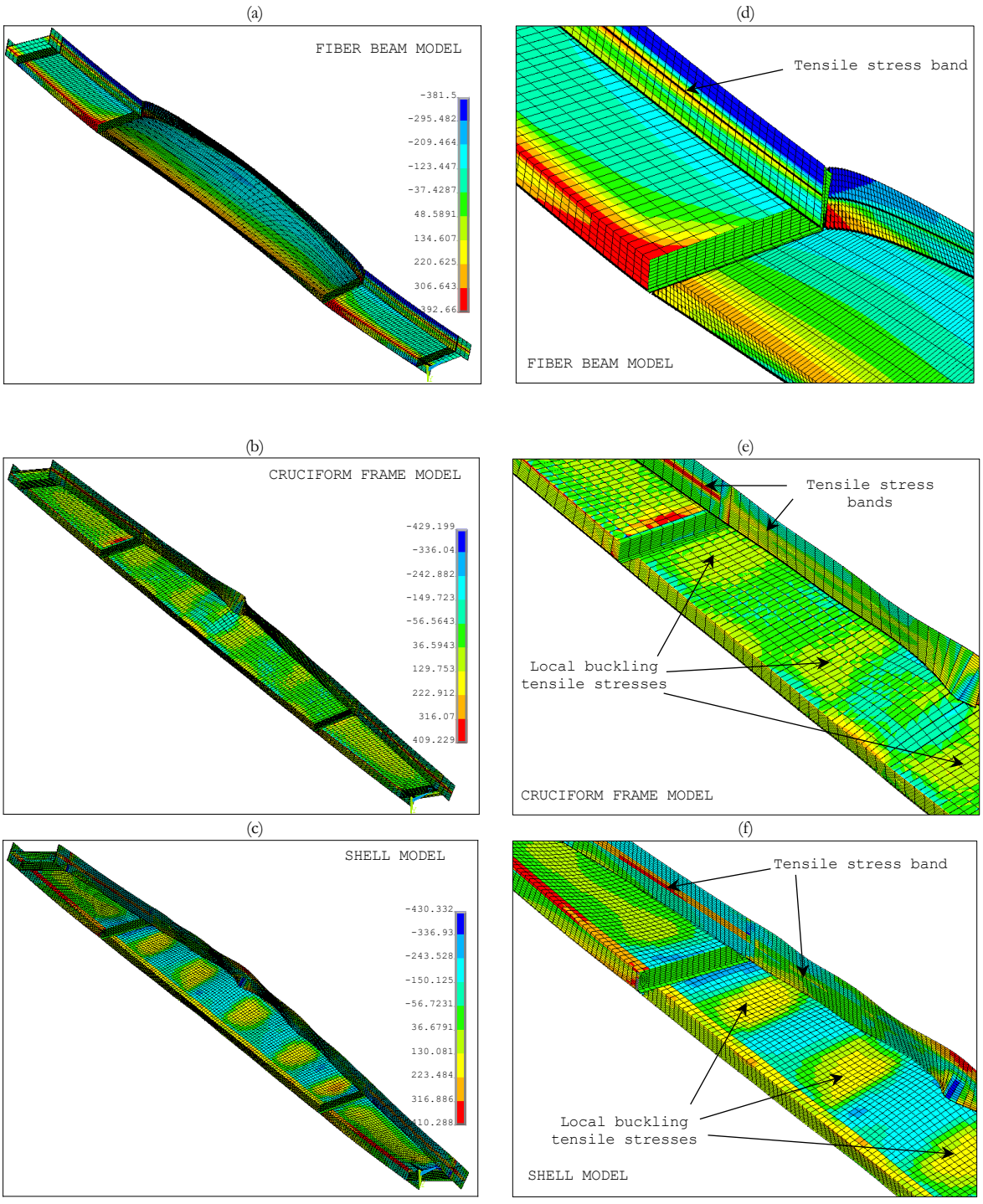

Fig. 69 Axial stresses at the end of the analysis [MPa]. (a,d) FBM. (b,e) CFM. (c,f) Ansys-SM

Some additional results at the end of the simulation related to torsional phenomena such as warping, bimoment, and bicurvature are shown in Fig. 70 to Fig. 72. These additional results are given only for FBM because they are easily available from the single fiber representing the tested beam. Fig. 70 and Fig. 71 show that the warping degree-of-freedom is null, and the bicurvature is significant at the beam mid-span where the maximum torsion occurs. The minimum (*MN*) and maximum (*MX*) warping points on the deformed shape (in Fig. 70) match the zero-bicurvature points (see Fig. 71). The changes of sign in the bicurvature diagram of Fig. 71 indicate warped torsion direction changes. The jumps in bicurvature and bimoment diagrams in Fig. 71 and Fig. 72 occur by the torsional resistance in the stiffener points. In turn, Fig. 73 shows the bicurvature-bimoment relationship representing the LTB evolution at mid-span. Initially, the bimoment is negative and then becomes ascending, indicating that the twisting direction of the cross-section changes during the test. The increase of the bimoment in the section is consistent with the LTB failure occurring at the beam mid-span. Although FBM cannot capture the local failure shape in the top flange, torsional results show that it simulates well the LTB phenomenon.

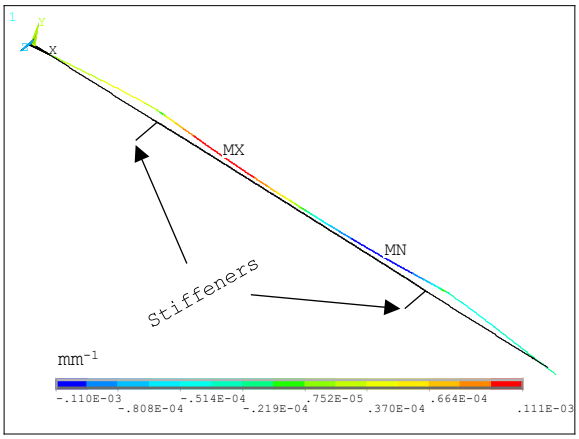

Fig. 70 Warping on the deformed shape

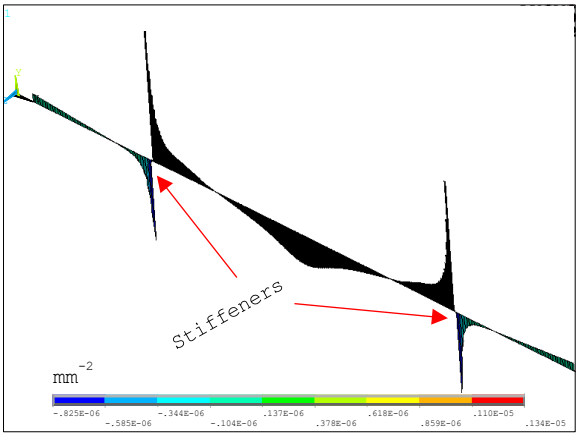

Fig. 71 Bicurvature

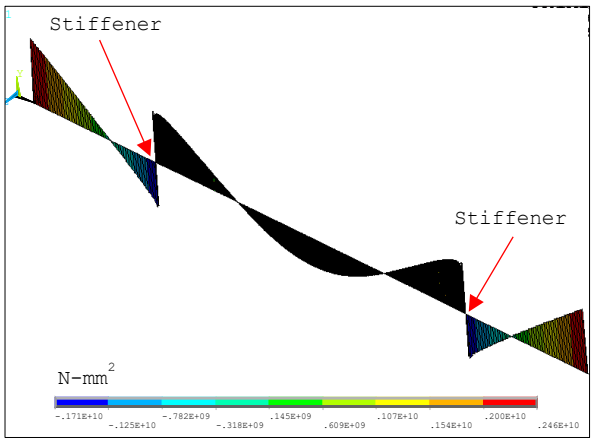

Fig. 72 Bimoment

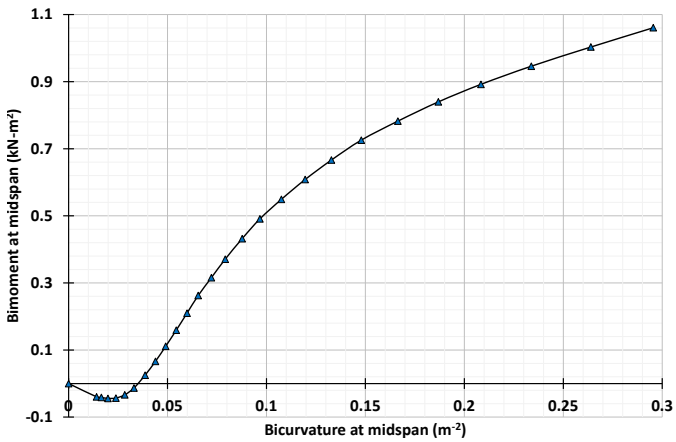

Fig. 73 Bimoment-bicurvature relationship

4.6.2 Test-3 validation

Fig. 74 shows the total force applied (P) versus the beam mid-span vertical deflection (Uz) at the bottom flange mid-point for Test-3, FIDESC4 simulations, and the proposed modeling strategies. Fig. 74 also presents the P-Uz curves of the simulations carried out in Ansys without residual stresses and thermal strains. The P-Uz curves for Test-3, FIDESC4 simulations, and CFM and SM are drawn up to 30 mm of vertical deflection according to FIDESC4 numerical simulations reported in [23]. The P-Uz relationship of the FBM is drawn past 35 mm because the ultimate load is only reached at 35.03 mm. The curves of Ansys simulations without residual stresses and thermal strains are drawn at deflections higher than 30 mm because they are advanced from those including them. Results indicate that the two proposed modeling strategies (FBM and CFM) validate satisfactorily against Test-3. Once more, CFM gets better deflection predictions than the FBM. Moreover, predictions of the Ansys models without residual stresses and thermal deformations again tend to underestimate the stiffness for the early force values and overestimate the ultimate load and defections. All other comments presented in Test-1validation are confirmed in Test-3 validation.

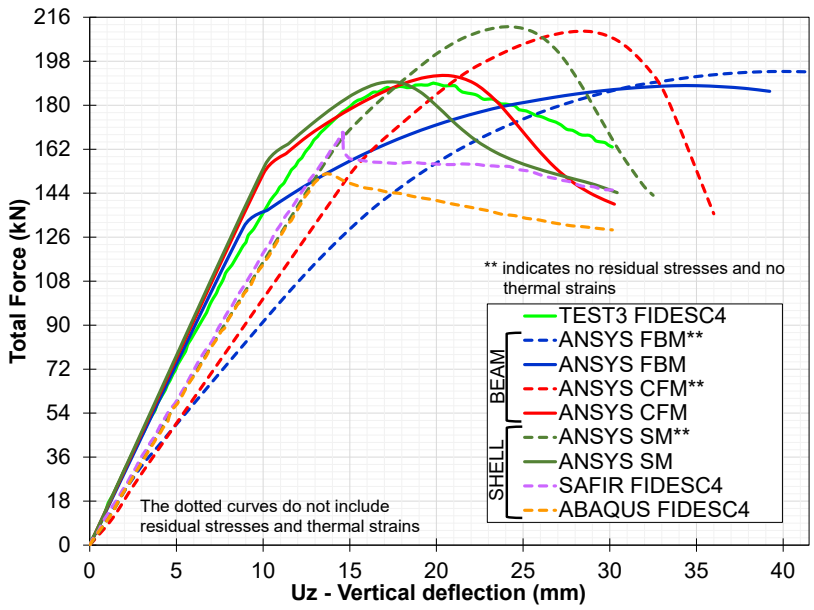

Fig. 74 Total applied load versus vertical deflection at the bottom flange mid-point in the beam mid-span for Test-3

In Table 9, the best result of the two proposed modeling strategies, FBM and CFM, is underlined and bold. Once again, FBM predicts the ultimate load value well, but its ultimate deflection is larger than the measured. FBM also has a slightly better prediction of M_{ult} than CFM, but CFM better reproduces the structure's response up to the end of the test. Finally, Table 10 shows the percentage overestimation of P_{ult}, Uz_{ult}, and E^{ε}_{ult} by the modeling strategies without residual stresses and thermal strains. Again, it is found that not considering these initial conditions in the simulations leads to overestimating all three predictions. SM** and CFM** make the highest overestimations for Uz_{ult} and E^{ε}_{ult}.

Table 9. Comparison of results between FIDESC4 simulations, experimental test, and proposed modeling strategies with and without residual stresses and thermal strains for Test-3

		P_{ult} (kN)	Uz_{ult} (mm)	E^{ε}_{ult} (J)	M_{ult} (kN-m)	$\frac{P^{Num}_{ult}}{P^{Exp}_{ult}}$	$\frac{Uz^{Num}_{ult}}{Uz^{Exp}_{ult}}$	$\frac{E^{Num}_{ult}}{E^{Exp}_{ult}}$
BEAM MODELS	TEST 3 FIDESC4	189.06	19.82	2410.10	103.99	---	---	---
	Ansys FBM**	193.82	39.99	5397.66	106.60	1.03	2.02	2.24
	Ansys FBM	**188.03**	35.06	5040.72	**103.42**	**0.99**	1.77	2.09
	Ansys CFM**	210.01	29.04	3794.94	115.50	1.11	1.47	1.57
	Ansys CFM	192.01	**20.85**	**2684.44**	105.61	1.02	**1.05**	**1.11**
SHELL MODELS	Ansys SM**	212.15	24.31	3125.80	116.68	1.12	1.23	1.30
	Ansys SM	189.23	17.91	2165.47	104.07	1.00	0.90	0.90
	Abaqus SM FIDESC4	151.95	13.71	1075.23	83.57	0.80	0.69	0.45
	Safir SM FIDESC4	168.92	14.60	1263.17	92.91	0.89	0.74	0.52

** indicates that residual stresses and thermal strains are not included. The best result of the two proposed modeling strategies, FBM and CFM, is underlined and bold.

Table 10. Overestimation of the predictions of the proposed models without residual stresses and thermal strains for Test-3

	P_{ult} [%]	Uz_{ult} [%]	E^{ε}_{ult} [%]
Ansys FBM**	3.08	14.07	7.08
Ansys CFM**	9.37	39.27	41.37
Ansys SM**	12.11	35.71	44.35

All discussions given of the simulation results of Test-1 are confirmed in the validation of Test-3, demonstrating that the proposed modeling strategies correctly simulate the LTB response of steel members with class-4 cross-sections under fire conditions with constant cross-section. On the other hand, the ratio of Test-3 ultimate moment (M_{ult}) to the elastic bending moment of the section under non-uniform temperature (My_{fire}) shown in Table 11 points out that the buckling limit state controlling failure occurs at an ultimate load (P_{ult}) equal to 45.4% of the elastic load (P_y= 416.56 kN).

Table 11. Relationship between the ultimate moment in the heated part of the beam and elastic bending moment for Test-3

M^{Test}_{ult} (kN-m)	$My^{Theor.}_{fire}$ (kN-m) [75,77]	$\left\lvert \frac{M^{Test}_{ult}}{My^{Theor}_{fire}} \right\rvert$
103.99	229.11	0.454

Fig. 75 compares the buckling shape (failure mode) of Test-3 with those obtained in previous FIDESC4 numerical simulations (Fig. 75e and Fig. 75f) included in [23] and with those obtained with the proposed modeling strategies. The experimental deformed shape (Fig. 75a) shows that the local failure in the top flange is near the beam mid-span section, i.e., over the 9th grid line drawn on the top flange. The FBM deformed shape (Fig. 75b) reproduces the global LTB failure in the heated central part of the beam but cannot capture the local failure shape in the top flange while the CFM deformed shape (Fig. 75c) correctly reproduces the place where local buckling occurs. The CFM deformed shape resembles that of Ansys-SM (Fig. 75d) and accurately represents the web undulations in the central part of the beam and the local buckling of the top flange. Details of the failure mode for CFM and Ansys-SM, evidencing their similarity, are shown in Fig. 76.

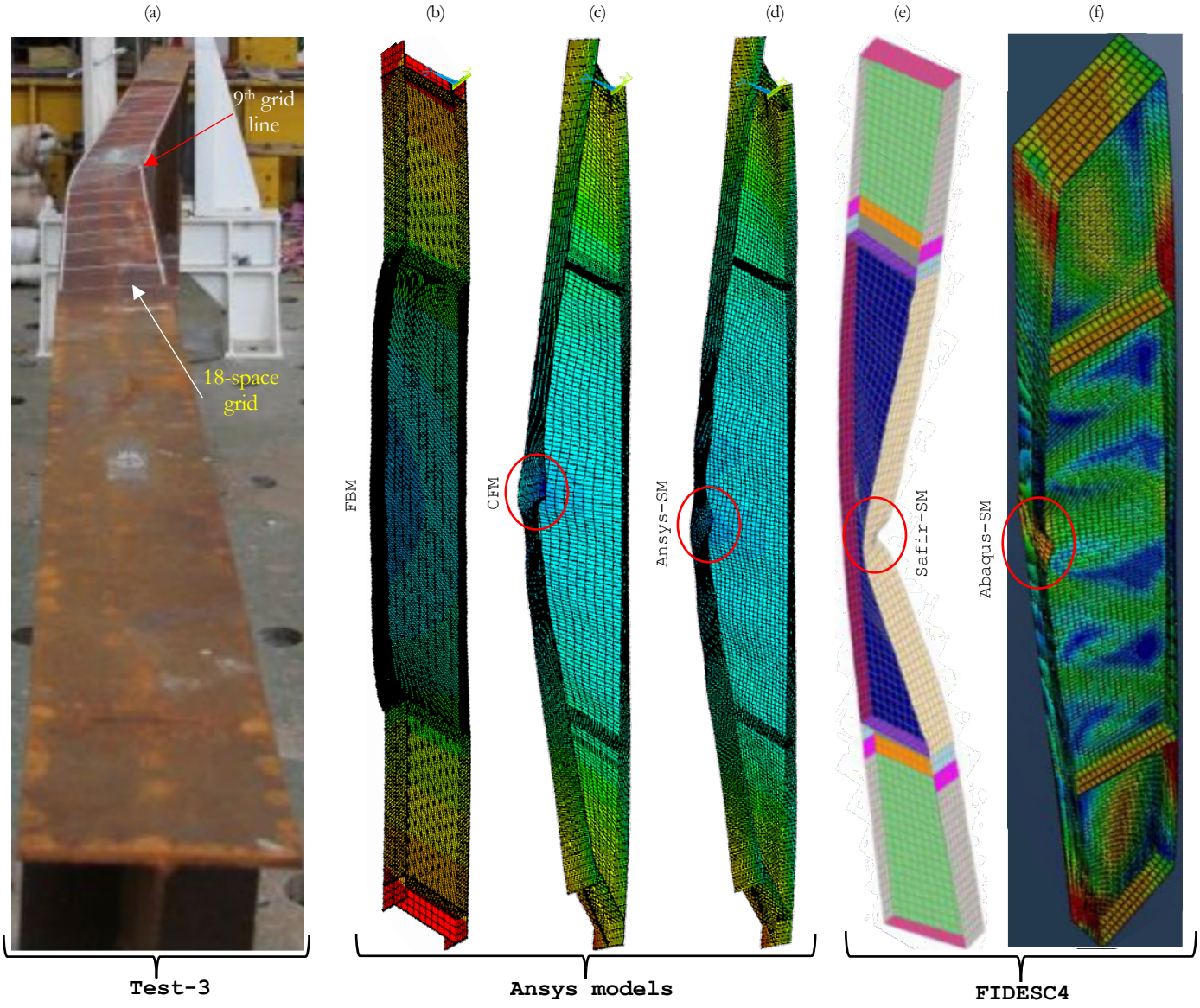

Fig. 75 Deformed shape of Test-3 models. (a) FBM Uz deflection. (b) CFM Uz deflection. (c) Ansys-SM Uz deflection (d) FIDESC4 Test-3 [23]. (e) FIDESC4 Safir-SM [23]. (f) FIDESC4 Abaqus-SM [23]

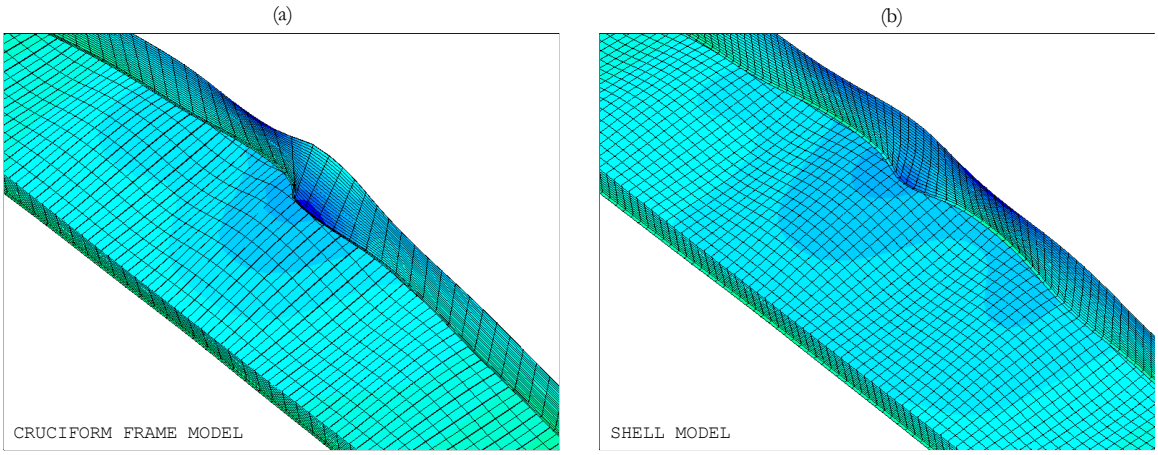

Fig. 76 Top flange and web local buckling detail. (a) CFM.
(b) Ansys-SM

Finally, the CPU times spent for each modeling strategy to carry out the full-GMNIA in Ansys for Test-1 and Test-3 are shown in Fig. 77. It can be seen that the best computation time is for CFM due to the reduction in the degrees of freedom and the complexity level achieved by discretizing with BEAM189 elements making it the best alternative to model the LTB problem in class-4 beams. In Fig. 77, the number of nodes, elements, and degrees of freedom is related to the CPU. For example, in Test-1 (Fig. 77a), it is observed that correct results can be achieved with a low-cost CFM of 2488 BEAM189 finite elements, 3413 nodes, and 23891 degrees of freedom instead of a high-cost SM of 14596 SHELL181 finite elements, 14789 nodes, and 88734 degrees of freedom. In Test-3 (Fig. 77b), the CFM nodes are slightly high (2508), whereas SM is still the same size. The time reduction of CFM versus SM is 52.2% in Test-1 and 46.7% in Test-3. Low-cost of CFM is caused by the quadratic interpolation of the BEAM189 finite element, which reduces the number of elements without losing the accuracy of results. On the other hand, the high refinement requirements in the cross-section pseudo-mesh to achieve the accuracy of the ultimate load increase the FBM computational cost, penalizing the advantage gained by saving the number of elements making it the highest computational cost. CPU times are calculated in Ansys using parallel distributed memory-MPI calculation in 6 physical cores on a Dell Mobile Workstation 7530/64 bits, Intel Xeon Processor-2.71 GHz, and Ram-32 GB.

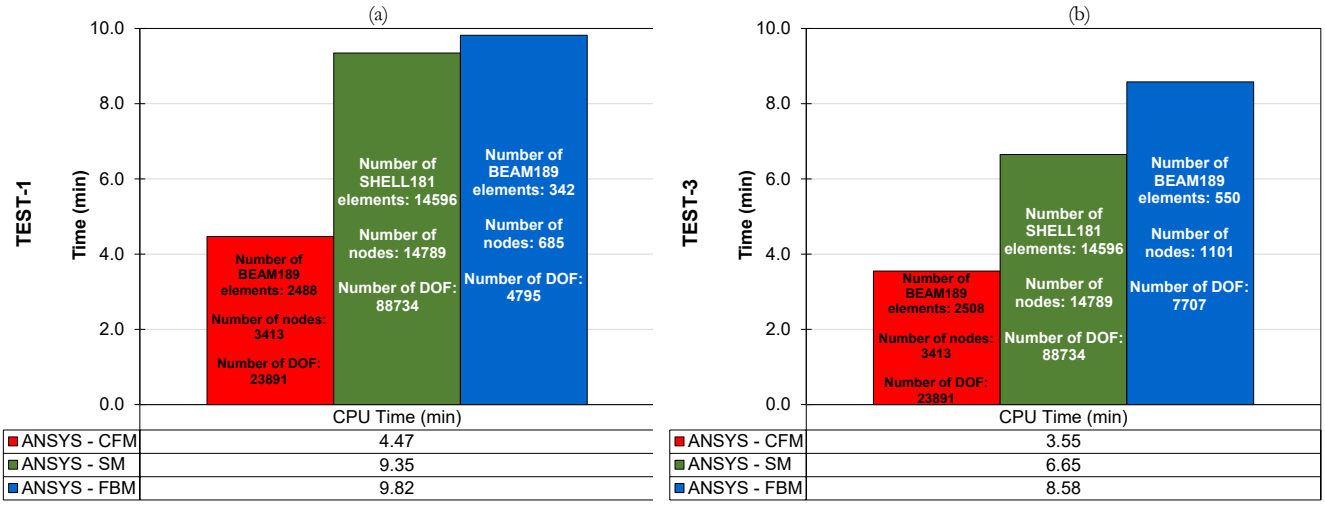

Fig. 77 Comparison of the CPU times of the proposed modeling strategies. (a) Test-1. (b) Test-3

Chapter 5

DISCUSSION OF RESULTS

Generally speaking, performance-based approaches applied to structures under fire seek to understand in-depth the effects that fire triggers on structures to reduce the associated risks. These approaches require countless numerical simulations for predicting the response of fire-affected steel structures, mostly with shell element-based models, because they enable high levels of detailing and better discretization. These approaches have provided valuable results, but they have a high computational cost. This aspect is essential because the most advanced analyses to understand better the structures' behavior under fire with safety and risk criteria need to be based on low computationally cost models. The reason is that these advanced analyses involve calibration and optimization tasks and sensitivity and failure probability studies, requiring many simulation repetitions. For example, in the reliability and risk advanced analyses, it is required to quantify the uncertainties of the problem under investigation. The most straightforward technique to quantify these uncertainties is by repeatedly evaluating the numerical model considering a random sampling of the input parameters. The above means that the numerical model run time should be pretty short for the probabilistic analysis computation time not to be very long (many months or perhaps years). For example, if one million simulations were used to evaluate the failure probability of the Cardington framework, the approximate run time using the Ansys-3D(No Spring) model would be one year on the high-performance workstation described in 3.8. Furthermore, it should also be noted that the computation time increases exponentially when the problems increase in complexity, as in large multi-member structures and those involving buckling failure limit states. Such is the case of the lateral-torsional buckling failures in thin-section steel beams (class-4) studied in this thesis or flexural-lateral buckling failures in slender-section steel columns. Note that if a similar exercise to the previous one was performed to evaluate the failure probability of the class-4 FIDESC4 beams subjected to lateral-torsional buckling, the approximate calculation time using the Ansys-CFM strategy would be 8.6 years in Test-1 and 6.5 years in Test-3 on the same high-performance workstation as above. Also, note that although the proposed models in this thesis are low-cost, an analysis of millions of repeated simulations based on these models already would demand considerable analysis time.

Unfortunately, most of the research, whether based on shell or beam models, has not paid close attention to the computational cost and has not reported computational times either, so it is difficult to make time comparisons. However, it could be verified in this thesis that the model built with finite beam elements using the Ansys-CFM strategy accurately reproduces the LTB response of the FIDESC4 class-4 beams (Test-1 and Test-3) with a significantly shorter computational time than the shell element-based model. For example, while an analysis of one million simulations with Ansys-CFM can last 8.6 years in Test-1 and 6.5 years in Test-3, the approximate run time with Ansys-SM would be 18 years in Test-1 and 13 years in Test-3 on the same high-performance workstation. Thus, in this case, the run time of analyses is duplicated when a shell element-based model is employed. That is not to count the computational cost overrun due to unforeseen events that often arise from unexpected execution stoppages by errors in the calculation codes that lead to debugging tasks, and so on. Although parallel computing, petaflops, and clusters can significantly reduce the computational

time, the time spent on probabilistic calculations can still be significant in many cases. Hence the importance of realistic models also having a low computational cost.

Some finite beam elements adapted to fire analysis enable assigning temperatures at the cross-section integration points for more realistic models; however, this temperature handling capability translates into the increased computational cost (storage and computational time). In contrast, in the proposed methodology to address the non-uniform temperatures in steel members, a uniform temperature and two time-varying average gradients approximate the non-uniform temperature in the cross-section of a Timoshenko finite beam element with satisfactory accuracy and low computational cost. The saving is related to the fact that the gradients are calculated explicitly with a bi-linear function without storing.

More realistic models can increase computational times. Therefore, it is essential to keep in mind that there must be a balance between modeling reality and computational cost to favor more complex analyses of multiple repetitions (such as probabilistic ones) that allow making decisions with safety and risk criteria. In consequence, it is worth analyzing when it is justified to sacrifice a more comprehensive structure response in favor of faster analysis. For example, the Ansys-2D(Spring) model successfully predicts the deflection at the midspan of the Cardington framework beam in less time than Ansys-3D(No Spring), as shown in Fig. 23. Thus, although the 3D response is not present in the 2D model, predictions are satisfactory with a lower computational cost.

In summary, to make more advanced analyses based on the repeated evaluation of numerical models of fire-affected steel structures feasible, computationally low-cost models should be sought, so beam-based models are suitable for this purpose. On the other hand, computationally high-cost models based on 3D-solid or shell elements are helpful in deterministic analyses of fire-affected parts of a structure and in deterministic analyses of the 3D-response of connections under fire.

Chapter 6

CONCLUSIONS AND FUTURE WORK

6.1 Conclusions

This thesis presents new proposals for modeling the thermo-mechanical response of steel structures under fire. The new proposals are built with the Ansys BEAM189 finite elements, which are simple but advanced seven-degree-of-freedom Timoshenko beam-type elements that reduce computational time and modeling effort. These savings in time, memory, and storage demand enable addressing complex steel structure analyses more easily and making feasible more complex structural fire engineering studies in which millions of simulations must be run quickly.

Chapter 3 presents a new methodology to represent the effects of non-uniform heating in structures subjected to fire action. The procedure uses beam-type finite elements with the Timoshenko formulation and the temperature field representation through an average value of the temperature and the section thermal gradients. The methodology was validated with results of the behavior (displacements) of the Cardington framework and the 2D numerical simulations of the Cardington experiment carried out by Franssen *et al.* and Santiago *et al.* [18,22,27]. The following conclusions were drawn:

- In a fire situation, the insulating elements in the frame members (the slab on the beam and the blocks between the columns) accentuate the thermal gradients, causing the steel (being a homogeneous material at environment temperature) to behave like a highly heterogeneous material. The non-uniform temperature makes the sections behave as if they were composed of several materials due to the temperature dependency of steel mechanical properties. This heterogeneity -asymmetrical- caused by the temperature field -asymmetrical- in the section, originates a coupling between the axial and bending effects. Therefore, an axial force produces a curvature, and a bending moment induces elongation of the members that affect the displacements field of the 3D-framework, favoring the appearance of displacements, rotations, and additional shearing effects, buckling and warping. These considerations justify Timoshenko's beam element in modeling the analyzed frame members. The above concludes that a good approximation of the mechanical structure response is determined by the type of beam element used to build the models.
- The proposed methodology is general, systematic, and enables the correct representation of a non-uniform and time-varying temperature field in the structure. These are significant advantages over other used strategies that represent the non-uniform temperature distributions from pre-established and constant relationships throughout the fire (e.g., the included in [17–20,22]).
- The methodology for determining the temperature field, including the variation of gradients in time, allows for 3D-structural analyses adapted to the 3D-nature of fire and the existence of non-uniform temperature fields in real structures.
- The non-uniform temperature field in the 3D- beam section calculated from the simulation

results of the section heat transfer over the entire fire scenario makes it possible that structural effects in the cooling phase can also be modeled. Although in the Cardington framework only deflections were measured up to the fire resistance time (when the first failure occurs), it can be seen that from about 17 to 21 minutes, the framework structural effects in the cooling phase (of the gas) are being considered; e.g., buckling evidence in the column.

- The proposed methodology with 3D-beam elements correctly predicts the 3D-field of displacements and 3D-effects that appear in structures under the action of fire (buckling, flexural-torsional buckling, warping, and coupling). Therefore, the methodology avoids using more complex finite elements (shell or solid), simplifying the structural modeling, and reducing its cost (modeling time, memory, storage, and computer calculation time). All of this allows tackling nonlinear phenomena present in structures subjected to fire action easily. It means that the proposed methodology represents a significant step forward towards the generalized application of performance-based approaches to deal with the effects of fire on structures. By doing so, this methodology also opens the path for a wider application of probabilistic models to complex structures under fire.

Chapter 4 presents two new methodologies implemented in Ansys to predict the LTB strength in steel beams with class-4 cross-sections subjected to fire action. The procedures use beam-type finite elements with the Timoshenko formulation and are based on a GMNIA that includes imperfections, residual stresses, and thermal strains. In the first modeling strategy (FBM), the beam is represented by a beam-type finite element fiber. In the second modeling strategy (CFM), the beam is represented by a beam-type finite element grid arrangement. Both modeling strategies were validated with experimental and numerical simulations of Test-1 and Test-3 carried out in the FIDESC4 [24] investigation on a slender beam of class-4 section and with a specific shell model of the same test built with Ansys. In all three cases, the validation of the ultimate load capacity of both tests was satisfactory. From the studies performed, the following conclusions were drawn:

- Both methodologies correctly predict the ultimate load of the class-4 steel members under fire and avoid using more complex finite element models. This simplification of the structural model is an important advantage over strategies that use shell elements (see, e.g., those included in [19,20]) and allows for full 3D analyses adapted to the 3D nature of the LTB phenomenon in real beams.

- The FBM strategy discretizes the steel member using a fiber representing the beam axis located at the outer edge of the beam where the boundary conditions are applied. Two types of elements are used to build the model: BEAM189 elements to model the fiber axis and LINK180 elements to transfer the load from the application points to the fiber axis representing the beam. FBM correctly predicts the ultimate load and is easy to build, and the number of elements and model building time is small, which is useful for quickly building multi-member models. Furthermore, its nodal results are easy to process. Although FBM is easier to build than CFM, its main disadvantages are that (a) FBM does not reproduce the local buckling shape and (b) FBM has a higher computational cost than CFM. Therefore, its use is not recommended for (a) post-buckling performance analyses and for (b) LTB analyses in steel beams requiring a large number of simulations as it would be the case of probabilistic and optimization analyses and involving knowledge of the collapse load. However, FBM can be very useful when the designer is interested only in the ultimate

load as in the LTB analysis under fire of multi-member steel structures belonging to industrial facilities or building frames.

- The CFM strategy discretizes the web and flanges of the steel member using a cruciform arrangement of BEAM189 element fibers to capture local buckling. This strategy is proposed to simplify the construction and reduce the computational cost of the shell models typically used for LTB analyses. CFM correctly predicts the structural response, the ultimate load, and even the local buckling failure of the tested beams. In addition, it is simpler, less computationally expensive than shell models. This reduction in computational cost opens the path for a wider application of probabilistic models to complex structures under fire and represents a significant step towards the generalized application of performance-based approaches to address fire effects. Therefore, CFM is recommended for evaluating the complete performance of the structure up to the collapse, as well as for optimization and probabilistic analyses.
- The simulation of the configuration and the conditions of the FIDESC4 experiments in slender beams of class-4 cross-section at high temperatures constitutes a modeling problem where initial stresses and initial strains are present. Therefore, both are indispensable for the proper calculation of the global response to the problem. The results of simulations carried out to validate the tests with and without residual stresses and thermal strains point out that the inclusion of these two initial conditions favorably modifies the LTB response of the tested beams. As a result, substantial improvements are evident in the evaluation of the initial stiffness of the beams and also in the calculations of ultimate load, ultimate displacement, and strain energy accumulated up to the ultimate load. In addition, it was verified that some tensile residual stresses remained after LTB failure, especially in the unheated part of the beam. This is another reason for including them in the LTB analysis of class-4 steel members in localized fire scenarios where the temperature along the member is not uniform.
- The study verified that the class-4 steel member strength under fire is significantly smaller than its elastic strength because buckling appears early [75,77]. In both tests, the buckling limit state established the ultimate load (P_{ult}) at approximately 46% of the theoretical elastic load (P_y).

6.2 Future work

The proposals developed in this thesis allow accurate, fast, low-cost, and easy to implement solutions. This contribution opens up a range of possibilities in modeling fire-affected steel structures that are still complex to solve today due to the high computational cost, such as optimization and probabilistic design studies of realistic steel structures affected by natural fire scenarios. Although researchers have developed several performance-based investigations and have found valuable results (mainly using FE models with many DOFs), the path is still vast. Accurate, low-cost predictive models of the behavior of steel structures under fire that make it feasible to carry out analyses to resolve uncertainties and reduce risks from fire attacks are needed. For example, in the case of class-4 fire-affected steel members, extreme situations aggravated by slenderness make it necessary to study the possible uncertainties arising in materials, loads, connections, prediction models for the comprehensive analysis of optimized members with safety criteria. These studies in class-4 steel members could also include, e.g., cyclic solicitations to evaluate the adverse effect of fire-triggering earthquakes, with low-cost

models being essential for these tasks. Likewise, for long-span steel portal frame beams, e.g., optimization studies based on low-cost models are necessary to find the optimum cross-section to reduce the weight, including fire solicitations and design criteria. However, before moving forward on this path, low-cost modeling strategies in class-4 steel members proposed in this thesis need to be extended to studying lateral-torsional buckling in steel beams with variable cross-sections and flexural-torsional buckling in steel columns with constant and variable cross-sections. Additionally, a combined methodology can also be formulated, taking advantage of the best of FBM and CFM modeling strategies for a more optimal steel structure's response to fire. Finally, it remains to explore new simplified approaches to analyze steel portal frames subjected to non-uniform temperature fields with beam elements that better represent the bilaminar effect in concrete-protected steel columns without sacrificing accuracy and computational time.

REFERENCES

[1] CTBUH. Tall Buildings in Numbers. The Global Tall Building Picture: Impact of 2019. CTBUH Journal Int J Tall Build Urban Habitat 2020:1–61.

[2] Arcelormittal. Wirkowise composite bridge: Europe's first road bridge with Arcorox weathering steel. 2020.

[3] Yoders J. Chicago's Union Station Tower Uses First 80-ksi Steel Sections in the US. ENRMidwest 2020.

[4] Shahbazian YWMMA. Fire Performance of Thin-Walled Steel Structures. 1st ed. London: CRC Press; 2020.

[5] Shyam-Sunder S, Gann RG, Grosshandler WL., Lew HS, Bukowski RW, Sadek F, et al. Final Report on the Collapse of World Trade Center Building 7, Federal Building and Fire Safety Investigation of the World Trade Center Disaster (NIST NCSTAR 1A). Washington: 2008. https://doi.org/10.6028/NIST.NCSTAR.1a.

[6] Qin C. Collapse simulations of steel buildings under fire. Colorado State University, 2016.

[7] Qin C, Mahmoud H. Collapse performance of composite steel frames under fire. Eng Struct 2019;183:662–76. https://doi.org/10.1016/j.engstruct.2019.01.032.

[8] Shakib H, Zakersalehi M, Jahangiri V, Zamanian R. Evaluation of Plasco Building fire-induced progressive collapse. Structures 2020;28:205–24. https://doi.org/10.1016/j.istruc.2020.08.058.

[9] Ahmadi MT, Aghakouchak AA, Mirghaderi R, Tahouni S, Garivani S, Shahmari A, et al. Collapse of the 16-Story Plasco Building in Tehran due to Fire. Fire Technol 2020;56:769–99. https://doi.org/10.1007/s10694-019-00903-y.

[10] Wright W, Lattimer B, Woodworth M, Nahid M, Sotelino E. Highway bridge fire assessment draft final report. Blacksburg: 2013.

[11] Peris-Sayol G, Paya-Zaforteza I, Balasch-Parisi S, Alós-Moya J. Detailed Analysis of the Causes of Bridge Fires and Their Associated Damage Levels. J Perform Constr Facil 2017;31:4016108. https://doi.org/10.1061/(ASCE)CF.1943-5509.0000977.

[12] Alos-Moya J, Paya-Zaforteza I, Garlock MEM, Loma-Ossorio E, Schiffner D, Hospitaler A. Analysis of a bridge failure due to fire using computational fluid dynamics and finite element models. Eng Struct 2014;68:96–110. https://doi.org/10.1016/j.engstruct.2014.02.022.

[13] Garlock M, Paya-Zaforteza I, Kodur V, Gu L. Fire hazard in bridges: Review, assessment and repair strategies. Eng Struct 2012. https://doi.org/10.1016/j.engstruct.2011.11.002.

[14] Payá-Zaforteza I, Garlock MEM. A numerical investigation on the fire response of a steel girder bridge. J Constr Steel Res 2012. https://doi.org/10.1016/j.jcsr.2012.03.012.

[15] Šulc S, Šmilauer V, Patzák B, Cábová K, Wald F. Linked simulation for fire-exposed elements using CFD and thermo-mechanical models. Adv Eng Softw 2019;131:12–22. https://doi.org/10.1016/j.advengsoft.2019.02.007.

[16] Horová K, Jána T, Wald F. Temperature heterogeneity during travelling fire on experimental building. Adv Eng Softw 2013;62–63:119–30. https://doi.org/10.1016/j.advengsoft.2013.05.001.

[17] Song YY, Huang ZH, Burgess LW, Plank RJ. The behaviour of single-storey industrial steel frames in fire. Adv Steel Constr 2009;5:289–302. https://doi.org/10.18057/IJASC.2009.5.3.5.

[18] Johnston RPD, Sonebi M, Lim JBP, Armstrong CG, Wrzesien AM, Abdelal G, et al.

The Collapse Behaviour of Cold-formed Steel Portal Frames at Elevated Temperatures. J Struct Fire Eng 2015;6:77–102. https://doi.org/10.1260/2040-2317.6.2.77.
[19] Nguyen XT, Park JS. Nonlinear Buckling Strength of Steel H-Beam under Localized Fire and Pure Bending. KSCE J Civ Eng 2021;25:561–73. https://doi.org/10.1007/s12205-020-0291-z.
[20] Kucukler M. Lateral instability of steel beams in fire: Behaviour, numerical modelling and design. J Constr Steel Res 2020;170:106095. https://doi.org/10.1016/j.jcsr.2020.106095.
[21] Prachar M, Hricak J, Jandera M, Wald F, Zhao B. Experiments of Class-4 open section beams at elevated temperature. Thin-Walled Struct 2016;98:2–18.
[22] Lou G, Wang C, Jiang J, Jiang Y, Wang L, Li G-Q. Fire tests on full-scale steel portal frames against progressive collapse. J Constr Steel Res 2018;145:137–52. https://doi.org/https://doi.org/10.1016/j.jcsr.2018.02.024.
[23] Wald, František Franssen J-M, Vila Real P, Oly R, Zhao B, Morente, Fernando Velda P. Fire design of steel members with welded or hot-rolled class-4 cross-section (FIDESC4). 2014th ed. Luxembourg: RFSC Publications; 2016. https://doi.org/10.2777/33944.
[24] Prachar M, Jandera M, Wald F, Zhao B. Lateral torsional-buckling of class-4 steel plate beams at elevated temperature: Experimental and numerical comparison. J Struct Fire Eng 2015. https://doi.org/10.1260/2040-2317.6.3.223.
[25] Prachar M, Jandera M, Wald F, Zhaob B. Fire resistance of slender section beams. Steel Constr 2014. https://doi.org/10.1002/stco.201410031.
[26] Couto C, Vila Real P, Lopes N, Zhao B. Numerical investigation of the lateral-torsional buckling of beams with slender cross-sections for the case of fire. Eng Struct 2016. https://doi.org/10.1016/j.engstruct.2015.10.045.
[27] Jandera Michal; Prachař MWF. Lateral-torsional buckling of class-4 section uniform and web tapered beams at elevated temperature. Thin-Walled Struct 2020;146. https://doi.org/10.1016/j.tws.2019.106458.
[28] Kucukler M, Gardner L, Macorini L. Lateral–torsional buckling assessment of steel beams through a stiffness reduction method. J Constr Steel Res 2015;109:87–100. https://doi.org/10.1016/j.jcsr.2015.02.008.
[29] Šorf M, Jandera M. Lateral-torsional buckling of slender cross-section stainless steel beams. Structures 2020;28:1466–78. https://doi.org/10.1016/j.istruc.2020.09.073.
[30] Franssen JM, Cooke GME, Latham DJ. Numerical simulation of a full scale fire test on a loaded steel framework. J Constr Steel Res 1995;35:377–408. https://doi.org/10.1016/0143-974X(95)00010-S.
[31] Quiel E, Garlock ME, Paya-Zaforteza I. Closed-Form Procedure for Predicting the Capacity and Demand of Steel Beam-Columns under Fire. J Struct Eng 2011;137:967–76. https://doi.org/10.1061/(ASCE)ST.1943-541X.0000443.
[32] Yang K-C, Lee H-H, Chan O. Performance of steel H columns loaded under uniform temperature. J Constr Steel Res 2006;62:262–70. https://doi.org/10.1016/j.jcsr.2005.07.001.
[33] Heidarpour A, Bradford MA. Local buckling and slenderness limits for flange outstands at elevated temperatures. J Constr Steel Res 2007;63:591–8. https://doi.org/10.1016/j.jcsr.2006.07.007.
[34] Oñate E. Structural Analysis with the Finite Element Method Linear Statics: Volume 2. Beams, Plates and Shells. 1st ed. Barcelona: Springer; 2013.
[35] Santiago A, Haremza C, Simões da Silva L, Rodrigues JP. Numerical behaviour of steel columns subject to localized fire loading. In: Topping BH V., Costa Neves LF, Barros RC, editors. Proc. Twelfth Int. Conf. Civil, Struct. Environ. Eng. Comput., Stirlingshire,

Scotland: Civil-Comp Press; 2009.
[36] Santiago A, Haremza C, Lopes F, Franssen JM. Numerical behaviour of steel columns under localized fire loading. In: Ed. Wald F, Burgess I, Kwasniewski L, Horová K, Caldová E, editors. Benchmark Stud. Exp. Valid. Numer. Model. fire Eng. 1st ed., Prague: CTU Publishing House; 2014.
[37] Burges I, Alexandrou M. Composite beams. In: Ed. Wald F, Burgess I, Kwasniewski L, Horová K, Caldová E, editors. Benchmark Stud. Verif. Numer. Model. fire Eng. 1st ed., Prague: CTU Publishing House; 2014.
[38] Burges I, Alexandrou M. Steel beams. In: Ed. Wald F, Burgess I, Kwasniewski L, Horová K, Caldová E, editors. Benchmark Stud. Verif. Numer. Model. fire Eng. 1st ed., Prague: CTU Publishing House; 2014.
[39] Burgess I, Plank R, Shephered P. Vulcan 2019.
[40] Kumar S, Miles S, Welch S, Vassart O, Zhao B, Lemaire AD, et al. EUR 23200 - Integrating advanced three-dimensional modelling methodologies for predicting thermo-mechanical behaviour of steel and composite structures subjected to natural fires. Luxembourg: Office for Official Publications of the European Communities; 2009.
[41] Rackauskaite E, Panagiotis K, Rein G. Model parameter sensitivity and benchmarking of the explicit dynamic solver of LS-DYNA for structural analysis in case of fire. Fire Saf J 2017;90. https://doi.org/10.1016/j.firesaf.2017.03.002.
[42] Axhag F. Plastic design of steel bridge girders. Luleå tekniska universitet, 1998.
[43] Pallares-Muñoz MR, Paya-Zaforteza I, Hospitaler A. A new methodology using beam elements for the analysis of steel frames subjected to non-uniform temperatures due to fires. Structures 2021;31:462–83. https://doi.org/10.1016/j.istruc.2021.02.008.
[44] Smyrnaios S V, Iliopoulos A, Vayas I. Truss models for inelastic stability analysis and design of steel plate girders. Eng Struct 2015;105:165–73. https://doi.org/10.1016/j.engstruct.2015.09.040.
[45] Possidente L, Tondini N, Battini J-M. 3D Beam Element for the Analysis of Torsional Problems of Steel-Structures in Fire. J Struct Eng 2020;146:4020125. https://doi.org/10.1061/(ASCE)ST.1943-541X.0002665.
[46] Franssen J, Cowez B, Gernay T. Effective stress method to be used in beam finite elements to take local instabilities into account. Fire Saf Sci 2014;11:544–57.
[47] Maraveas C, Gernay T, Franssen J-M. An equivalent stress method to account for local buckling in beam finite elements subjected to fire. J Struct Fire Eng 2019;10:340–53. https://doi.org/10.1108/JSFE-09-2018-0020.
[48] Maraveas C, Gernay T, Franssen J-M. Sensitivity of elevated temperature load carrying capacity of thin-walled steel members to local imperfections. Appl. Struct. Fire Eng. – ASFE 2017, Manchester: 2017. https://doi.org/10.1201/9781315107202-4.
[49] Maraveas C, Gernay T, Franssen J-M. Buckling of steel plates at elevated temperatures: Theory of perfect plates vs Finite Element Analysis. CONFAB 2017 - 2nd Int. Conf. Struct. Saf. Under Fire Blast Load., London: 2017.
[50] Maraveas C, Gernay T, Franssen J-M. Thin-walled steel members at elevated temperatures considering local imperfections: Numerical simulation of isolated plates. 9th Natl. Congr. Met. Struct., Larisa, Greece: 2017.
[51] Pallares-Muñoz MR, Payá-Zaforteza I, Hospitaler-Pérez A. New modeling strategies for analyzing lateral-torsional buckling in class-4 steel structural members at elevated temperatures using beam-type elements. Structures 2021;34:3508–32. https://doi.org/https://doi.org/10.1016/j.istruc.2021.09.087.
[52] Maraveas C. Local Buckling of Steel Members Under Fire Conditions: A Review. Fire Technol 2019;55:51–80. https://doi.org/10.1007/s10694-018-0768-1.

[53] Ansys. ANSYS Engineering Analysis System. User manual. Canonsburg, Pennsylvania: Houston, Pa. : Swanson Analysis Systems; 2019.
[54] Jeffers AE, Beata PA. Generalized shell heat transfer element for modeling the thermal response of non-uniformly heated structures. Finite Elem Anal Des 2014;83:58–67. https://doi.org/10.1016/j.finel.2014.01.003.
[55] Rigobello R, Coda HB, Munaiar Neto J. A 3D solid-like frame finite element applied to steel structures under high temperatures. Finite Elem Anal Des 2014;91:68–83. https://doi.org/10.1016/j.finel.2014.07.005.
[56] Alos-Moya J, Paya-Zaforteza I, Hospitaler A, Loma-Ossorio E. Valencia bridge fire tests: Validation of simplified and advanced numerical approaches to model bridge fire scenarios. Adv Eng Softw 2019;128:55–68. https://doi.org/10.1016/j.advengsoft.2018.11.003.
[57] Alos-Moya J, Paya-Zaforteza I, Hospitaler A, Rinaudo P. Valencia bridge fire tests: Experimental study of a composite bridge under fire. J Constr Steel Res 2017;138:538–54. https://doi.org/10.1016/j.jcsr.2017.08.008.
[58] Peris-Sayol G, Paya-Zaforteza I, Alos-Moya J, Hospitaler A. Analysis of the influence of geometric, modeling and environmental parameters on the fire response of steel bridges subjected to realistic fire scenarios. Comput Struct 2015;158:333–45. https://doi.org/10.1016/j.compstruc.2015.06.003.
[59] Davidson MT, Harik IE, Davis DB. Fire Impact and Passive Fire Protection of Infrastructure: State of the Art. J Perform Constr Facil 2013;27. https://doi.org/10.1061/(asce)cf.1943-5509.0000295.
[60] Allam A, Nassif A, Nadjai A. Behaviour of restrained steel beam at elevated temperature – parametric studies. J Struct Fire Eng 2019;10:324–39. https://doi.org/10.1108/JSFE-11-2018-0036.
[61] Latham DJ, Thomson G, Kirby BR, Wainman DE. Second natural fire test on a loaded steel frame at Cardington. Rotherham: 1986.
[62] Cooke GME, Latham DJ. The inherent fire resistance of a loaded steel framework. Steel Constr Today 1987;1:49–58.
[63] Srivastava G, Ravi Prakash P. An integrated framework for nonlinear analysis of plane frames exposed to fire using the direct stiffness method. Comput Struct 2017;190:173–85. https://doi.org/10.1016/j.compstruc.2017.05.013.
[64] EN 1993-1-2. Eurocode 3: Design of steel structures - Part 1-2: General rules - Structural fire design. Brussels: European Committee for Standardization; 2005.
[65] EN 1992-1-2. Eurocode 2: Design of concrete structures - Part 1-2: General rules - Structural fire design. Brussels: European Committee for Standardization; 2004.
[66] Purkiss JA, Li LY. Fire safety engineering design of structures. 3rd Editio. Boca Raton: CRC Press; 2013. https://doi.org/10.1201/b16059.
[67] Magisano D, Liguori F, Leonetti L, de Gregorio D, Zuccaro G, Garcea G. A quasi-static nonlinear analysis for assessing the fire resistance of reinforced concrete 3D frames exploiting time-dependent yield surfaces. Comput Struct 2019;212:327–42. https://doi.org/10.1016/j.compstruc.2018.11.005.
[68] Kiakojouri F, De Biagi V, Chiaia B, Sheidaii M. Progressive collapse of framed building structures: Current knowledge and future prospects. Eng Struct 2020;206:110061. https://doi.org/10.1016/j.engstruct.2019.110061.
[69] Mattieu J. Asegurar la resistencia al fuego de estructuras metálicas. Segur Contra Incend 2020:1–40.
[70] Elkawas AA, Hassanein MF, El Hadidy AM, El-Boghdadi MH, Elchalakani M. Behaviour of corrugated web girders subjected to lateral-torsional buckling: Experimental tests and numerical modelling. Structures 2021;33:152–68.

https://doi.org/10.1016/j.istruc.2021.04.057.
[71] Arcelormittal. Dusseldorf's iconic Kö-Bogen. 2014.
[72] Szychowski A, Brzezińska K. Local Buckling and Resistance of Continuous Steel Beams with Thin-Walled I-Shaped Cross-Sections. Appl Sci 2020;10. https://doi.org/10.3390/app10134461.
[73] Roth FMABJC. Theoretical and numerical stability analyses of unrestrained, mono-symmetric thin-walled beams. J Constr Steel Res 2003;59. https://doi.org/10.1016/s0143-974x(02)00007-x.
[74] Seres N, Fejes K. Lateral-torsional buckling of girders with class-4 web: Investigation of coupled instability in EC3-based design approach. Adv Struct Eng 2020;23:2442–57. https://doi.org/10.1177/1369433220915623.
[75] Kulak L, Grondin GY. Limit States Design In Structural Steel. 10th ed. Canadian Institute of Steel Construction; 2018.
[76] Schmidt H. Stahlbaunormen: Kommentar zu DIN EN 1993-1-6: Festigkeit und Stabilität von Schalen. Stahlbau-Kalender-Tag 2012, Stuttgart: Universität Stuttgart. Institut für Konstruktion und Entwurf; 2013. https://doi.org/www.p-s-p.de/uploads/downloads/Vortrag_Schmidt_Kommentar_zu_DIN_EN_1993-1-6_Stuttgart_2012-06.pdf.
[77] Buchanan A, Abu A. Steel Structures. Struct. Des. Fire Saf., New Zealand: John Wiley & Sons, Ltd.; 2016, p. 154–94. https://doi.org/10.1002/9781118700402.ch6.
[78] Thiébaud R, Lebet J-P. Lateral Torsional Buckling of steel bridge girders. Proc Annu Stab Conf SSCR n.d.:1–19.
[79] Agüero A, Baláž I, Koleková Y. New method for metal beams sensitive to lateral-torsional buckling with an equivalent geometrical UGLI imperfection. Structures 2021;29:1445–62. https://doi.org/10.1016/j.istruc.2020.11.047.
[80] Prachar M, Jandera M, Wald F, Zhao B. Lateral torsional-buckling of class-4 steel plate beams at elevated temperature: Experimental and numerical comparison. 2014. https://doi.org/fire.fsv.cvut.cz/fidesc4/Prachar-validation.pdf.
[81] Hambly EC. Bridge Deck Behaviour, Second Edition. Second edi. London: CRC Press; 2014.
[82] Vayas I, Ermopoulos J, Ioannidis G. Design of Steel Structures to Eurocodes. 1st ed. Springer International Publishing; 2019.
[83] Wang W, Kodur V, Yang X, Li G. Experimental study on local buckling of axially compressed steel stub columns at elevated temperatures. Thin-Walled Struct 2014;82:33–45. https://doi.org/10.1016/j.tws.2014.03.015.
[84] Ansys Inc. ANSYS Mechanical Training Materials. Cust Train Mater 2010; December.
[85] Oñate E. Structural Analysis with the Finite Element Method. Linear Statics: Volume 1: Basis and Solids (Lecture Notes on Numerical Methods in Engineering and Sciences) (v. 1). 1st ed. Barcelona: CIMNE; 2009.
[86] ECCS-CECM-EKS. Ultimate Limit State Calculation Of Sway Frames With Rigid Joints. ECCS Publ No33 1984.
[87] Gere JM, Timoshenko SP. Mechanics of Materials. Third edit. London, United Kingdom: Springer International Publishing; 1991. https://doi.org/10.1007/978-1-4899-3124-5.